論文 / 著書情報
Article / Book Information

題目(和文)	
Title(English)	Study of Zn-Ge-O Thin Film as Alternative Low Electron Affinity N-Type Material for Wide Band Gap Chalcogenide Solar Cell
著者(和文)	Dwinanri Egyna
Author(English)	Dwinanri Egyna
出典(和文)	学位:博士(工学), 学位授与機関:東京工業大学, 報告番号:甲第12572号, 授与年月日:2023年9月22日, 学位の種別:課程博士, 審査員:山田 明,伊原 学,中川 茂樹,間中 孝彰,宮島 晋介,杉山 睦
Citation(English)	Degree:Doctor (Engineering), Conferring organization: Tokyo Institute of Technology, Report number:甲第12572号, Conferred date:2023/9/22, Degree Type:Course doctor, Examiner:,,,,,
学位種別(和文)	博士論文
Type(English)	Doctoral Thesis

DOCTORAL THESIS

Study of Zn-Ge-O Thin Film as Alternative Low Electron Affinity N-Type Material for Wide Band Gap Chalcogenide Solar Cell

Presented by:

Dwinanri Egyna

Supervisor:

Professor Akira Yamada

Department of Electrical and Electronic Engineering

Graduate School of Engineering

Tokyo Institute of Technology

Tokyo, Japan

June 2023

Abstract

The prospective and current performance of chalcogenide materials, such as $Cu(In,Ga)(S,Se)_2$ (CIGSSe) are well known in the thin film photovoltaics technology. However, CIGSSe material still has a lot of untapped potential, especially the wide band gap materials with $E_g \geq 1.4\ eV$. Wide band gap CIGSSe material may offer a material with the ideal band gap for single junction solar cells or a top cell for multijunction solar cells. Unfortunately, research into the wide band gap materials have yet to result in a high efficiency device, likely due to the incompatible n-type material for the heterojunction coupling.

In this work, a numerical study on the n-type layer of a CIGSSe-based photovoltaics were conducted to understand the contribution of the n-type materials on the device performance, the physical mechanisms, and the design rules for a suitable n-type material. It was found that a low electron affinity material is crucial to achieve a high V_{OC} by the improvement of interface passivation and contact selectivity.

In addition, a novel n-type material was developed through the alloying of ZnO and GeO_2, resulting in an alternative low electron affinity material for wide band gap CIGSSe-based photovoltaics. The film was

produced through the MOCVD method, utilizing tetramethoxygermanium as the Ge-precursor. By characterising the Zn-Ge-O films, it has been verified that higher $[Ge]/([Zn]+[Ge])$ lead to lower electron. The crystallography of the single films was also affected, resulting in a polycrystalline structure at lower $[Ge]/([Zn]+[Ge])$ and the aggregation of nanocrystals at higher $[Ge]/([Zn]+[Ge])$. Initial evaluations of the samples' electronic properties and its potential application in chalcogenide solar cells indicate promising outcomes, suggesting that the Zn-Ge-O thin film could serve as a viable alternative for the n-type layer in these solar cells in the future.

Keyword: CIGS solar cells; thin-film heterojunction; open-circuit voltage; n-type layer; buffer layer; transparent conductive oxide

Contents

Chapter 1 Introduction

1.1 Overview on Climate Change

Ever since the issue of global warming—and the encompassing climate change—was cemented in the awareness of the global society through the formation of Intergovernmental Panel on Climate Change (IPCC) in 1988 [1], the topic has rapidly transformed from a "possible bleak future" into a "current emergency crisis" that everyone has to live with. Across the globe, not only people are experiencing the record heatwaves in decades, but also dealing with the larger implication of such disruption in a large and sensitive system such as our global weather system.

Some of those detrimental impacts can be directly witnessed by the ever increasing maximum and minimum annual temperature as shown in Figure 1-1, or the occurrence and intensity of extreme storms portrayed in Figure 1-2. These global mapping of weather events illustrated the tendency of those weather events based on historical data up to 2020, and the projection of future events up to the end of the century based on models that were ever perfected by those historical records. Based on these data driven observations, the Working Group 1 (WG1) of IPCC has reached certain conclusions regarding our climate's future.

In their 6th Assessment Report (AR6) published in 2021, WG1 was virtually certain that the intensity, duration, and frequency of extreme high temperature will increase over most inhabited land areas [2]. They also claimed with high confidence that although in most regions the change in magnitude of the high temperature will be in proportion to global warming (i.e., 1.5° C of annual highest temperature increase for 1.5° C of global mean temperature increase), in some other places like the middle latitudes and polar regions the augmentation would be non-linear to the global warming levels [3].

In the report, IPCC GW1 also identified from the best-track and homogenized tropical cyclone data, there have been a 6% per decade increase of the global tropical cyclone intensity for the last four decades. In addition, there is evidence that suggest the intensification rates (i.e., the manner in which tropical cyclones escalate from lower category storm to higher category storm) and the frequency of rapid intensification occurrences have also increased during the same period[4-6]. They concluded that it is likely that tropical cyclone instances, intensity, and frequency will increase in the future, especially in the Pacific northwest[7].

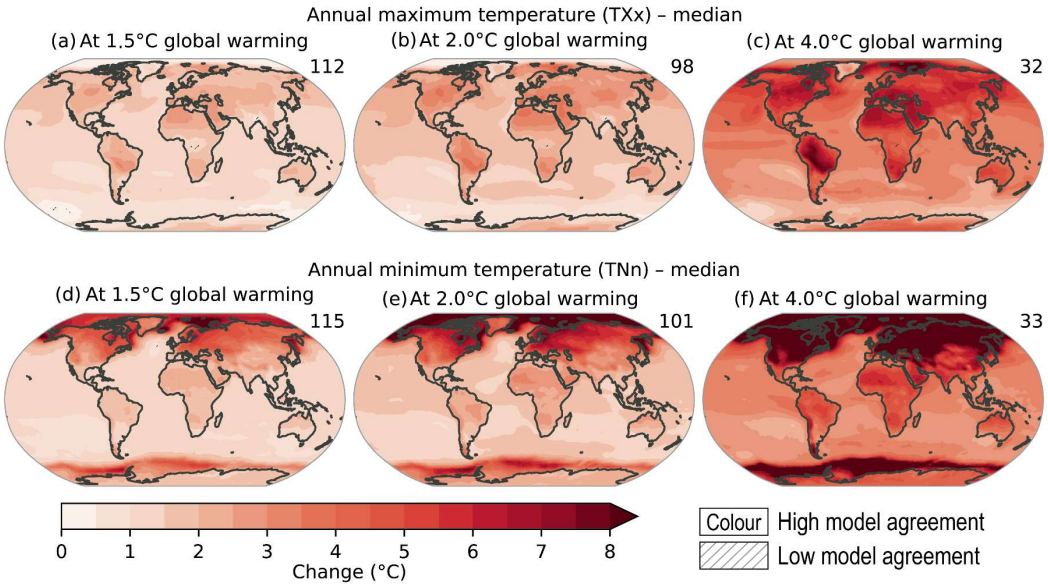

Figure 1-1 Projected changes in (a–c) annual maximum temperature (TXx) and (d–f) annual minimum temperature (TNn) at 1.5°C, 2°C, and 4°C of global warming compared to the 1850–1900 baseline. IPCC Sixth Assement Report, Working Group 1, 2021.

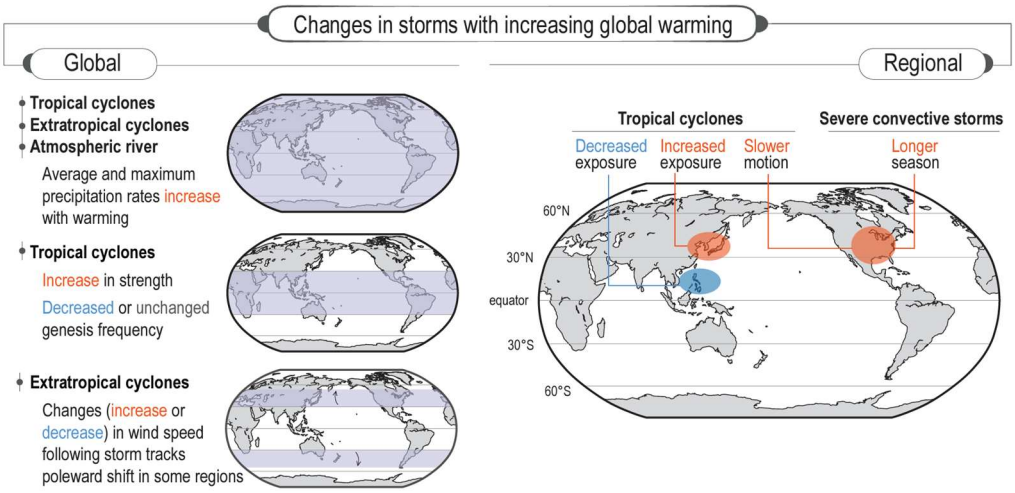

Figure 1-2 Summary schematic of past and projected changes in tropical cyclone, extratropical cyclone, atmospheric river, and severe convective storm behaviour. IPCC Sixth Assement Report, Working Group 1, 2021.

The overall increase of the mean temperature on itself will have a significant and direct impact to the quality of life of the human race. Certain regions on earth that are currently densely populated might be inhabitable in the future dude to the increase urban heat-island effect. In combination with the changes of the meteorological conditions, extreme air pollution episodes will also occur in the already highly polluted environments. In turn, these phenomena will reduce water availability, destabilise buildings, and disrupt local and global transportation system. Considering the human displacement that will inevitably follows, this vicious circle will end in a catastrophic, if not apocalyptic, result for the human race[8].

1.2 Overview on Energy

In recent time, we have come to understand that the Earth's climate system is an enormous and highly complex system, and post-industrial revolution human activities in multiple sectors have unfortunately contributed in the acceleration of the climate change. Therefore, participation and cooperation across different sectors is requisite in the mitigation efforts. In order to limit global warming between 1.5°C to 2°C, revolutionary steps have to be taken in urban planning, transportation, industry, agriculture, and energy—both in reformation and future development. In the purpose of this thesis however, we will focus on the mitigation efforts required in the energy sector.

1.2.1 Global Energy Consumption and Energy Crisis

Energy consumption in the 21st century has witnessed significant shifts and transformation, both from the supply side and the consumption side. As our awareness and understanding of the human-influenced climate change heightened, this first quarter of the century have seen a major increase in renewable sources, such as hydro, wind, and solar power, as shown in Figure 1-3 [9, 10]. The majority of these sources are converted into electricity sources and distributed towards industrial, commercial, and residential uses. The traditional energy sources such as coal, oil, and natural gas, though still dominating the market, are slowly decreasing or stagnating. From the consumption side, one of the major energy transitions is occurring in the transportation sector, where electrification of personal, commercial, and public transportation is gradually phasing out the use of petrol in that sector. It is a major effort towards a more sustainable future, considering transportation account for around 27% of total global energy consumption in 2019 (Figure 1-4).

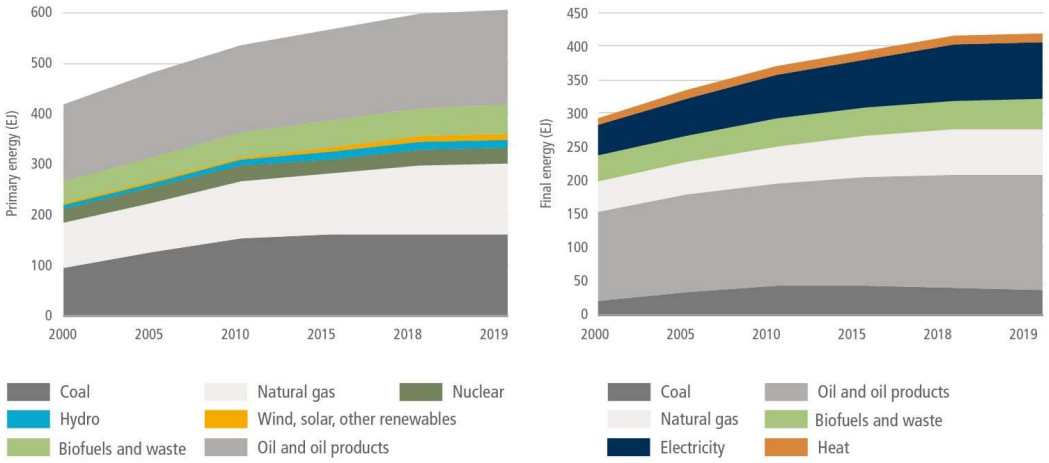

(a) (b)

Figure 1-3 (a) World total primary energy supply (TPES) (EJ) and (b) total final energy consumption (TFC) 2000–2019. IPCC Sixth Assement Report, Working Group 3, 2022.

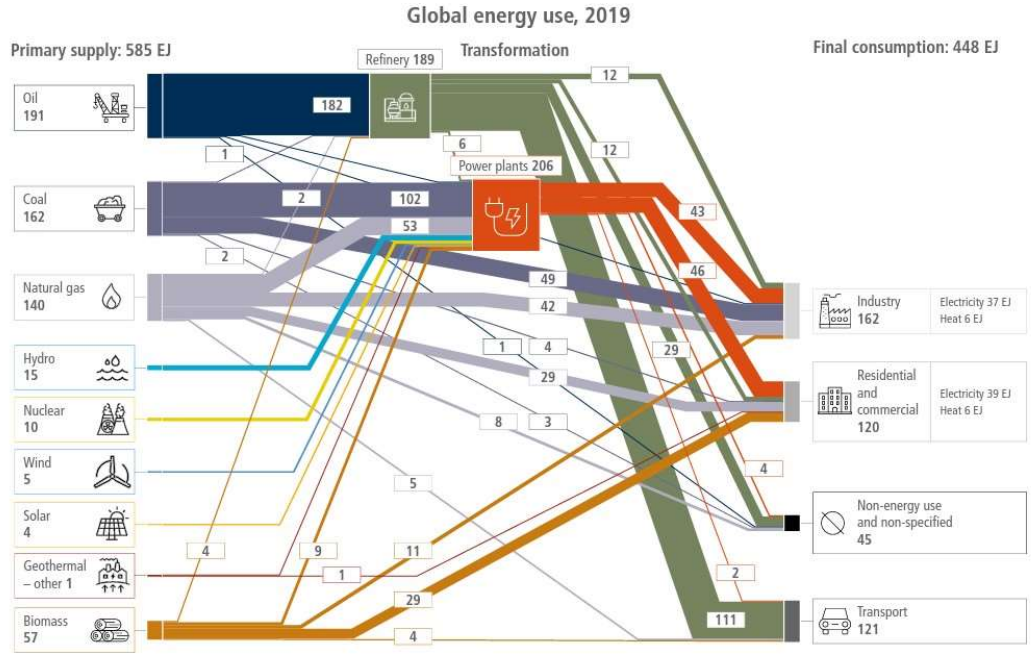

Figure 1-4 Global energy flows within the 2019 global energy system. IPCC Sixth Assement Report, Working Group 3, 2022.

The rapid growth of the electric vehicle (EV) market is illustrated in Figure 1-5. Based on the data from International Energy Agency (IEA) in the last decade, the market share of EV for the cars and vans has spiked up from virtually non-existent in 2010 to accounting for approximately 13% of the sales in 2022. A similar phenomenon was also seen in the two-wheelers market where the market share has grown more than 15 folds in 2022 compared to 2010. A more moderate growth in the large-vehicles market were also noted by IEA, specifically for buses and trucks. Since large-vehicles are responsible for mass transportation and commercial product distribution, this change would also bring a significant impact in mitigating the environmental impact of human activity. It can also be noted from the figure, that the majority of the sales is happening in China, followed by Europe for cars and vans, and India for two-wheelers.

In addition to shifting our energy supply to a more sustainable option, recognizing the significance of energy security is also crucial. IEA defines energy security as "uninterrupted availability of energy sources at an affordable price"[11]. In the short term, energy security pertains to the capacity of the energy system to swiftly respond to unforeseen shifts in the balance between energy supply and demand. In the last five years only, numerous global and local human-influenced calamity, both direct and indirect, have brought into picture the fragility of current energy system.

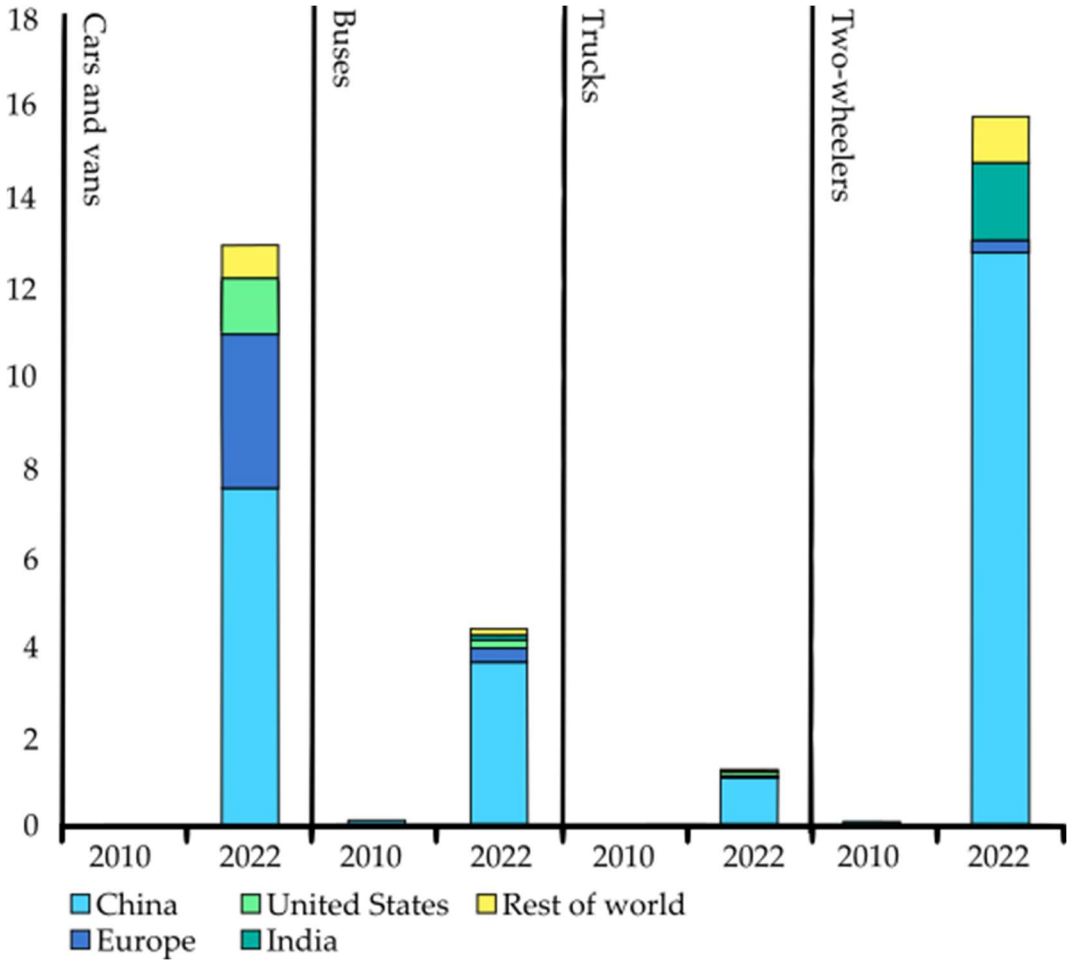

Figure 1-5 Comparison of the electric vehicles sales share in 2010 and 2012 by vehicle type and country. Figure is adapted from IEA.

In 2019, massive power loss occurred in the Java and Bali islands in Indonesia due to a single major transmission line issue, leaving more than 100 million people, major industries, and the capital city, Jakarta, without power for about 20 hours[12]. Extreme weather as an impact of climate change caused once-in-a-century grievous drought event in Brazil in 2021. For a country that relied on hydropower for more than 66% of its electricity

generation[13], the drought brought extremely serious energy crisis that resulted in steep cost for customers, and increase in fossil fuel consumption to meet the energy demands[14]. Another dire energy crisis in the recent years was brought by conflict cause by the Russian invasion of Ukraine in 2020. In response to the humanitarian crisis, the international community, including European Union (EU), imposed international sanctions against Russia as an effort to discourage the continuation of the war. In response, Russia, as the third largest petroleum producer and the second largest natural gas producer in the world [15], had decided to stop supplying its resources to certain countries. As a result, millions face sudden price hike in their energy cost while also facing food crisis in 2022[16], in the middle of winter for the norther hemisphere[17, 18].

These examples underlined vulnerability of the global energy systems on all segments: supply, distribution, and consumption. The future will likely bring more failures on aging existing energy systems, more severe climate change ramifications such as flood, drought, and extreme weathers, and more human-to-human conflicts due to the diminishing natural resources and displacement. Decentralised and diversified energy system is required to guarantee energy security for the future society.

1.2.2 Renewable Energy Sources

In recent years, renewable energy has emerged as a pivotal focus area in global efforts to mitigate climate change and ensure our survival as a species. With mounting concerns over dwindling fossil fuel reserves, environmental degradation, and the ever-worsening climate consequences, researchers, policymakers, and grassroot movements delve into the multi-faceted aspects of renewable energy to guarantee a smooth and swift transition for clean energy sources.

As the examples in Section 1.1 have demonstrated, climate change threatens both short-term and long-term energy security of our society. In terms of the short-term security, unlike fossil fuels, which are vulnerable to price volatility and geopolitical risks, renewable energy resources are inherently domestic and widely distributed, reducing dependence on imported fuels. It also allows for decentralization of energy supply, allowing local generation and reducing the vulnerability of the supply and distribution system. Renewable energy sources are also more versatile and scalable in their operation compared to large fossil fuel plants currently in operation, thus very responsive to fluctuation of supply and demand. In addition, for the long-term security, renewable energy resources are virtually inexhaustible, widely available, providing a stable and enduring energy supply. Diversification of energy mix and curtailment on fossil fuel dependence to reduce environmental impacts are inherent long-term

benefit of the transition to renewable energy. Moreover, renewable energy technologies have witnessed significant advancements, leading to improved efficiency, cost reductions, and scalability, making them increasingly competitive with conventional energy sources.

In 2021, renewable sources account for 28.7% of global electricity generation according to IEA. The rapid acceleration of wind and solar PV capacity shown in Figure 1-6 is responsible for the notable growth in renewable energy share for the past decade. The transition towards bioenergy source is also steadily growing. Despite the potential, the growth of geothermal and ocean source is still stalling[19].

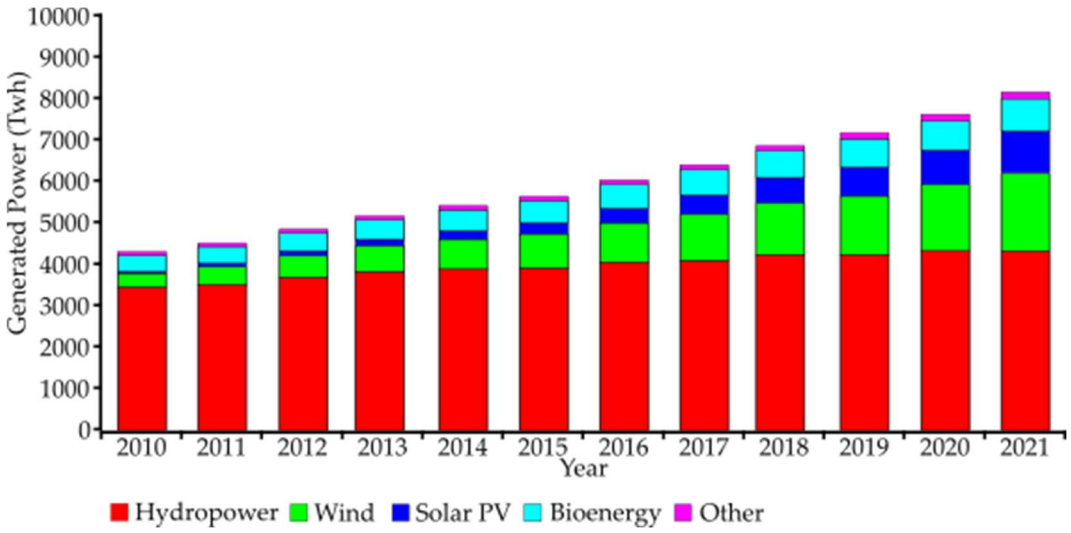

Figure 1-6 Growth of renewable energy power generation by technology 2010-2021. Figure is adapted from IEA.

Our primary emphasis will be on the application of photovoltaic cells for harnessing solar power among various renewable resources. The

utilization of solar energy through photovoltaic cells encompasses a broad spectrum of applications, spanning from terrestrial to extra-terrestrial settings, as well as encompassing both small and large-scale power generation. The generation of electricity through this method is environmentally friendly, as it is carbon-free and operates through a distinct mechanism in contrast to traditional mechanical-to-electrical processes.

1.3 Current Status of Photovoltaics

1.3.1 Theoretical Efficiency Limit of Photovoltaic cell

The efficiency of photovoltaic cells is constrained by the band gap, which is a fundamental property of the semiconductor material used. The band gap represents the energy difference between the valence band (where electrons are bound) and the conduction band (where electrons are free to move). If the band gap is too large, photons with lower energy cannot generate electron-hole pairs, leading to a loss of potential energy conversion. On the other hand, if the band gap is too small, higher energy photons are absorbed, but excess energy is wasted as heat rather than being converted into electricity. Therefore, finding the optimal band gap for a photovoltaic cell is crucial to maximize its efficiency by efficiently harvesting photons across a broad range of energies and minimizing energy losses due to thermalization.

The Shockley Quisser limit, also referred to as the SQ limit or detailed balance limit, represents the maximum theoretical efficiency achievable by photovoltaic cell of an ideal band gap. It was initially computed in 1961 by William Shockley and Hans J. Queisser for silicon-based photovoltaic cells operating at 1.1 eV with an efficiency of 30% [20]. Subsequent refinements to this value considered additional factors such as the globally measured solar spectra (A.M 1.5G), reflective back surfaces, and materials with band gaps that offer improved spectrum matching. For a photovoltaic cell utilizing a 1.34 eV band gap, the maximum theoretical efficiency could be enhanced to 33.7% [21].

Currently, based on the data compiled by the National Renewable Energy Laboratory (NREL) mapped in Figure 1-7, the latest highest efficiency record for a single-junction photovoltaic cell without concentrator is GaAs with 27.8% conversion efficiency[22]. GaAs has the band gap of 1.42 eV, which is close to the ideal band gap for a photovoltaic cell derived by Shockley and Queisser. Figure 1-8 showed the SQ limit of different photovoltaic cell materials, and their recent efficiency record[23]. As can be understood from the figure, the development in several photovoltaic cell materials have almost caught up with the aforementioned theoretical efficiency (blue circles). Several others however, still have a lot of room for development (green and red circles), either through material engineering or photovoltaic cell device structure engineering.

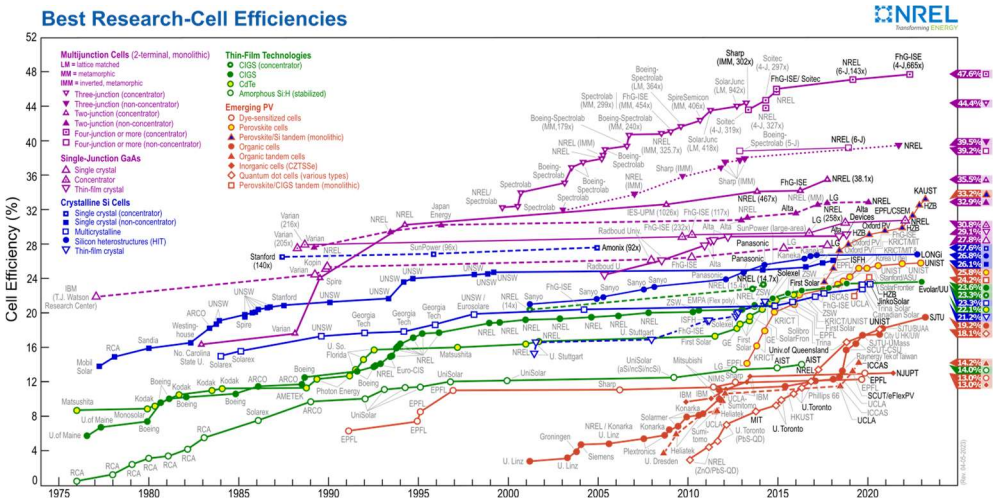

Figure 1-7 Recent efficiency records for various types of photovoltaic cells, NREL

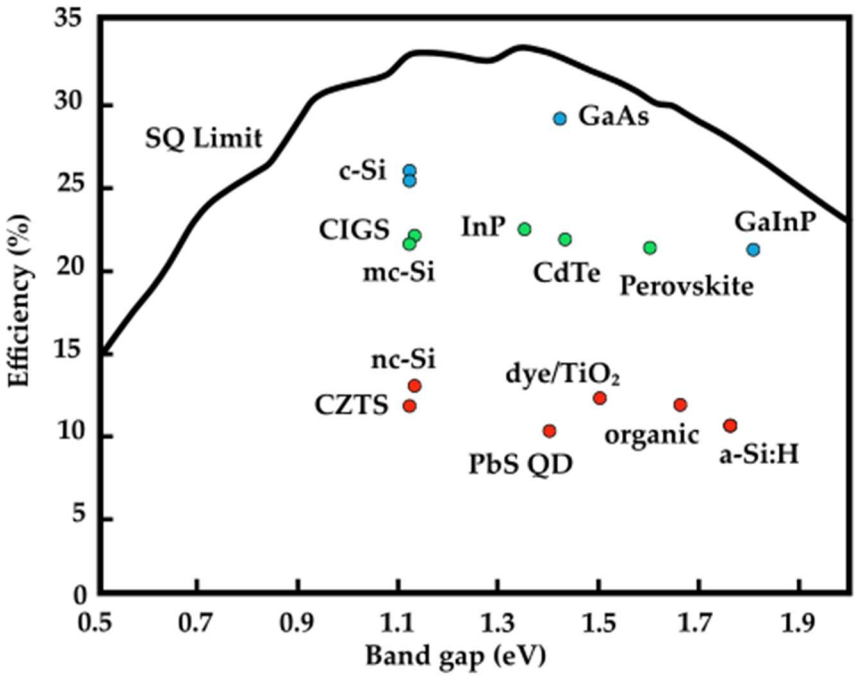

Figure 1-8 SQ Limit and current efficiencies of various photovoltaic cell materials.

Some of the prospective ternary or quaternary compound semiconductor materials in Figure 1-8 also possess a unique characteristic that

allows for tuning or modification of its band gap energy. adjusting the band gap, the material can be tailored to match the solar spectrum, maximizing the absorption of photons across a wide range of energies. This flexibility enables more efficient utilization of solar radiation, as it allows for the customization of the band gap to better match the incident light source. Therefore, materials such as $Cu(In,Ga)(S,Se)_2$ (CIGSSe), Cu_2ZnSnS_4 (CZTS), or perovskite arguably have the untapped potential of an ideal band gap photovoltaic cell.

Another pathway to maximising the energy conversion of photons through the photovoltaic device is through the multijunction photovoltaic cell design. A multijunction photovoltaic cell is a specialized type of photovoltaic cell composed of multiple single junction photovoltaic cells, each with a different band gap. The band gap of each junction is optimized to absorb specific ranges of wavelengths effectively as shown in Figure 1-9. Typically, in the structure of a multijunction photovoltaic cell, the junction with the widest band gap is placed on top to capture higher energy photons from shorter wavelengths. The subsequent junctions in the stack have progressively narrower band gaps, with the photovoltaic cell with the narrowest band gap positioned at the bottom. This arrangement reduces thermalization losses for higher energy photons and transmission losses for lower energy photons.

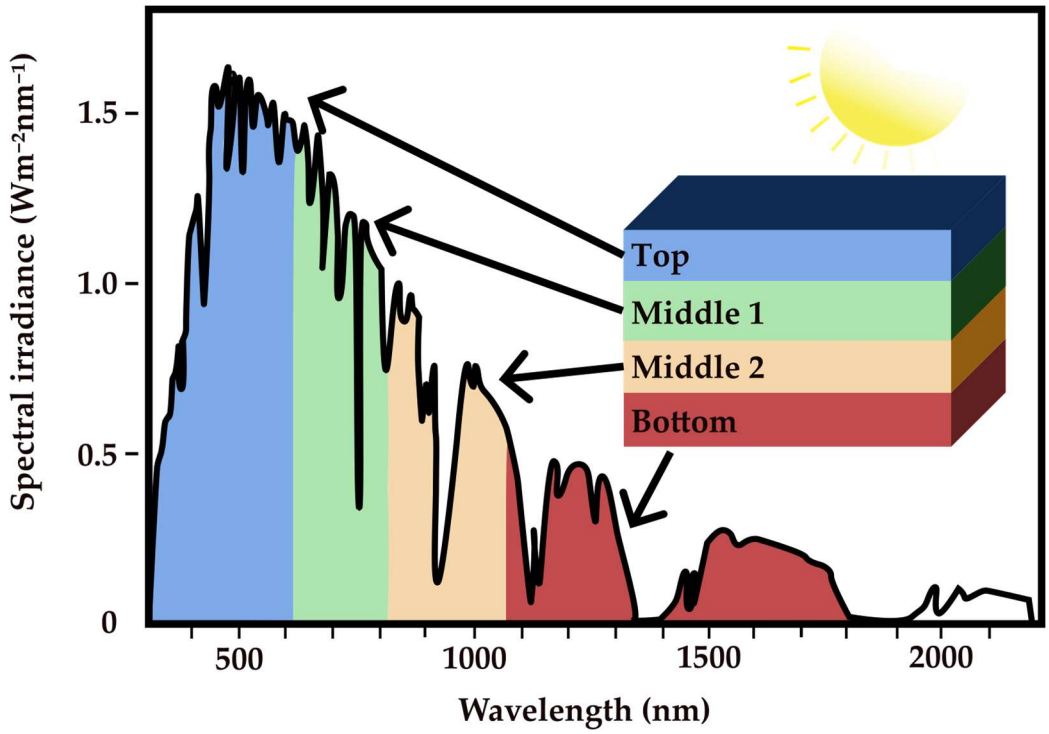

Figure 1-9 An illustration of multijunction photovoltaic cell design and the optimisation of photons absorption for specific wavelength range at each junction

The theoretical efficiency of a multijunction photovoltaic cell, assuming an infinite number of cells, can reach up to 68.2% under 1 sun conditions [24]. In practical applications, such as tandem photovoltaic cells with two cells of different band gaps or triple junction photovoltaic cells, the maximum theoretical efficiencies under 1 sun are around 50% and 56%, respectively [25]. Empirical evidence supports these theoretical estimates, demonstrating that multijunction photovoltaic cells outperform single junction cells, with some already surpassing the Shockley Quisser limit.

One of the common methods for integrating the junctions in multijunction photovoltaic cells is called mechanical stacking. In mechanical stacking, individual photovoltaic cells are stacked on top of each other with external electrical connections. Each junction operates independently, converting photons into electrical charges, which are then transported through individual contacts. This method is technically simpler and easier to fabricate, as it does not require current matching and allows for more flexible combinations of band gaps for each junction. However, a challenge of this method is the need for a transparent back contact to allow longer wavelength photons to pass through to the next junction. While Transparent Conductive Oxide (TCO) is commonly used as the front contact, further research is necessary to develop novel materials for the transparent back contact.

An alternative method for integrating the junctions in multijunction photovoltaic cells is monolithic integration. Unlike mechanical stacking, monolithic integration involves series-connecting the junctions through the bulk of the cell, similar to a single junction photovoltaic cell. This integration method requires only one front contact and one back contact. It is crucial to achieve current matching between the junctions to prevent carrier recombination between the layers. The quality of the interfaces between the top, middle, and bottom cells is also critical to minimize recombination caused by defects at the interfaces. However, the utilization of rare metals

and the need for high precision manufacturing contribute to the high production cost of this type of photovoltaic cell.

1.3.2 Photovoltaic Technologies

Broadly speaking, the materials used in photovoltaic technology can be divided into five categories: crystalline Si (c-Si), thin-film, organic, dye-sensitized, and perovskite.

Crystalline Si can be further divided into monocrystalline and multicrystalline technologies. Monocrystalline Si has the longest research and development history compared to any other materials, going back to 1955 for the first reasonably operating photovoltaic cell[26]. Answering the challenge of lowering the production cost, multicrystalline Si wafer was began to be used in 1980 by Solarex [27]. In 2018, panels made of c-Si photovoltaic technology still dominated the market with 75% share[28]. However, his was a decrease from 2014 where they made up 92% of the photovoltaic panels in the market [29]. The current efficiency record for c-Si photovoltaic technology is 26.8% by LONGi [30].

Due to the absorption coefficient material limitation, c-Si unfortunately has to be bulky and rigid, which limits the application potentials. Thin-film photovoltaic cells, on the other hand, took advantage of materials with high absorption coefficient, and thus enabling very thin layers to form a pn-junction device. Some of those materials are $Cu(In,Ga)(S,Se)_2$ (CIGSSe),

CdTe, and amorphous Si (a-Si). Although not as high as c-Si yet, the efficiency of thin-film technologies is slowly catching up with 23.35% for CIGSSe by Solar Frontier [31], 22.1% for CdTe by First Solar[32], and 10.2% for a-Si by AIST[33]. The thin-film technology is crucial in the development of multijunction solar cell.

Organic semiconductor solar cells, also referred to as organic photovoltaics (OPVs) or organic solar cells, are a specific kind of solar cell that employs organic materials as the active layer. These organic materials are typically composed of conjugated polymers or small molecules possessing semiconducting characteristics. Current efficiency record for OPV is 18.1% [34]. One of the advantages of organic semiconductor solar cells is their potential for low-cost production. However, the stability and the durability of OPVs are still underperformed compared to inorganic semiconductor.

Dye-sensitized solar cells (DSSCs), also referred to as Grätzel cells, are a specific kind of solar cell that employs a semiconductor material sensitized by a dye to convert sunlight into electrical energy. Typically, the dye consists of an organic molecule capable of absorbing light, commonly derived from ruthenium complexes or organic dyes. The dye was adsorbed by a wide-band gap semiconductor to form a transparent conducting substrate. One of the advantages of DSSCs is their ability to capture a wide range of sunlight wavelengths, including both visible and infrared light.

This makes them effective in low-light conditions and enables their use in indoor or cloudy environments. Currently, the efficiency record of DSSC is at 15.2%[35]. One of the main research focuses is stability, as the organic dyes tend to degrade over a period of time.

1.4 Overview of CIGSSe-based Photovoltaic

CIGSSe photovoltaic technology is a type of thin-film solar cell that has gained significant attention since its first development in the 1970s [36, 37]. In the last 50 years, the technology has progressed very far from a plain $CuInSe_2$/CdS pn-heterojunction [36] to a more complex Mo/Cu(In,Ga)$(S,Se)_2$/CdS/ZnO/ZnO:Al/Al structure[31]. From the commercial perspective, CIGSSe photovoltaics can be manufactured using low-cost and scalable processes, such as sputtering or evaporation, making them economically attractive. Additionally, CIGSSe solar cells can be deposited on flexible substrates, enabling the production of lightweight and flexible solar panels suitable for various applications. In this section, some key points on recent CIGSSe photovoltaics development will be briefly mentioned. These topics will be further expounded in Chapter 2.

The recapitulation of CIGSSe photovoltaics development can be seen in Figure 1-10. There are some of the significant checkpoints in the journey of CIGSSe research and development. These checkpoints have become the foundation of current high efficiency CIGSSe photovoltaics, but

also presented future challenges for other CIGSSe applications such tandem solar cell technology.

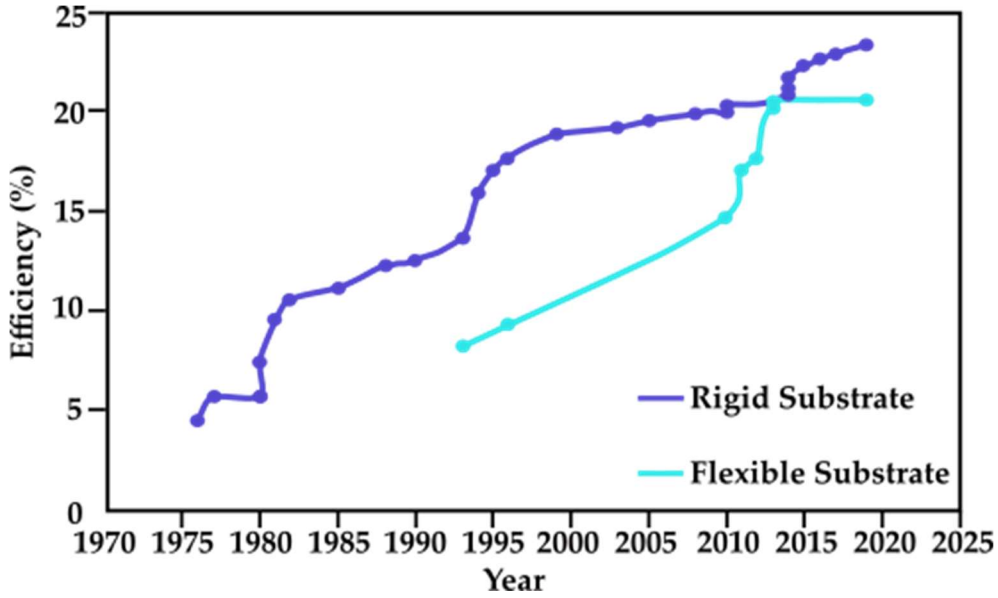

Figure 1-10 Progression of laboratory scale CIGS solar cell efficiency record.

For example, molybdenum (Mo) has been practically established as CIGSSe back contact material by the virtues of being chemically and mechanically stable throughout the CIGSSe photovoltaic device growth process [38]. The interfacial layer formed between Mo and CIGSSe, and the volume morphology have made this material irreplaceable [39, 40]. However, the low light transmission of Mo makes it unsuitable back contact material in the case of top cell application in tandem photovoltaics.

In regards of CIGSSe absorber, band gap grading and post deposition treatment have dramatically improved the open circuit voltage V_{OC} and the efficiency of CIGSSe photovoltaics. Through three-stage

co-evaporation method developed by NREL, the ratio of [Ga]/[Ga+In] across the absorber's bulk could be controlled, resulting in variety of energy band gap level at different depth of the absorber[41]. The introduction of various alkali elements from the surface of CIGSSe have also been noted to affect the electrical properties of the absorber and the pn-junction interface[42-45].

As a heterojunction solar cell, CIGSSe photovoltaics presented a unique challenge in regards of material coupling. Up until recently, CdS/ZnO double n-type layers had been the preferred combination to produce high performing CIGSSe photovoltaics[46]. However, considering the environmental impacts, the development of Cd-free CIGSSe has been at the forefront of research interest in the recent years[31, 47]. In addition, the pn-junction interface of heterojunction solar cells has also been found to have a significant impact on the solar cell performance. Therefore, interface engineering and alternative n-type materials for CIGSSe absorber are the current focal point of the field[48-50].

1.5 Overview of Transparent Conductive Oxide

Transparent conductive oxide (TCO) is an essential component that has revolutionised the modern electronics part. From our personal devices to multifunctional facades, biochemical/environmental sensors to photovoltaic panels, and wearable electronics to transparent heaters, TCOs

play a big role in implementing and improving these electronic devices[51]. TCOs are a class of semiconductor materials that inhibit wide optical band gap around the ultraviolet range ($E_g > 3.2\ eV$). Therefore, these materials have high transparency on the visible light wavelength with transmittance $> 80\%$. TCO materials also have conductivity close to that of metals, which can be induced by doping[52]. In addition, they also reflect near infrared and infrared wavelengths[53].

TCO was first studied by Bädeker in 1907 in his work on CdO thin films prepared by sputtering and thermal oxidation, in which the transparent films showed to possess electrical conducting property[54]. This ground-breaking research paved the path to further discoveries of other TCO materials, dominated by p-block heavy metals such as SnO_2, In_2O, ZnO, Ga_2O_3, Tl_2O_3, etc.[55]. Innovations through novel ternary and quaternary transition metals oxide compounds such as Zn_2SnO_4, $GaInO_3$, $Zn_2In_2O_5$, etc. were also shown to have potentials in the variety of TCO application[56]. Considering the massive impact TCO has to modern electronic devices, efforts were made to boost the durability, lower the manufacturing cost, and improve the environmental impact of TCOs[57].

ZnO is one of the attractive TCOs for numerous applications, especially because of the low-cost material source and non-toxicity. ZnO is direct band gap semiconductor with relatively wide band gap and huge exciton binding energy[58]. The peculiarity of ZnO has been attributed to the

high ionization energy of oxygen, the highest among the elements in group VI. This high ionization energy was claimed to result in a strong interaction between the Zn (3d) and O (2p) orbitals in ZnO [59]. In regards to doping, efficient doping with group III elements dopant could decrease the film resistivity dramatically [60].

1.6 Research Objectives

The current efficiency of single junction CIGSSe solar cells with a band gap of approximately 1.0-1.2 eV is approaching 25%, which represents the current record. In order to achieve even higher efficiency with a single junction solar cell, it is necessary to utilize materials with wider band gaps, around 1.4 eV, to achieve better spectral matching. Additionally, the development of all CIGSSe tandem solar cells for increased yield requires a chalcopyrite top cell with an efficiency surpassing 20%. $CIGS_2$ material shows promise in fulfilling both requirements. However, while significant progress has been made in the research of $CIGSe_2$ solar cells, there has been limited investigation into pure sulfide $CIGS_2$ solar cells in comparison. Therefore, we aim to elucidate the fundamental mechanisms within the n-type layers of thin film heterojunction solar cell such as CIGSSe in regards to the carrier generation and transport. Such research is crucial to achieve high-efficiency solar cells with wider band gaps.

In addition, a novel n-type layer material will be explored in this study, focusing on ZnGeO thin film transparent conductive oxide as an alternative n-type layers for CIGSSe-based photovoltaics. The research will involve the synthesis of ZnGeO thin films using metal-organic chemical vapour deposition (MOCVD), followed by characterisation and thorough investigation of their optoelectronic properties and crystallography of the novel material. Up to date, there has been no fundamental research done on ZnGeO transparent conductive oxide for thin-film heterojunction photovoltaics.

1.7 Thesis Outline

The thesis will be organized into four main chapters that progressively delve into different aspects of photovoltaic technology and materials.

Chapter 1 serves as the introduction to the thesis and covers various important topics. It begins by providing an overview of climate change, emphasizing the need for sustainable solutions to address the environmental challenges we face. Following that, a discussion on energy takes place, including an exploration of global energy consumption and the energy crisis. The significance of renewable energy sources is highlighted, showcasing their potential to mitigate climate change and promote a sustainable future. The chapter then delves into the current status of photovoltaics,

offering insights into the theoretical efficiency limit of photovoltaic cells and examining different photovoltaic technologies. Additionally, an overview of CIGSSe-based photovoltaic technology is provided, focusing on its structure and key components. The role of transparent conductive oxide (TCO) in enhancing photovoltaic cell performance is also discussed. Finally, the research objectives of the thesis are outlined, clarifying the goals, addressing knowledge gaps, and describing the methodology that will be employed throughout the study.

Chapter 2 focuses specifically on CIGSSe-based photovoltaics. The chapter begins with an introduction to the topic, providing background information and setting the context for further discussions. It then proceeds to discuss the device structure of CIGSSe-based photovoltaics, highlighting key components such as the substrate, back contact, Cu(In,Ga)(S,Se)2 p-type absorber layer, and buffer and window layers. The chapter explores the technological advancements in CIGSSe photovoltaics, starting with the development of CIGSSe tandem solar cells, which have the potential to enhance efficiency through the combination of multiple absorber layers. Additionally, alternative n-type buffer layer materials will be investigated as potential alternatives to improve device performance. The chapter also introduces the concept of buffer-free CIGSSe solar cells, which offer a novel approach in the field. Overall, this chapter aims to provide a comprehensive

understanding of CIGSSe-based photovoltaics and the advancements that have been made in this area.

Chapter 3 focuses on the utilization of low electron affinity materials in thin-film heterojunction photovoltaics. The chapter begins with an introduction, providing an overview of the topic and its significance in the field of photovoltaics. It then introduces the SCAPS 1D simulation software, which will be utilized for the analysis and modeling in this chapter. The chapter explores the window/absorber structure with ideal interface conditions, discussing the simulation modeling, parameters, and the analysis of solar cell characteristics. Furthermore, the energy level shifts in the band diagram will be analyzed, shedding light on the mechanisms governing charge transport and recombination in thin-film heterojunction photovoltaics. The chapter then proceeds to examine the window/absorber structure with interface defects, including simulation modeling, parameters, and the analysis of solar cell characteristics in such conditions. Additionally, the roles of the N-type layer in realistic design conditions will be discussed. This includes exploring the N-type layer's function as interface passivation, where it plays a crucial role in reducing interface recombination and improving device performance. Furthermore, the N-type layer will be explored in terms of its function as a selective electron contact, enabling efficient charge extraction from the absorber layer. Overall, Chapter 3 aims to provide in-depth analysis and insights into the utilization of low electron

affinity materials and their impact on thin-film heterojunction photovoltaics.

Chapter 4 focuses specifically on the investigation of Zn-Ge-O thin film as a low electron affinity material in photovoltaic applications. The chapter begins with an introduction, providing an overview of the topic and its relevance in the context of photovoltaic devices. It then delves into the concept of transparent conductive oxide (TCO), exploring its properties and highlighting its importance in enhancing the performance of photovoltaic devices. The chapter further examines the dependence of the N-type layer on the Ga- and S-content in the CIG(SSe)2 absorber layer, investigating the relationship between these components and the N-type layer's performance. Additionally, the chapter explores the band gap engineering and alloy coupling of ZnO, discussing strategies to modify its properties for optimal device performance. The experimental set-up is described, encompassing the epitaxial film growth and film characterization processes. The analysis of a single layer Zn-Ge-O thin film follows, including an assessment of its optical, mechanical, and electrical properties. The chapter concludes by examining the utilization of the Zn-Ge-O film in a photovoltaic device, highlighting its potential as a low electron affinity material for enhancing device performance and efficiency. This provides valuable insights into its practical applications in the field of photovoltaics.

References

[1] "About the IPCC", https://www.ipcc.ch/about/. [Accessed 04/27/2023]

[2] C. Li, F. Zwiers, X. Zhang, G. Li, Y. Sun, and M. Wehner, "Changes in Annual Extremes of Daily Temperature and Precipitation in CMIP6 Models," *Journal of Climate,* vol. 34, no. 9, pp. 3441-3460, 5 2021.

[3] S. I. Seneviratne, M. G. Donat, A. J. Pitman, R. Knutti, and R. L. Wilby, "Allowable CO2 emissions based on regional and impact-related climate targets," *Nature,* vol. 529, no. 7587, pp. 477-483, 1 2016.

[4] J. P. Kossin, K. R. Knapp, T. L. Olander, and C. S. Velden, "Global increase in major tropical cyclone exceedance probability over the past four decades," *Proceedings of the National Academy of Sciences,* vol. 117, no. 22, pp. 11975-11980, 6 2020.

[5] K. Balaguru, G. R. Foltz, and L. R. Leung, "Increasing Magnitude of Hurricane Rapid Intensification in the Central and Eastern Tropical Atlantic," *Geophysical Research Letters,* vol. 45, no. 9, pp. 4238-4247, 5 2018.

[6] K. Bhatia, G. Vecchi, H. Murakami, S. Underwood, and J. Kossin, "Projected Response of Tropical Cyclone Intensity and Intensification in a Global Climate Model," *Journal of Climate,* vol. 31, no. 20, pp. 8281-8303, 10 2018.

[7] T. Knutson *et al.*, "Tropical Cyclones and Climate Change Assessment: Part II: Projected Response to Anthropogenic Warming," *Bulletin of the American Meteorological Society,* vol. 101, no. 3, pp. E303-E322, 3 2020.

[8] S. I. Seneviratne, X. Zhang, M. Adnan, W. Badi, C. Dereczynski, A. Di Luca, S. Ghosh, I. Iskandar, J. Kossin, S. Lewis, F. Otto, I. Pinto, M. Satoh, S.M. Vicente-Serrano, M. Wehner, and B. Zhou, "2021: Weather and Climate Extreme Events in a Changing Climate," in *Climate Change 2021: The Physical Science Basis.*Cambridge: Cambridge University Press, 2021.

[9] L. Clarke *et al.*, "Energy Systems," in *IPCC, 2022: Climate Change 2022: Mitigation of Climate Change Cambridge:* Cambridge University Press, 2022.

[10] J. C. Minx *et al.*, "A comprehensive and synthetic dataset for global, regional, and national greenhouse gas emissions by sector 1970-2018 with an extension to 2019," *Earth System Science Data,* vol. 13, no. 11, pp. 5213-5252, 11 2021.

[11] I. E. Agency. "Energy Security", https://www.iea.org/areas-of-work/energy-security. [Accessed 05/05/2023

[12] A. B. Da Costa and F. Nangoy. "CORRECTED-UPDATE 3-Millions lose power as Indonesia capital, parts of Java hit by blackout |

Reuters", https://jp.reuters.com/article/indonesia-power-idAFL4N25003W. [Accessed on 05/10 2022]

[13] S. Johnson, N. Manzagol, and K. Antonio. "U.S. Energy Information Administration - EIA - Independent Statistics and Analysis", https://www.eia.gov/todayinenergy/detail.php?id=49436. [Accessed 05/05/2023

[14] L. A. Cuartas *et al.*, "Recent Hydrological Droughts in Brazil and Their Impact on Hydropower Generation," *Water,* vol. 14, no. 4, p. 601, 2022.

[15] I. E. Agency. "Russian War on Ukraine", https://www.iea.org/topics/russias-war-on-ukraine. [Accessed 04/27/2023]

[16] M. Behnassi and M. El Haiba, "Implications of the Russia–Ukraine war for global food security," *Nature Human Behaviour,* vol. 6, pp. 754-755, 2022.

[17] G. Grandea, "Food Crisis, Energy Crisis and Recession: A Global Opportunity and Challenge towards Endemic," *International Journal of Science and Society,* Vol. 4, no. 4, pp. 223-233, 2022.

[18] A. Vaughan, *The first global energy crisis*. Reed Business Information, 2022.

[19] I. E. Agency. "Renewable Electricity", https://www.iea.org/reports/renewable-electricity. [Accessed on 05/11/2023]

[20] W. Shockley and H. J. Queisser, "Detailed Balance Limit of Efficiency of p‐n Junction Solar Cells," *Journal of Applied Physics,* vol. 32, no. 3, pp. 510-519, 3 1961.

[21] S. Rühle, "Tabulated values of the Shockley–Queisser limit for single junction solar cells," *Solar Energy,* vol. 130, pp. 139-147, 6 2016.

[22] NREL. "Best Research-Cell Efficiency Chart | Photovoltaic Research", https://www.nrel.gov/pv/cell-efficiency.html. [Accessed on 05/12/2023

[23] A. Polman, M. Knight, E. C. Garnett, B. Ehrler, and W. C. Sinke, "Photovoltaic materials: Present efficiencies and future challenges," *Science,* vol. 352, no. 6283, 4 2016.

[24] A. De Vos, "Detailed balance limit of the efficiency of tandem solar cells," *Journal of Physics D: Applied Physics,* vol. 13, no. 5, p. 839, 1980.

[25] C. H. Henry, "Limiting efficiencies of ideal single and multiple energy gap terrestrial solar cells," *Journal of applied physics,* vol. 51, no. 8, pp. 4494-4500, 1980.

[26] M. A. Green, "Silicon photovoltaic modules: a brief history of the first 50 years," *Progress in Photovoltaics: Research and Applications,* vol. 13, no. 5, pp. 447-455, 8 2005.

[27] J. Lindmayer and Z. Putney, "Semicrystalline versus single crystal silicon," in *Phtovoltaic Specialists Conference*, USA, 1980, pp. 208-213: IEEE.

[28] A. Mandaokar, "The photovoltaic materials market is projected to grow at a 8.5% CAGR between 2020-2030," 2023.

[29] M. S. Chowdhury *et al.*, "An overview of solar photovoltaic panels' end-of-life material recycling," *Energy Strategy Reviews,* vol. 27, p. 100431, 1 2020.

[30] LONGi. "LONGi once again sets new world record for HJT solar cell efficiency", https://www.longi.com/en/news/new-hjt-world-record/. [Accessed on 05/15/2023]

[31] M. Nakamura, K. Yamaguchi, Y. Kimoto, Y. Yasaki, T. Kato, and H. Sugimoto, "Cd-Free Cu(In,Ga)(Se,S)2 thin-film solar cell with record efficiency of 23.35%," *IEEE Journal of Photovoltaics,* vol. 9, no. 6, pp. 1863-1867, 11 2019.

[32] F. Solar. "First Solar, Inc. - First Solar Achieves Yet Another Cell Conversion Efficiency World Record", https://investor.firstsolar.com/news/press-release-details/2016/First-

Solar-Achieves-Yet-Another-Cell-Conversion-Efficiency-World-Record/default.aspx. [Accessed on 05/16/2023]

[33] T. Matsui *et al.*, "High-efficiency amorphous silicon solar cells: Impact of deposition rate on metastability," *Applied Physics Letters*, vol. 106, no. 5, p. 053901, 2 2015.

[34] M. Zhang *et al.*, "Single-layered organic photovoltaics with double cascading charge transport pathways: 18% efficiencies," *Nature Communications 2021 12:1*, vol. 12, no. 1, pp. 1-10, 1 2021.

[35] Y. Ren *et al.*, "Hydroxamic acid pre-adsorption raises the efficiency of cosensitized solar cells," *Nature 2022 613:7942*, vol. 613, no. 7942, pp. 60-65, 10 2022.

[36] L. L. Kazmerski, F. R. White, and G. K. Morgan, "Thin ‐ film CuInSe2/CdS heterojunction solar cells," *Applied Physics Letters*, vol. 29, no. 4, pp. 268-270, 8 1976.

[37] L. L. Kazmerski, F. R. White, M. S. Ayyagari, Y. J. Juang, and R. P. Patterson, "Growth and characterization of thin ‐ film compound semiconductor photovoltaic heterojunctions," *Journal of Vacuum Science and Technology*, vol. 14, no. 1, pp. 65-68, 1 1977.

[38] S. Raud and M. A. Nicolet, "Study of the CuInSe2/Mo thin film contact stability," *Thin Solid Films*, vol. 201, no. 2, pp. 361-371, 6 1991.

[39] T. Wada, N. Kohara, S. Nishiwaki, and T. Negami, "Characterization of the Cu(In,Ga)Se2/Mo interface in CIGS solar cells," *Thin Solid Films*, vol. 387, no. 1-2, pp. 118-122, 5 2001.

[40] J. H. Yun *et al.*, "Fabrication of CIGS solar cells with a Na-doped Molayer on a Na-free substrate," *Thin Solid Films*, vol. 515, no. 15, pp. 5876-5879, 5 2007.

[41] A. M. Gabor, J. R. Tuttle, D. S. Albin, M. A. Contreras, R. Noufi, and A. M. Hermann, "High ‐ efficiency CuIn x Ga1− x Se2 solar cells made from (In x, Ga1− x) 2Se3 precursor films," *Applied Physics Letters*, vol. 65, no. 2, pp. 198-200, 1994.

[42] T. Dullweber *et al.*, "Back surface band gap gradings in Cu(In,Ga)Se2 solar cells," *Thin Solid Films*, vol. 387, no. 1-2, pp. 11-13, 5 2001.

[43] A. Belghachi and N. Limam, "Effect of the absorber layer band-gap on CIGS solar cell," *Chinese Journal of Physics*, vol. 55, no. 4, pp. 1127-1134, 8 2017.

[44] F. Ghavami and A. Salehi, "High-efficiency CIGS solar cell by optimization of doping concentration, thickness and energy band gap," https://doi.org/10.1142/S0217984920500530, vol. 34, no. 4, 12 2019.

[45] F. Tchomb Mabvuer, F. Tchangnwa Nya, and G. M. Dzifack Kenfack, "Improving the absorption spectrum and performance of CIGS solar

cells by optimizing the stepped band gap profile of the multilayer absorber," *Solar Energy,* vol. 240, pp. 193-200, 7 2022.

[46] P. Jackson, R. Wuerz, D. Hariskos, E. Lotter, W. Witte, and M. Powalla, "Effects of heavy alkali elements in Cu(In,Ga)Se2 solar cells with efficiencies up to 22.6%," *physica status solidi (RRL) – Rapid Research Letters,* vol. 10, no. 8, pp. 583-586, 8 2016.

[47] S. Shi *et al.*, "Optimizing the thickness of sputtering-Zn(O, S) buffer layer for all-dry Cd-free CIGS solar cells," *Materials Research Express,* vol. 6, no. 8, p. 086431, 5 2019.

[48] S. Sinha, D. K. Nandi, P. S. Pawar, S. H. Kim, and J. Heo, "A review on atomic layer deposited buffer layers for Cu(In,Ga)Se2 (CIGS) thin film solar cells: Past, present, and future," *Solar Energy,* vol. 209, pp. 515-537, 10 2020.

[49] R. Prasad, A. K. Das, and U. P. Singh, "Impact of buffer layers on the performance of graded CIGS solar cells: a numerical approach," *Applied Physics A: Materials Science and Processing,* vol. 127, no. 11, pp. 1-12, 11 2021.

[50] N. Beyrami, M. Saadat, and Z. Sohbatzadeh, "A modeling study on utilizing In2S3 as a buffer layer in CIGS-based solar cells," *Journal of Computational Electronics,* vol. 21, no. 6, pp. 1329-1337, 12 2022.

[51] B. G. Lewis and D. C. Paine, "Applications and Processing of Transparent Conducting Oxides," *MRS Bulletin,* vol. 25, no. 8, pp. 22-27, 8 2000.

[52] C. G. Granqvist and A. Hultåker, "Transparent and conducting ITO films: new developments and applications," *Thin Solid Films,* vol. 411, no. 1, pp. 1-5, 5 2002.

[53] V. Fang, J. V. Kennedy, J. Futter, and J. Manning, *A Review of Near Infrared Reflectance Properties of Metal Oxide Nanostructures*. GNS Science, 2013.

[54] K. Bädeker, "Über die elektrische Leitfähigkeit und die thermoelektrische Kraft einiger Schwermetallverbindungen," *Annalen der Physik,* vol. 327, no. 4, pp. 749-766, 1 1907.

[55] T. Coutts, J. Perkins, D. Ginley, and T. Mason, "Transparent Conducting Oxides: Status and Opportunities in Basic Research," *Transparent Conducting Oxides: Status and Opportunities in Basic Research,* vol. 99, 1 1999.

[56] T. Minami, "New n -Type Transparent Conducting Oxides," *MRS Bulletin,* vol. 25, no. 8, pp. 38-44, 8 2000.

[57] T. Minami, "Substitution of transparent conducting oxide thin films for indium tin oxide transparent electrode applications," *Thin Solid Films,* vol. 516, no. 7, pp. 1314-1321, 2 2008.

[58] T. C. Collins and R. J. Hauenstein, "Fundamental Properties of ZnO," in *Zinc Oxide Materials for Electronic and Optoelectronic Device Applications*Chichester, UK: John Wiley & Sons, Ltd, 2011, pp. 1-28.

[59] K. Ellmer and A. Klein, "ZnO and its applications," *Transparent conductive zinc oxide: basics and applications in thin film solar cells,* pp. 1-33, 2008.

[60] Y. Liu, Y. Li, and H. Zeng, "ZnO-Based Transparent Conductive Thin Films: Doping, Performance, and Processing," *Journal of Nanomaterials,* vol. 2013, p. 196521, 2013.

Chapter 2 CIGSSe-based Photovoltaics

2.1 Introduction

Chalcogenide solar cells are a type of photovoltaic device that utilizes chalcogenide materials, such as sulfides (S), selenides (Se), and tellurides (Te), as the p-type absorber layer. These materials have unique properties that make them suitable for solar cell applications. Chalcogenide solar cells can be categorized into different types based on the specific chalcogenide material used, such as $Cu(In,Ga)(S,Se)_2$ (CIGSSe) solar cells, CdTe solar cells, and $Cu_2Zn_2SnS_4$ (CZTS) solar cells. In particular, these materials are suitable as thin-film photovoltaics owing to their high absorption coefficient [1-4]. It results in lower material usage to fabricate a lightweight panel with comparable efficiency, thus reducing the cost from both manufacturing and installation perspectives [2, 5]. In addition, chalcogenide-based photovoltaics also benefitted from another aspect of thin-film technology: flexible substrate. Chalcogenide absorber has been deposited on various type of flexible substrates such as polyimide (PI), polyether sulfone (PES), stainless steel, or molybdenum foil [6-9].

Among the different types of chalcogenide absorbers, only two materials have been commercialised: CIGSSe and CdTe [10, 11]. The current record efficiency these two materials are 23.35% [12] and 22.1% [13] for

CIGSSe and CdTe respectively. In this study, I will focus on CIGSSe-based photovoltaics in particular as the intended p-type absorber material. In this chapter, a general review of CIGSSe-based photovoltaics technology will be discussed. At the end, several emerging research on CIGSSe-based solar cell would be summarised.

2.2 CIGSSe-based Photovoltaics Device Structure

Figure 2-1 illustrates a common structure for heterojunction solar cells using a CIGSSe absorber. The multiple layers are grown upwards, and thus require a substrate. Depending on the intended application, the substrate may either be a rigid glass substrate or a flexible substrate. On the next layer a back contact material coats the substrate and serves as the electrical contact for the absorber layer. In addition to good conductivity, this layer shall also adhere well to the specific absorber deposited onto it. Next, the main part of the photovoltaic devices in the p-type absorber layer, in this case a CIGSSe-based material. This layer serves as the energy converter which will capture photons and transform them into electron-hole pairs that will be utilised in the electrical energy generation. The top 2 layers are the n-type materials which collects and transport the charge carriers onto to the front contact. It is crucial for these layers to be both transparent to allow the maximum amount of photon to reach the absorber, and highly conductive to effectively transfer the generated charged carrier.

In this structure, the CIGSSe absorber layer is typically directly deposited onto a soda lime glass (SLG) substrate coated with a rear contact material. Various metals, including Au, Ti, Mo, Ni, Ag, Al, and Cu, have been explored as potential rear contact materials. Among them, Au, Ti, Mo, and Ni have shown consistent and low-resistivity contacts with CIGS[14]. However, it should be noted that Au and Ti tend to diffuse into the CIGSSe film at high temperatures, such as during the deposition process[15, 16]. Additionally, combining Mo with SLG offers the advantage of facilitating the diffusion of sodium (Na) through Mo via thermal activation during absorber growth, which can enhance cell efficiency [17].

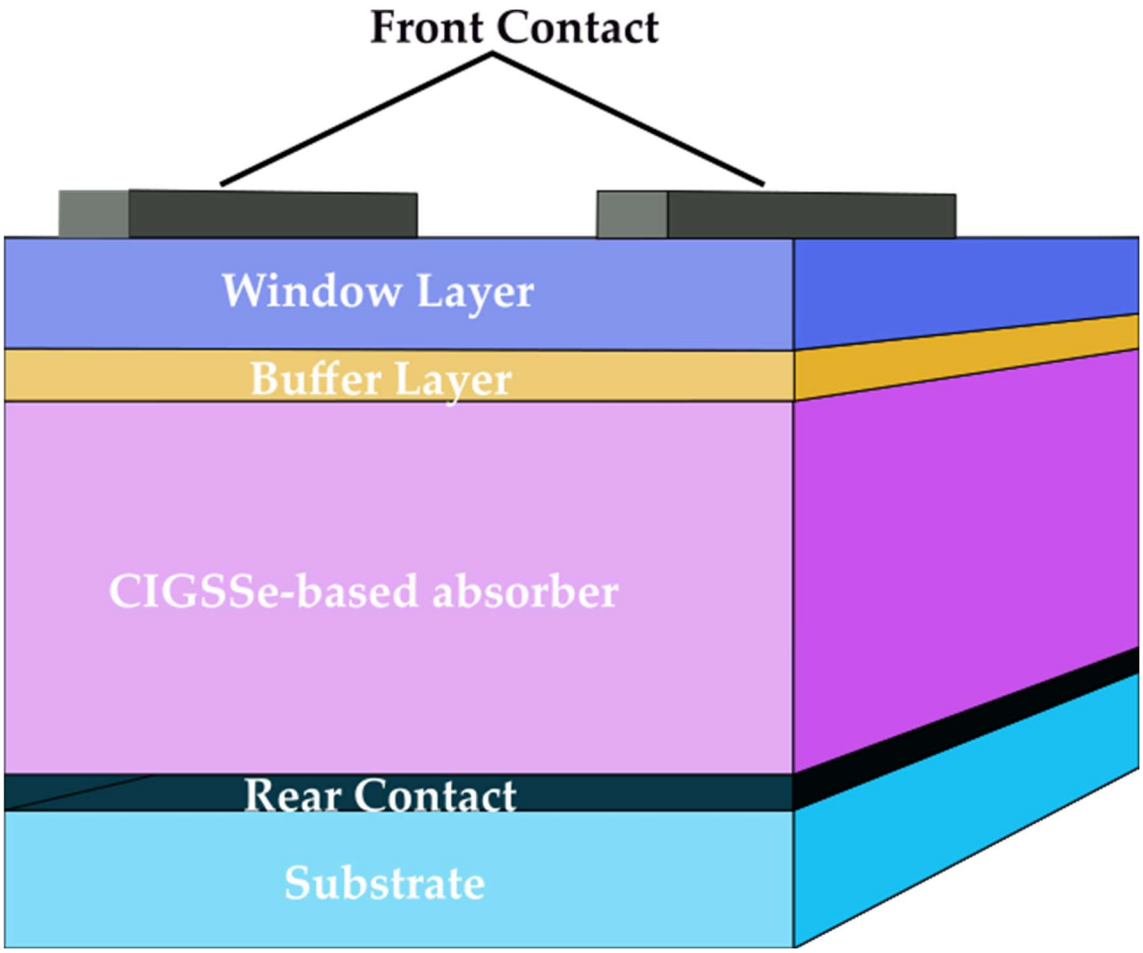

Figure 2-1 A typical device structure of thin-film heterojunction CIGSSe Solar Cell

2.2.1 Substrate

The choice of substrate in CIGSSe photovoltaics has a crucial role in the device's manufacturing line by limiting the high process temperature required for the crystallisation of the absorber. While the common rigid substrate for CIGSSe, soda lime glass (SLG), have long shown the ability to withstand CIGSSe deposition temperature [18], flexible substrate such polyimide (PI) would degrade when exposed to temperature higher than 500°C [19, 20]. Other flexible substrates such as stainless steel have also been examined in other studies [21].

In addition to being mechanically suitable, SLG substrate also possess an additional benefit of sodium (Na). The effect of Na diffusion from the glass substrate into the absorber layer during the high temperature process on CIGSSe deposition has been attributed to the improvement of cell improvement, especially V_{OC} [22, 23].

2.2.2 Back Contact

Coating the substrate, the back contact primarily serves as a carrier collector to transport the separated holes from electron-hole pairs to external circuit. In addition, back contact may also function as an optical reflector optimising the photon absorption in the absorber bulk.

Up to date, molybdenum (Mo) is the preferred material for CIGSSe photovoltaics' back contact. The advantages of Mo compared to other metals are the ability to withstand the high process temperature during CIGSSe deposition [24, 25], the formation of $MoSe_2$ at the Mo/CIGSSe junction which has an excellent ohmic contact property [26, 27], and the chemical stability or low chemical reaction between Mo and CIGSSe [28-30]. Moreover, the Mo layer and its unique structural characteristics enable the movement of sodium ions from the glass substrate to the CIGS absorber layer [31]. Several other materials have been tested as alternative back contacts for CIGSSe solar cells and so far none have come close to surpass Mo [27, 32-34].

Generally, high quality thin film Mo back contacts were fabricated by magnetron sputtering method. The microstructure of Mo thin film is crucial for the formation of $MoSe_2$ at the interface, Na diffusion from glass substrate to absorber, and the layer-to-layer adhesion [26, 29, 35, 36]. As an example, low deposition pressure tends to result in low electrical resistivity but poor adhesion, while high deposition pressure has been found to produce porous film with good adhesion albeit higher electrical resistivity [29, 30, 37].

2.2.3 Cu(In,Ga)(S,Se)$_2$ p-type Absorber Layer

The I-III-VI$_2$ ternary compounds like Cu(In,Ga)(S,Se)$_2$ are extensions of the II-IV compound semiconductors. They formed a chalcopyrite crystal structure (Figure 2-2 (a)), which can be regarded as a superposition of the zinc blend or the sphalerite structure (Figure 2-2 (b)) [38]. The ternary compound can be further modified by atom substitution of cation and anion with another element in the same group. The substitution of elements with another affect the lattice constant; S replacement of Se atom will shorten the *a* lattice parameter, while Ga replacement of In atom will shorten both the *a* and *c* lattice constants [39]. Therefore, the addition of Ga and S will result in the widening of the CIGSSe band gap as illustrated in Figure 2-3.

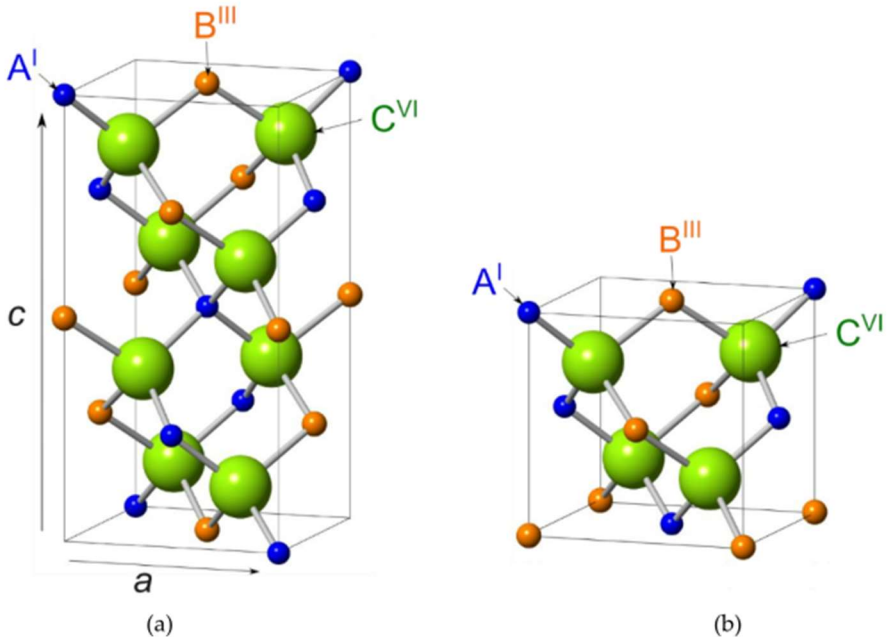

Figure 2-2 Schematic diagrams of (a) chalcopyrite and (b) sphalerite structure.

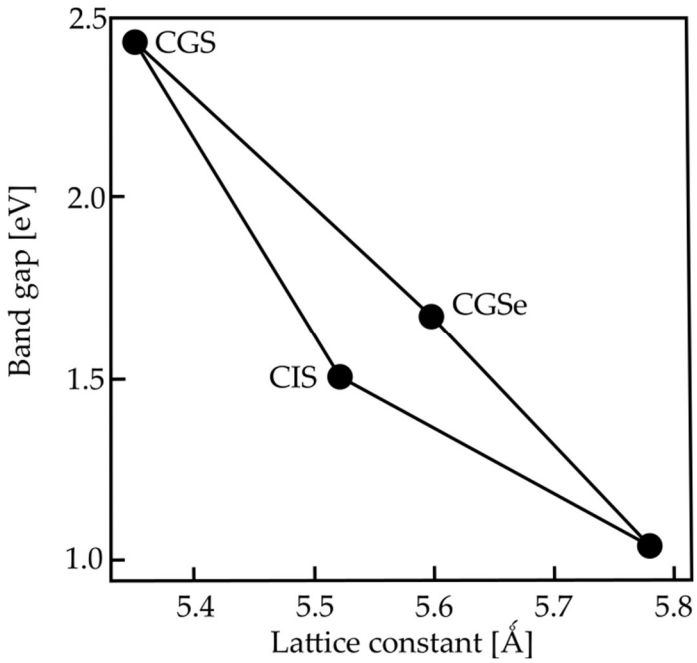

Figure 2-3 Lattice constants and band gap of $Cu(In,Ga)(Se,S)_2$ system.

Maeda *et al.* in [40] empirically investigated the effect of Ga- and S-content in CIGSSe absorber onto the conduction band minimum (CBM) and the valence band maximum (VBM) from a film prepared by a mechanochemical process of elemental powders and post-annealing at 550 °C for 30 min in a N_2 atmosphere. The CBM of each sample was estimated from the diffuse reflectance *R*% spectrum while the VMBs were measured by photoelectron yield spectroscopy (PYS). The authors found that the band-gap energy of the CIGSSe system increased with higher Ga and S contents. The VBM level did not significantly change with increasing Ga content but became deeper with increasing S content. Additionally, the CBM level increased with higher Ga and S content. By controlling the GGI and SSSe

ratios, the researchers were able to design depth profiles for the VBM and CBM energy levels in the CIGSSe absorber layer. The substitution of S for Se resulted in a decreased VBM and an increased CBM at the surface and grain boundaries of the material, effectively reducing electron-hole recombination by acting as a hole-blocking layer. The effects were mapped on the Figure 2-4 below.

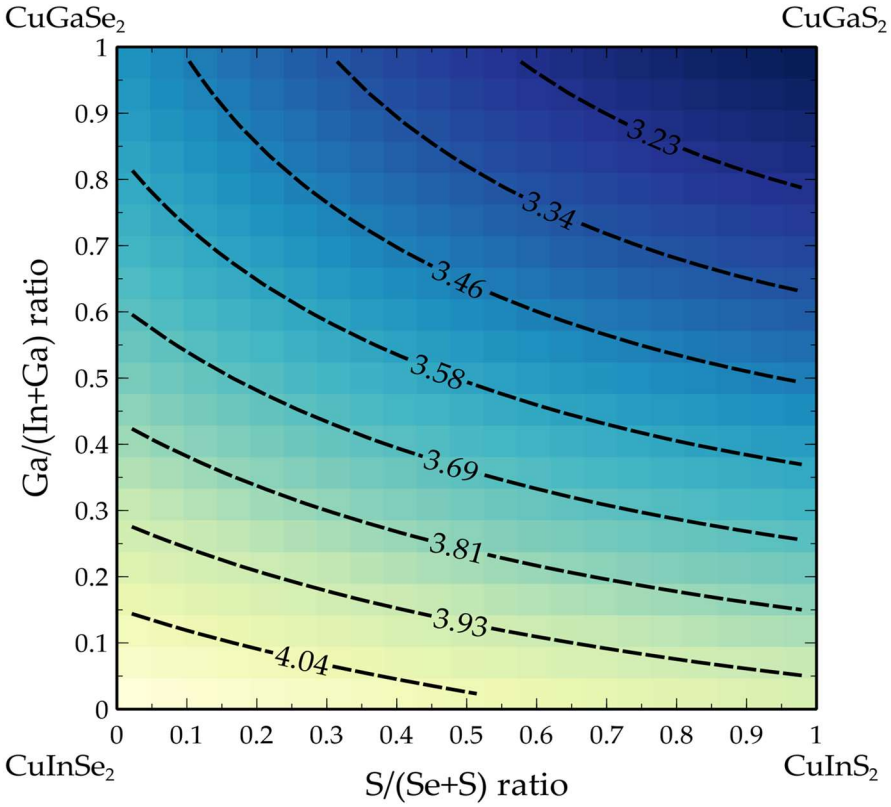

Figure 2-4 Mapping of the CIGSSe absorber's electron affinity, relative to the vacuum level for various Ga/[Ga + In] and S/[S + Se] ratios.

2.2.4 Buffer and Window Layers

To facilitate the generation, separation, and collection of electrical carriers, a transparent material(s), conductive for the minority carrier of the absorber is required to be coupled with the absorber layer. For p-type CIGSSe absorber, transparent conductive materials are good candidates for this purpose. For conventional CIGSSe-based photovoltaics, buffer and window layers are often stacked together to optimise the performance of the photovoltaic device.

A buffer layer is typically inserted between the absorber layer and the window layer. The addition of a thin CdS buffer layer to the CIGSSe-based solar cell marked a significant breakthrough in 1987, enabling chalcopyrite thin film cells to achieve efficiencies exceeding 12% [41]. Buffer layer on CIGSSe-based photovoltaics is believed to prevent chemical reaction between the absorber and the window layers, protect the absorber layer for any deposition damage through the rest of the manufacturing process, prevent shunting between the absorber and the window layers, enhance carrier transport from the absorber to the window layer, and provide good lattice matching to minimise strain and interfacial defects [42, 43].

CdS material has consistently been favoured and has garnered significant attention and interest from numerous researchers due to its emergence as a promising buffer material for thin-film heterojunction solar

cells with high efficiency such as CIGSSe or CdTe [44]. The chemical bath deposition (CBD) method is the commonly used technique for depositing the CdS buffer layer. In this method, thiourea ($CS(NH_2)_2$) is employed as the sulfur source, while a cadmium-ammonia solution derived from cadmium salt ($Cd(CH_3COOH)_2$) is used as the source of cadmium [45]. Achieving the appropriate thickness and uniformity of the CdS film is critical for maximizing the efficiency of the solar cell. Moreover, the CBD process serves as an etching method, effectively removing impurities and excess copper from the surface of the CIGSSe material. Previous research has also demonstrated that the CBD process leads to the formation of a buried junction between the n-type CIGSSe and p-type CIGSSe layers at the interface with CdS, resulting in the creation of a CIGS homojunction [46, 47].

The window layer typically consists of a transparent and conductive material that enables the transmission of light while facilitating the effective capture of charge carriers (electrons or holes) that are produced by the incident light. For CIGSSe-based photovoltaics, the window layer often consists of two layers: High Resistance Window (HRW) and Low Resistance Window (LRW). In certain works, HRW is described as a secondary buffer layer or intermediate layer. The main purpose of HRW layer is believed to be similar to the buffer layer i.e., preventing shunt resistance [48]. On the other hand, LRW is expected to provide maximum electrical conductivity at minimum optical absorption. Similar materials are used for HRW and

LRW, with dopant often used to significantly reduced the resistivity of the chosen material for LRW application.

The conventional approach for producing In_2O_3:Sn (ITO) involves DC sputtering in an Ar:O_2 mixture. The sputtering targets consist of In_2O_3 (90%) and SnO_2 (10%), and the typical substrate temperature during deposition is 250°C. Although sputtering is more costly than chemical vapor deposition, it is compatible with the production of both superstrate and substrate-type solar cells due to the relatively low substrate temperature. It appears that ITO possesses an indirect band gap of approximately 2.4 eV [49]. ITO films exhibit remarkably low resistivity and a higher σ/α value compared to SnO_2:F [50].

ZnO have been doped with Al, Ga, In, B, and F is used in chemical vapor deposition [51]. Sputtering of low-resistance ZnO can be conducted at a low substrate temperature, such as 100°C. Higher substrate temperatures, however, lead to improved values of σ/α. Doped films can be deposited using radio frequency, midfrequency, and DC sputtering. Deposition of ZnO through chemical vapour deposition (CVD) can be done through the vapourisation of diethylzinc ($(C_2H_5)_2Zn$), as the Zn source, and distilled water, as the oxide source. The vapour transported into the reaction chamber through inert gas like Ar. High substrate temperature has been shown to have detrimental impact to the carrier mobility [52]. An aqueous or gaseous solution is used as a dopant source, such as B_2H_6 for B.

2.3 Technology Advancement in CIGSSe Photovoltaics

2.3.1 CIGSSe Tandem Solar Cell

There are two significant challenges and design requirements for monolithic tandem solar cells are discussed, namely current matching between the cells and material compatibility. The band gap tunability of CIGSSe solar cells makes them attractive for tandem solar cell applications. By adjusting the Ga/In or S/Se composition ratio in the absorber material, the band gap and current can be tailored to a specific wavelength range. This flexibility allows CIGSSe to function as either the top or bottom cell in a tandem configuration, pairing with various materials to match the properties of the other sub-cell. However, to ensure material compatibility, the possibility of CIGSSe/CIGSSe tandem solar cells should also be considered in future research.

The current champion CIGSSe cell, with an efficiency of 23.35%, has a band gap of 1.08 eV [12], making it suitable as the bottom cell in a tandem solar cell. Previous studies have explored several tandem configurations using narrow band gap CIGSSe as the bottom cell, such as perovskite/CIGSe [53-55] or DSSC/CIGSe [56-58]structures. Additionally, chalcogenide cells employing CdTe/CIGSe have been investigated, achieving a certified efficiency of 15.3% [59]. Unfortunately, none of the previously

studied all CIGSSe tandem solar cells have surpassed an efficiency of 10% [60, 61].

One of the major challenges in achieving high efficiency for CIGSSe solar cells is the poor performance of wide band gap cells, particularly those with high Ga composition [62-64]. It has been observed that single junction CIGSSe solar cells with high Ga content tend to exhibit smaller grain sizes, lower short-circuit current (J_{SC}), and increased interfacial recombination [65]. Up to recently, the majority of research in the field have focused on narrow band gap CIGSSe, a new approach is necessary to realize high efficiency in all CIGSSe tandem solar cells.

A promising perspective is the development of pure-sulfide CIGS solar cells. The band gap of pure-sulfide CIGS solar cells can be adjusted within the range of 1.5-2.4 eV, whereas pure selenide CIGSe solar cells have a range of 1.0-1.7 eV [66, 67]. This indicates that achieving wide band gap CIGS with low Ga content is more feasible using pure-sulfide CIGS materials. Currently, the highest reported efficiency for pure-sulfide CIGS solar cells is 15.5% with a band gap of 1.57 eV [68].

2.3.2 Alternative n-type Buffer Layer Material

In their work [69], Gloeckler and Sites examined various factors that could potentially restrict the efficiency of wide band gap $CIGSe_2$ solar cells using SCAPS-1D simulation software. Their study focused on

adjusting the band gap of $CIGSe_2$ solar cells by manipulating the conduction band minimum of the $CIGSe_2$ absorber, which is primarily influenced by the Ga/In ratio. Consequently, this adjustment also affected the conduction band offset between the absorber and the window layer. For their calculations, they assumed a ZnO/CdS window layer combination.

Through their simulations, Gloeckler and Sites discovered that in cases where the conduction band offset between the window and absorber was zero or negative (indicative of wide band gap $CIGSe_2$), small interfacial recombination became a limiting factor for the open circuit voltage. They concluded that the commonly used ZnO/CdS window layer, which is suitable for narrow band gap $CIGSe_2$, is not optimal for wide band gap applications. As an alternative, they proposed using a Zn(O,S) compound, as experimental results have shown that the addition of sulfur can increase the conduction band minimum of ZnO [70]. Additionally, they observed that achieving wide band gap absorbers through valence band maximum control led to solar cells with higher open circuit voltages.

Merdes *et al.* suggested that, similar to narrow band gap $CIGSe_2$ solar cells, the control of band gap through the Ga/In composition ratio is crucial for wide band gap $CIGS_2$ solar cells [71]. In their study, they increased the sulfurization temperature of the sputtered precursor containing CuGa/CuIn from 510°C in their previous research [72] to 560°C and introduced a short high-temperature phase at 630°C to promote interdiffusion

between the Ga-rich and In-rich phases. They observed that although their previous results showed a tendency for higher V_{OC} due to the front grading, their modified deposition process yielded higher efficiency due to smoother back grading and flatter front grading. CdS/$CIGS_2$ device structures were employed in these studies conducted by Merdes *et al*.

Hiroi *et al*. achieved the current highest record for pure sulfide $CIGS_2$ solar cells at 15.5% by replacing CdS with $Zn_{1-x}Mg_xO$ as the buffer layer in a ZnO/CdS/$CIGS_2$ device structure [68]. The new buffer material managed to increase the short circuit current compared to CdS. However, as other studies have suggested, matching the conduction band minimum is crucial in achieving higher V_{OC}. In this study, Hiroi *et al.* achieved improved conduction band minimum matching between the buffer layer and the absorber by increasing the Mg concentration from Mg/(Mg+Zn) = 0.193 to Mg/(Mg+Zn) = 0.242, which increased the band gap of the $Zn_{1-x}Mg_xO$ material [73].

2.3.3 Buffer-free CIGSSe

Buffer-free CIGSSe solar cells have emerged as a promising research area. These cells aim to simplify the device structure by eliminating the need for a buffer layer between the CIGSSe absorber and the transparent conducting oxide (TCO) layer. Although the fabrication processes for CIGSSe solar cells are predominantly carried out using dry methods, the

application of buffer layers typically involves wet solution processes. By directly interfacing the CIGSSe absorber with the TCO layer, buffer-free CIGSSe solar cells offer potential cost savings in the manufacturing process and reduced material usage.

Minemoto and Julayhi demonstrated in [74] the first empirical result of buffer-free CIGSe photovoltaic device using a novel TCO material of $ZnO_{1-x}S_x$:Al. The alloying of S into the conventional TCO material, ZnO:Al, improved the device efficiency from 1.7% to 8.4%. All the other device characteristics such as V_{OC}, J_{SC}, and fill factor all improved. The authors suggested that the novel material addressed the shunting issue on the TCO/absorber interface. However, the performance of a Al–NiCr grid/AZOS/CdS/CIGS/Mo/soda-lime glass (SLG) device is still superior than the Cd-free counterpart in regard to V_{OC}, efficiency, and fill factor.

References

[1] J. Wang *et al.*, "Fabrication of CdTe thin films grown by the two-step electrodeposition technique on Ni foils," *Journal of Alloys and Compounds,* vol. 636, pp. 97-101, 2015.

[2] T. D. Lee and A. U. Ebong, "A review of thin film solar cell technologies and challenges," *Renewable and Sustainable Energy Reviews,* vol. 70, pp. 1286-1297, 2017.

[3] S. Ishizuka *et al.*, "Physical and chemical aspects at the interface and in the bulk of CuInSe 2-based thin-film photovoltaics," *Physical Chemistry Chemical Physics,* vol. 24, no. 3, pp. 1262-1285, 2022.

[4] N. H. Raad *et al.*, "Improving the electronic and optical properties of chalcogenide Cu2ZnSnS4 compound with transition metal dopants: A first-principles investigation," *Thin Solid Films,* vol. 766, p. 139653, 2023.

[5] M. Powalla, S. Paetel, E. Ahlswede, R. Wuerz, C. D. Wessendorf, and T. Magorian Friedlmeier, "Thin‐film solar cells exceeding 22% solar cell efficiency: An overview on CdTe-, Cu (In, Ga) Se2-, and perovskite-based materials," *Applied Physics Reviews,* vol. 5, no. 4, p. 041602, 2018.

[6] J. Ramanujam *et al.*, "Flexible CIGS, CdTe and a-Si:H based thin film solar cells: A review," *Progress in Materials Science,* vol. 110, pp. 100619-100619, 2020/5// 2020.

[7] M. I. Khalil *et al.*, "CZTS thin film solar cells on flexible Molybdenum foil by electrodeposition-annealing route," *Journal of Applied Electrochemistry,* vol. 51, no. 2, pp. 209-218, 2021/2// 2021.

[8] S. Shi *et al.*, "Recent progress in the high-temperature-resistant PI substrate with low CTE for CIGS thin-film solar cells," *Materials Today Energy,* vol. 20, pp. 100640-100640, 2021/6// 2021.

[9] C. Zhang *et al.*, "High efficiency CIGS solar cells on flexible stainless steel substrate with SiO2 diffusion barrier layer," *Solar Energy,* vol. 230, pp. 1033-1039, 2021/12// 2021.

[10] B. Saparov, "Next generation thin-film solar absorbers based on chalcogenides," *Chemical Reviews,* vol. 122, no. 11, pp. 10575-10577, 2022.

[11] S. Philipps and W. Warmuth, "Photovoltaics report fraunhofer institute for solar energy systems," *ISE with Support of PSE GmbH November 14th; Fraunhofer ISE: Freiburg, Germany,* 2019.

[12] M. Nakamura, K. Yamaguchi, Y. Kimoto, Y. Yasaki, T. Kato, and H. Sugimoto, "Cd-Free Cu(In,Ga)(Se,S)2 thin-film solar cell with record

efficiency of 23.35%," *IEEE Journal of Photovoltaics,* vol. 9, no. 6, pp. 1863-1867, 11 2019.

[13] F. Solar. "First Solar, Inc. - First Solar Achieves Yet Another Cell Conversion Efficiency World Record", https://investor.firstsolar.com/news/press-release-details/2016/First-Solar-Achieves-Yet-Another-Cell-Conversion-Efficiency-World-Record/default.aspx. [Accessed on 05/16/2023]

[14] R. J. Matson, K. A. Emery, and R. E. Bird, "Terrestrial solar spectra, solar simulation and solar cell short-circuit current calibration: a review," *Solar cells,* vol. 11, no. 2, pp. 105-145, 1984.

[15] Z. J. Li‐Kao *et al.*, "Towards ultrathin copper indium gallium diselenide solar cells: proof of concept study by chemical etching and gold back contact engineering," *Progress in Photovoltaics: Research and Applications,* vol. 20, no. 5, pp. 582-587, 2012.

[16] P. Blösch *et al.*, "Alternative back contact designs for Cu (In, Ga) Se2 solar cells on polyimide foils," *Thin Solid Films,* vol. 535, pp. 220-223, 2013.

[17] J. Ramanujam and U. P. Singh, "Copper indium gallium selenide based solar cells–a review," *Energy & Environmental Science,* vol. 10, no. 6, pp. 1306-1319, 2017.

[18] R. H. Boyd, "Relaxation processes in crystalline polymers: experimental behaviour—a review," *Polymer,* vol. 26, no. 3, pp. 323-347, 1985.

[19] M. Aleksandrova, "Specifics and challenges to flexible organic light-emitting devices," *Advances in Materials Science and Engineering,* vol. 2016, 2016.

[20] S. Shi *et al.*, "Recent progress in the high-temperature-resistant PI substrate with low CTE for CIGS thin-film solar cells," *Materials Today Energy,* vol. 20, p. 100640, 2021/06/01/ 2021.

[21] P. Blösch *et al.*, "Comparative Study of Different Back-Contact Designs for High-Efficiency CIGS Solar Cells on Stainless Steel Foils," *IEEE Journal of Photovoltaics,* vol. 1, no. 2, pp. 194-199, 2011.

[22] T. Nakada, D. Iga, H. O. Hiroki Ohbo, and A. K. Akio Kunioka, "Effects of Sodium on Cu(In, Ga)Se2-Based Thin Films and Solar Cells," *Japanese Journal of Applied Physics,* vol. 36, no. 2R, p. 732, 1997/02/01 1997.

[23] L. Kronik, D. Cahen, and H. W. Schock, "Effects of Sodium on Polycrystalline Cu(In,Ga)Se2 and Its Solar Cell Performance," *Advanced Materials,* vol. 10, no. 1, pp. 31-36, 1998.

[24] S. Raud and M.-A. Nicolet, "Study of the CuInSe2/Mo thin film contact stability," *Thin Solid Films,* vol. 201, no. 2, pp. 361-371, 1991.

[25] P. Pradhan *et al.*, "Effect of molybdenum deposition temperature on the performance of CuIn1− xGaxSe2 solar cells," in *2015 IEEE 42nd Photovoltaic Specialist Conference (PVSC)*, 2015, pp. 1-4: IEEE.

[26] T. Wada, N. Kohara, S. Nishiwaki, and T. Negami, "Characterization of the Cu (In, Ga) Se2/Mo interface in CIGS solar cells," *Thin Solid Films,* vol. 387, no. 1-2, pp. 118-122, 2001.

[27] D. Abou-Ras *et al.*, "Formation and characterisation of MoSe2 for Cu (In, Ga) Se2 based solar cells," *Thin Solid Films,* vol. 480, pp. 433-438, 2005.

[28] Y. Huang, S. Gao, Y. Tang, J. Ao, W. Yuan, and L. Lu, "The multi-functional stack design of a molybdenum back contact prepared by pulsed DC magnetron sputtering," *Thin Solid Films,* vol. 616, pp. 820-827, 2016.

[29] W. Li, X. Yan, A. G. Aberle, and S. Venkataraj, "Analysis of microstructure and surface morphology of sputter deposited molybdenum back contacts for CIGS solar cells," *Procedia Engineering,* vol. 139, pp. 1-6, 2016.

[30] Z.-H. Li, E.-S. Cho, and S. J. Kwon, "Molybdenum thin film deposited by in-line DC magnetron sputtering as a back contact for Cu (In, Ga) Se2 solar cells," *Applied surface science,* vol. 257, no. 22, pp. 9682-9688, 2011.

[31] J. H. Yun *et al.*, "Fabrication of CIGS solar cells with a Na-doped Molayer on a Na-free substrate," *Thin Solid Films,* vol. 515, no. 15, pp. 5876-5879, 5 2007.

[32] M. J. Shin *et al.*, "Ultrathin Cu(In,Ga)Se2 transparent photovoltaics: an alternative to conventional solar energy-harvesting windows," *Nano Energy,* vol. 92, p. 106711, 2022/02/01/ 2022.

[33] J. Keller, L. Stolt, O. Donzel-Gargand, T. Kubart, and M. Edoff, "Wide-Gap Chalcopyrite Solar Cells with Indium Oxide–Based Transparent Back Contacts," *Solar RRL,* vol. 6, no. 8, p. 2200401, 2022.

[34] K. Orgassa, H. W. Schock, and J. Werner, "Alternative back contact materials for thin film Cu (In, Ga) Se2 solar cells," *Thin Solid Films,* vol. 431, pp. 387-391, 2003.

[35] P. Bommersbach *et al.*, "Influence of Mo back contact porosity on co‐evaporated Cu (In, Ga) Se2 thin film properties and related solar cell," *Progress in Photovoltaics: Research and Applications,* vol. 21, no. 3, pp. 332-343, 2013.

[36] L. Assmann, J. Bernede, A. Drici, C. Amory, E. Halgand, and M. Morsli, "Study of the Mo thin films and Mo/CIGS interface properties," *Applied Surface Science,* vol. 246, no. 1-3, pp. 159-166, 2005.

[37] K. Aryal, H. Khatri, R. W. Collins, and S. Marsillac, "In Situ and Ex Situ Studies of Molybdenum Thin Films Deposited by

rf and dc Magnetron Sputtering as a Back Contact for CIGS Solar Cells," *International Journal of Photoenergy*, vol. 2012, p. 723714, 2012/04/11 2012.

[38] B. R. Pamplin, T. Kiyosawa, and K. Masumoto, "Ternary chalcopyrite compounds," *Progress in Crystal Growth and Characterization*, vol. 1, no. 4, pp. 331-387, 1979/01/01/ 1979.

[39] S. Abrahams and J. Bernstein, "Piezoelectric nonlinear optic CuGaS2 and CuInS2 crystal structure: Sublattice distortion in AIB III C 2 VI and A II B IV C 2 V type chalcopyrites," *The Journal of Chemical Physics*, vol. 59, no. 10, pp. 5415-5422, 1973.

[40] T. Maeda, R. Nakanishi, M. Yanagita, and T. Wada, "Control of electronic structure in Cu (In, Ga)(S, Se) 2 for high-efficiency solar cells," *Japanese Journal of Applied Physics*, vol. 59, no. SG, p. SGGF12, 2020.

[41] K. Mitchell, R. Potter, J. Ermer, R. Wieting, and C. Eberspacher, "High efficiency thin film tandem PV modules," in *19th IEEE Photovoltaic Specialists Conference*, 1987, pp. 13-18.

[42] T. Nakada, M. Mizutani, Y. Hagiwara, and A. Kunioka, "High-efficiency Cu (In, Ga) Se2 thin-film solar cells with a CBD-ZnS buffer layer," *Solar energy materials and solar cells*, vol. 67, no. 1-4, pp. 255-260, 2001.

[43] P. Reyes and S. Velumani, "Structural and optical characterization of mechanochemically synthesized copper doped CdS nanopowders," *Materials Science and Engineering: B,* vol. 177, no. 16, pp. 1452-1459, 2012.

[44] A. Ashok, G. Regmi, A. Romero-Núñez, M. Solis-López, S. Velumani, and H. Castaneda, "Comparative studies of CdS thin films by chemical bath deposition techniques as a buffer layer for solar cell applications," *Journal of Materials Science: materials in Electronics,* vol. 31, pp. 7499-7518, 2020.

[45] D. Lincot, M. Froment, and H. Cachet, "Chemical deposition of chalcogenide thin films from solution," *Advances in electrochemical science and engineering,* vol. 6, pp. 165-235, 1999.

[46] S.-W. Park *et al.*, "Dependence of Cu (In, Ga) Se2 Solar Cell Performance on Cd Solution Treatment Conditions," *Molecular Crystals and Liquid Crystals,* vol. 551, no. 1, pp. 221-227, 2011.

[47] C.-S. Jiang, F. Hasoon, H. Moutinho, H. Al-Thani, M. Romero, and M. Al-Jassim, "Direct evidence of a buried homojunction in Cu (In, Ga) Se 2 solar cells," *Applied Physics Letters,* vol. 82, no. 1, pp. 127-129, 2003.

[48] U. Rau, P. Grabitz, and J. Werner, "Resistive limitations to spatially inhomogeneous electronic losses in solar cells," *Applied Physics Letters,* vol. 85, no. 24, pp. 6010-6012, 2004.

[49] F. Matino *et al.*, "Electronic structure of indium-tin-oxide films fabricated by reactive electron-beam deposition," *Physical Review B,* vol. 72, no. 8, p. 085437, 2005.

[50] R. G. Gordon, "Preparation and properties of transparent conductors," *MRS Online Proceedings Library (OPL),* vol. 426, p. 419, 1996.

[51] K. Ellmer and A. Klein, "ZnO and its applications," *Transparent conductive zinc oxide: basics and applications in thin film solar cells,* pp. 1-33, 2008.

[52] W. W. Wenas, A. Yamada, K. Takahashi, M. Yoshino, and M. Konagai, "Electrical and optical properties of boron ‐ doped ZnO thin films for solar cells grown by metalorganic chemical vapor deposition," *Journal of applied physics,* vol. 70, no. 11, pp. 7119-7123, 1991.

[53] M. Jos ˇ t *et al.*, "Perovskite/CIGS tandem solar cells: from certified 24.2% toward 30% and beyond," *ACS energy letters,* vol. 7, no. 4, pp. 1298-1307, 2022.

[54] N. Shrivastav *et al.*, "Perovskite-CIGS Monolithic Tandem Solar Cells with 29.7% Efficiency: A Numerical Study," *Energy & Fuels,* vol. 37, no. 4, pp. 3083-3090, 2023.

[55] M. Mousa, M. M. Salah, F. Z. Amer, A. Saeed, and R. I. Mubarak, "High efficiency tandem perovskite/CIGS solar cell," in *2020 2nd International Conference on Smart Power & Internet Energy Systems (SPIES)*, 2020, pp. 224-227: IEEE.

[56] S. H. Moon *et al.*, "Monolithic DSSC/CIGS tandem solar cell fabricated by a solution process," *Scientific reports,* vol. 5, no. 1, pp. 1-6, 2015.

[57] S. Y. Chae, S. J. Park, O.-S. Joo, Y. Jun, B. K. Min, and Y. J. Hwang, "Highly stable tandem solar cell monolithically integrating dye-sensitized and CIGS solar cells," *Scientific reports,* vol. 6, no. 1, pp. 1-8, 2016.

[58] D. Xiong and W. Chen, "Recent progress on tandem structured dye-sensitized solar cells," *Frontiers of Optoelectronics,* vol. 5, pp. 371-389, 2012.

[59] X. Wu *et al.*, "High-efficiency CdTe polycrystalline thin-film solar cells with an ultra-thin CuxTe transparent back-contact," *MRS Online Proceedings Library (OPL),* vol. 865, 2005.

[60] T. K. Todorov, D. M. Bishop, and Y. S. Lee, "Materials perspectives for next-generation low-cost tandem solar cells," *Solar Energy Materials and Solar Cells,* vol. 180, pp. 350-357, 2018.

[61] K. Kim *et al.*, "Highly efficient Ag-alloyed Cu (In, Ga) Se2 solar cells with wide band gaps and their application to chalcopyrite-based tandem solar cells," *Nano Energy,* vol. 48, pp. 345-352, 2018.

[62] M. A. Contreras *et al.*, "Wide band gap Cu (In, Ga) Se2 solar cells with improved energy conversion efficiency," *Progress in Photovoltaics: Research and Applications,* vol. 20, no. 7, pp. 843-850, 2012.

[63] J. V. Li, S. Grover, M. A. Contreras, K. Ramanathan, D. Kuciauskas, and R. Noufi, "A recombination analysis of Cu (In, Ga) Se2 solar cells with low and high Ga compositions," *Solar Energy Materials and Solar Cells,* vol. 124, pp. 143-149, 2014.

[64] S. Ishizuka, A. Yamada, P. J. Fons, H. Shibata, and S. Niki, "Impact of a binary Ga2Se3 precursor on ternary CuGaSe2 thin-film and solar cell device properties," *Applied Physics Letters,* vol. 103, no. 14, p. 143903, 2013.

[65] S. Jung, S. Ahn, J. H. Yun, J. Gwak, D. Kim, and K. Yoon, "Effects of Ga contents on properties of CIGS thin films and solar cells fabricated by co-evaporation technique," *Current Applied Physics,* vol. 10, no. 4, pp. 990-996, 2010.

[66] H. W. Spiess, U. Haeberlen, G. Brandt, A. Räuber, and J. Schneider, "Nuclear magnetic resonance in IB–III–VI2 semiconductors," *Physica Status Solidi B,* vol. 62, no. 1, pp. 183-192, 1974.

[67] A. Zunger and J. Jaffe, "Structural origin of optical bowing in semiconductor alloys," *Physical Review Letters,* vol. 51, no. 8, p. 662, 1983.

[68] H. Hiroi, Y. Iwata, S. Adachi, H. Sugimoto, and A. Yamada, "New world-record efficiency for pure-sulfide Cu (In, Ga) S 2 thin-Film solar cell with Cd-free buffer layer via KCN-free process," *IEEE Journal of Photovoltaics,* vol. 6, no. 3, pp. 760-763, 2016.

[69] M. Gloeckler and J. Sites, "Efficiency limitations for wide-band-gap chalcopyrite solar cells," *Thin Solid Films,* vol. 480, pp. 241-245, 2005.

[70] S.-H. Wei and A. Zunger, "Calculated natural band offsets of all II–VI and III–V semiconductors: Chemical trends and the role of cation d orbitals," *Applied Physics Letters,* vol. 72, no. 16, pp. 2011-2013, 1998.

[71] S. Merdes *et al.*, "CdS/Cu (In, Ga) S2 based solar cells with efficiencies reaching 12.9% prepared by a rapid thermal process," *Progress in Photovoltaics: Research and Applications,* vol. 21, no. 1, pp. 88-93, 2013.

[72] S. Merdes *et al.*, "12.6% efficient CdS/Cu (In, Ga) S2-based solar cell with an open circuit voltage of 879 mV prepared by a rapid thermal process," *Solar Energy Materials and Solar Cells,* vol. 95, no. 3, pp. 864-869, 2011.

[73] T. Minemoto, T. Negami, S. Nishiwaki, H. Takakura, and Y. Hamakawa, "Preparation of Zn1− xMgxO films by radio frequency

magnetron sputtering," *Thin solid films,* vol. 372, no. 1-2, pp. 173-176, 2000.

[74] T. Minemoto and J. Julayhi, "Buffer-less Cu (In, Ga) Se2 solar cells by band offset control using novel transparent electrode," *Current Applied Physics,* vol. 13, no. 1, pp. 103-106, 2013.

Chapter 3 Low Electron Affinity Material for Thin-Film Heterojunction Photovoltaics

3.1 Introduction

In this part of the research, we conducted simulations using a wide band gap p-type chalcogenide material with ideal band gap $E_g = 1.5\ eV$ and an arbitrary n-type window layer material as a model. The properties of the n-type window layer were based on the standard n-ZnO combination. However, minor adjustments were made to certain parameters to ensure convergence in specific scenarios during the calculations. For example, instead of using the commonly used band gap value of $E_g^{ZnO} = 3.3\ eV$ [1], we set the band gap for the window layer to $E_g^{window} = 3.0\ eV$. Preliminary evaluations showed no significant difference between the two models.

This part of the study primarily focuses on the simple pn heterojunction window/absorber photovoltaic cell structure. Past empirical results have suggested a major relationship between the conduction band alignment and the open circuit voltage V_{OC} of thin film solar cell devices [2-5]. Therefore, in this work the calculated V_{OC} from the modelled devices will be the benchmark for the solar cell characteristic evaluation.

Considering that in thin-film heterojunction the depletion region may extend well into the absorber layer, photocurrent may be generated both in the bulk and the depletion region with non-uniform generation rate $G(x)$. Therefore, the width of the depletion region W and the electron diffusion length L_e are to be taken into account when estimated the maximum potentially available energy. Thus, theoretical maximum V_{OC} for the simulated models can be calculated through this equation, where α is the absorption coefficient of the absorber material, N_A is the acceptor concentration, n_i is the intrinsic carrier concentration, G is the generation rate, and τ_e is the lifetime of the electron:

$$V_{OC} = \frac{kT}{q} \ln \frac{N_A}{n_i^2} G_0 \tau_e k \qquad \text{Eq. 3.1}$$

$$k = \frac{1}{1 + \alpha L_e} + \frac{e^{\alpha W} - 1}{\alpha L_e} \qquad \text{Eq. 3.2}$$

In Section 3.3, we evaluate the effect of the independent variable under ideal conditions, assuming no defects at the interface. The discussion then moves to the less ideal conditions where interface defects must be taken into account in Section 3.4. Finally, in Section 3.5, we propose two roles of n-type layer in pn-junction solar cell and introduce the physical mechanism related to the roles.

3.2 SCAPS-1D Simulation Software

This study utilizes a simulation software known as SCAPS 1D, which stands for one-dimensional solar cell capacitance simulator. This program was developed by Prof. Marc Burgelman's team at the Department of Electronics and Information System, University of Gent in Belgium [6]. Originally designed for polycrystalline $CuInSe_2$ and CdTe solar cells [6-10], SCAPS 1D has undergone several improvements over the years to accommodate research on crystalline and amorphous solar cells as well [11-14]. It has emerged as a valuable tool for researchers in the field, enabling them to design, evaluate, and validate their work aimed at enhancing the performance of thin film heterojunction solar cells [15-19].

SCAPS 1D specifically addresses various challenges associated with simulating realistic thin film heterojunction solar cells like CIGSSe. These photovoltaic devices exhibit energy band discontinuities between their layers, and while other simulation programs typically consider recombination within the same layer only, SCAPS 1D takes into account the possibility of interfacial recombination between carriers from different layers across the band gap created by the discontinuity. To address this phenomenon, SCAPS 1D incorporates a thin interface dummy layer with its own E_C and E_V values, which are based on the neighbouring layers in the junction and control the energy band states distribution, similar to the bulk material [7]. Additionally, SCAPS 1D allows for the manipulation of material

parameters to reflect the control of alloy composition [16], making it particularly useful for simulating the grading in CIGS solar cells. These capabilities and features make SCAPS 1D the preferred choice for the researchers in this study.

3.3 Window/Absorber Structure with Ideal Interface Condition

3.3.1 Simulation Modelling and Parameters

The initial model used in this study, consisted of a basic pn-junction solar cell with a structure comprising of an absorber layer and a window layer, called Model A. The absorber layer is made of a CIGSSe material with $E_g = 1.5\ eV$ that is close to the band gap for ideal solar cells. In this model, the interface between the layers was assumed to be in an ideal condition, with interface defect concentration $N_t = 0$. The electron affinity of the window layer, denoted as χ^{Window} was varied between $4.45\ eV$ and $4.95\ eV$ in order to examine the impact of various n-type material on a CIGSSe-based single junction solar cell device, especially on the open-circuit voltage (V_{OC}). The diffusion potential also changes accordingly from $1.33\ V$ to $0.83\ V$, dependent on the electron affinity. The V_{OC} calculated through this model represents the maximum achievable V_{OC} for the photovoltaic devices with materials of these particular properties as calculated in Eq. 3.1.

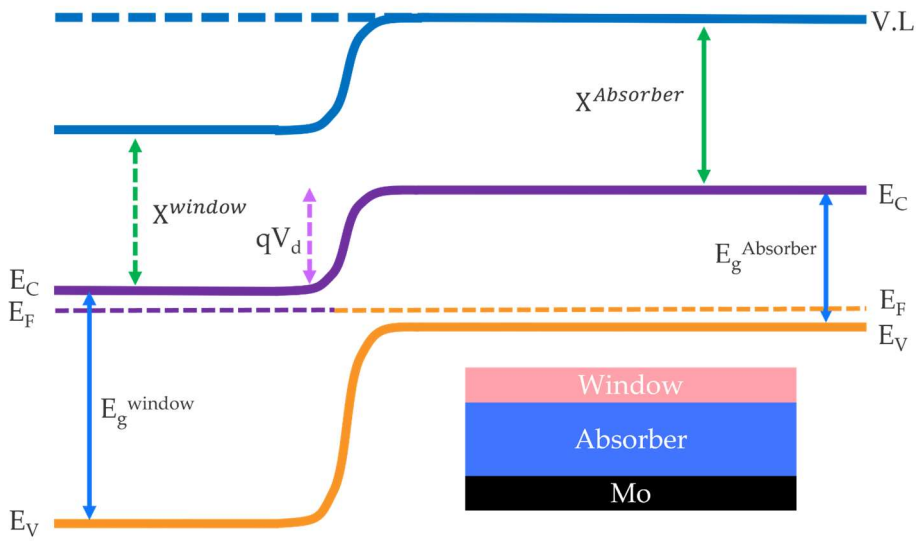

Figure 3-1 Illustration of the simulation model of a heterojunction solar cell with ideal interface condition (Model A).

Table 3-1 SCAPS material parameters for ideal window/absorber heterojunction solar cells structure

	Window Layer	**Absorber**
d (μm)	0.20	3.00
X (eV)	*variable*	4.50
E_g (eV)	3.00	1.50
N_C (cm^{-3})	2.20×10^{18}	2.20×10^{18}
N_V (cm^{-3})	1.80×10^{19}	1.80×10^{19}
N_A (cm^{-3})	-	1.00×10^{16}
N_D (cm^{-3})	1.00×10^{18}	-
N_t (cm^{-2})	0	

The other material parameters used in the simulation are as shown in Table 3-1 where d is the thickness of the layer, X is the electron affinity, E_g is the band gap, N_C is the effective density in the conduction band, N_V is the effective density in the valence band, N_A is the acceptor

concentration, N_D is the dopant concentration, and N_t is the interface defect concentration.

3.3.2 Analysis of Solar Cell Characteristics

To gain further understanding of the effect of n-type layer on a heterojunction photovoltaics, we conducted an evaluation of the impact of varying electron affinity levels in the window layer on solar cell characteristics, specifically the open-circuit voltage V_{OC}, as illustrated in Figure 3-2. The V_{OC} of all the simulated Model A devices are around 1.02 V. This value is close to the theoretical maximum V_{OC} calculated from Eq. 3.1 where $\alpha = 1.00 \times 10^5\ cm^{-1}$, $W = 0.5\ \mu m$, and $L_e = 1.5\ \mu m$. Since no interface defect was considered in the simulation (i.e., ideal condition), therefore it is expected that the V_{OC} will be close to the theoretical maximum V_{OC}.

No significant influence of different levels of electron affinity in the window layer was observed in the calculated V_{OC}. This result differs from some references (e.g., [20-22]) where a decreasing trend in V_{OC} was observed when $X^{window} > X^{absorber}$. In those references, it is suspected that recombination between majority carriers through defects at the window/absorber interface is the cause of V_{OC} loss. Since in this simulation it was assumed a low interface defect concentration at the interface, we can infer that V_{OC} is a characteristic sensitive to the interface.

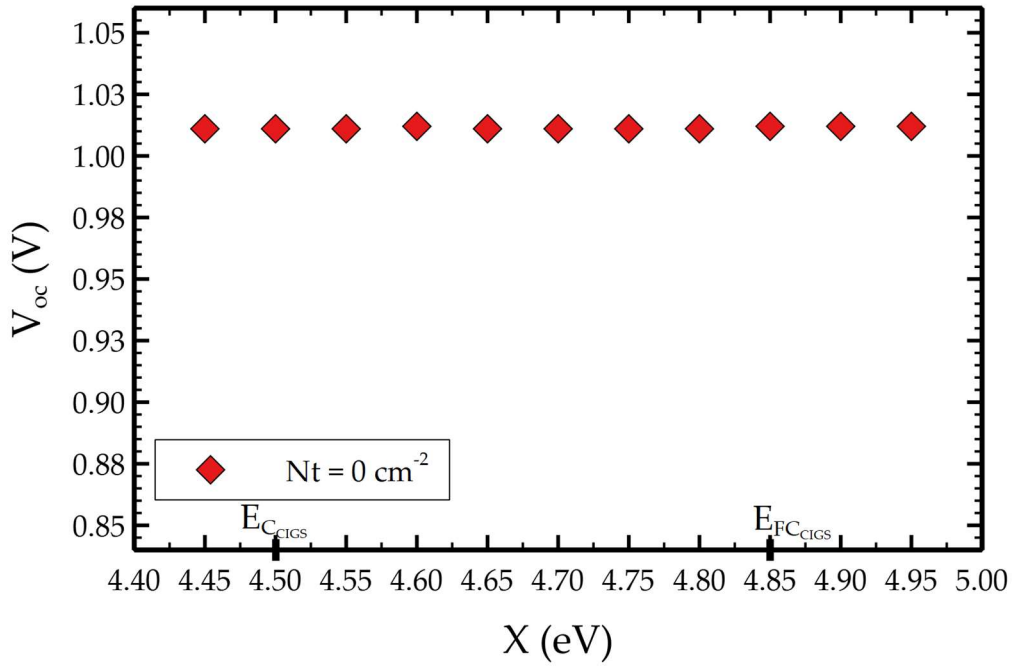

Figure 3-2 The effect of X^{Window} variation on the open-circuit voltage of a heterojunction solar cell with window/absorber structure and an ideal interface condition.

3.3.3 Analysis of Energy Levels Shift in Band Diagram

In a homojunction solar cell, like silicon (Si), the diffusion potential (V_d) is maintained by the capacitance C at the depletion region. The open-circuit condition occurs when there is no gradient present at the interface of the quasi-Fermi distribution of the current-contributing carriers, specifically the electron quasi-Fermi distribution. However, in the case of thin-film heterojunction solar cells, equilibrium may not be achieved at a bias voltage (V_{bias}) equal or lower than V_d due to the heterogeneous nature of the materials involved, as confirmed by the calculation result. V_{bias}

higher than V_d can be applied on the device before it finally reaches open-circuit state at $1.02\,eV$. Therefore, it can be assumed that an additional mechanism may have maintained the capacitance at the pn-junction that, especially for the designs where $\mathrm{X}^{Window} > E_{FC_{CIGS}}$.

To investigate these phenomena further, the impact of V_{bias} under illumination on the devices' energy band shifting was observed. Four points of observation were selected based on the relevant V_{bias} amplitudes. These points are $V_{bias} = 0\,V$ where fermi level splitting occurs under illumnittion, $V_{bias} = 0.82\,V$ which is equal to the diffusion potential V_d of the $\mathrm{X}_{Window} = 4.95\,eV$ design, $V_{bias} = 0.95\,V$ which is equal to the initial quasi-Fermi level difference in both designs, and $V_{bias} = 1.02\,V$ where both devices were shown to reach the open-circuit condition.

Figure 3-1 and Figure 3-3 compare the different relationships between qV_d (thermal equilibrium voltage) and the minimum Quasi-Fermi level splitting $E_{FC} - E_{FV}$ (energy difference between the conduction band edge and the valence band edge) in the two scenarios. The blue arrows represent the minimum $E_{FC} - E_{FV}$ required for a balanced electron concentration throughout the bulk, while the red arrows represent the qV_d that forms after the semiconductor device reaches the thermal equilibrium condition.

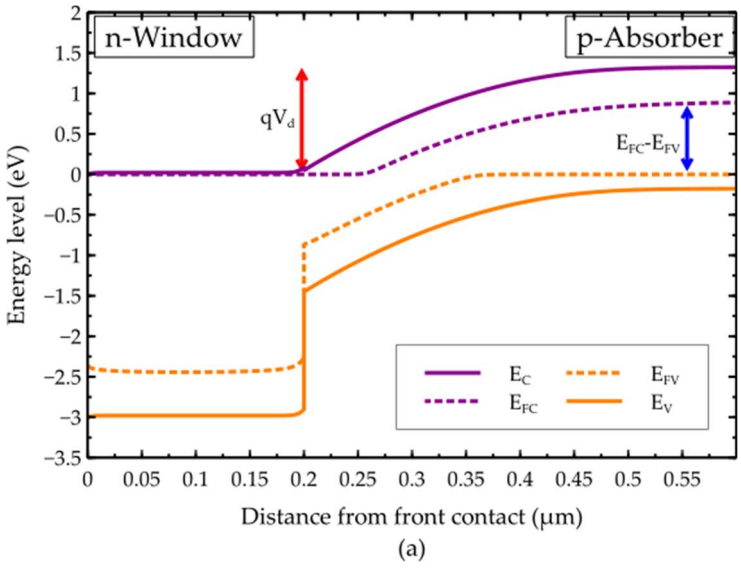

Figure 3-3 The band diagram of a heterojunction solar cell with (a) $X^{window} = 4.45\ eV$ and (b) $X^{window} = 4.95\ eV$ under illumination at $V_{bias} = 0\ V$.

In Figure 3-3 (a), the minimum $E_{FC} - E_{FV}$ is 0.95 eV, and the corresponding qV_d is 1.34 eV. On the other hand, in Figure 3-3 (b), the qV_d is 0.84 eV, while the minimum $E_{FC} - E_{FV}$ remains the same at 0.95 eV. From this figure, it can be deduced that in the scenario depicted in Figure

3-3 (b), the carrier concentration in the p-type and n-type layers will not be equal when $V_{bias} = V_d$.

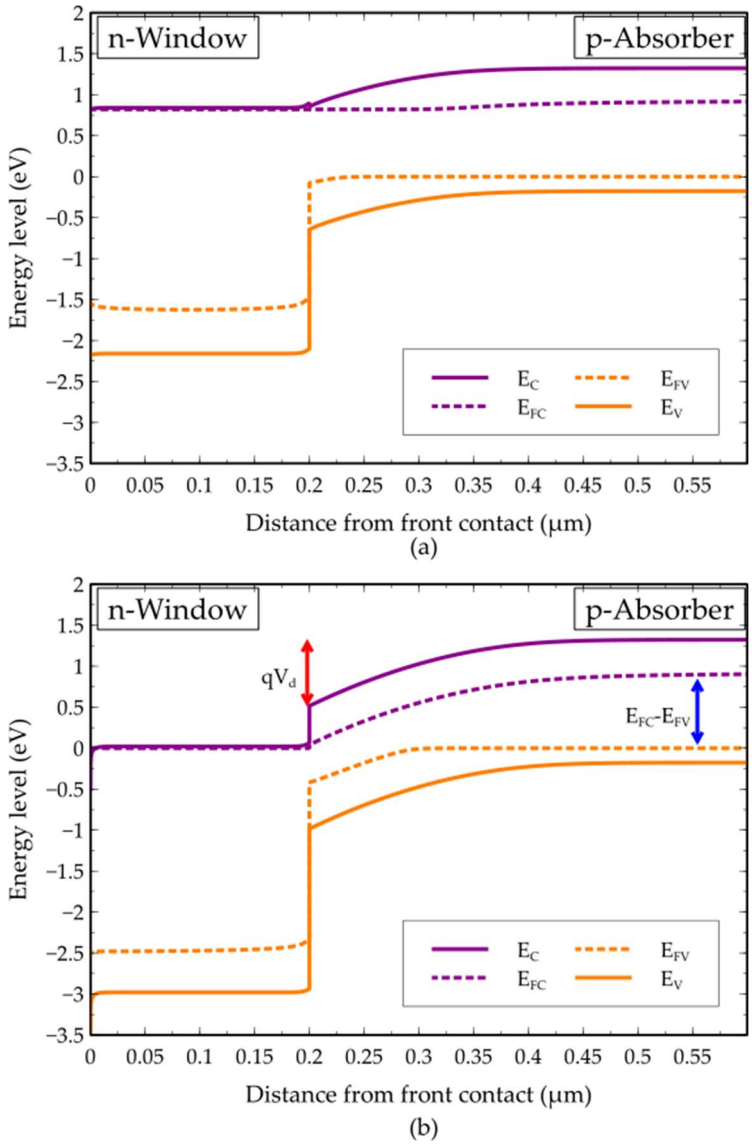

Figure 3-4 The band diagram of a heterojunction solar cell with (a) $X^{window} = 4.45\ eV$ and (b) $X^{window} = 4.95\ eV$ under illumination at $V_{bias} = 0.82\ V$.

The energy bands condition at $V_{bias} = V_d$ are illustrated Figure 3-4. When the biasing voltage is equal to the diffusion potential, the conduction band offset ΔE_C exhibits the maximum bending, resulting in a right angle or a flat region for the E_C at the interface, as shown in Figure 3-4 (b). However, a different situation can be observed in Figure 3-4 (a), where the band bending is still present at the heterojunction interface.

Regarding the Quasi- Fermi level, gradients near the heterojunction interface is still evident for the electron carriers in both Figure 3-4 (a) and Figure 3-4 (b). This indicates that the diffusion of excess electrons from the p-type region to the n-type region continues to occur at this bias level. Therefore, it can be concluded that qV_d at thermal equilibrium is not the limiting factor for the maximum V_{OC} of the device. It merely acts as a potential barrier in achieving thermal equilibrium conditions for the solar cell.

The next important point to consider is the initial quasi-Fermi levels difference $E_{FC} - E_{FV}$ of both solar cell devices at $V_{bias} = 0.95\ V$. As expected, the E_{FC} flattens at the heterojunction interface when E_{FC_p} is equal to E_{FC_n} in both Figure 3-5 (a) and Figure 3-5 (b). However, the calculation results did not indicate that J_{out} is equal to zero at this point. Therefore, it is clear that the minimum $E_{FC} - E_{FV}$ does not determine the maximum limit of V_{OC}. However, this does not immediately invalidate the relationship between V_{OC} and quasi-Fermi level described in Equation 3.42.

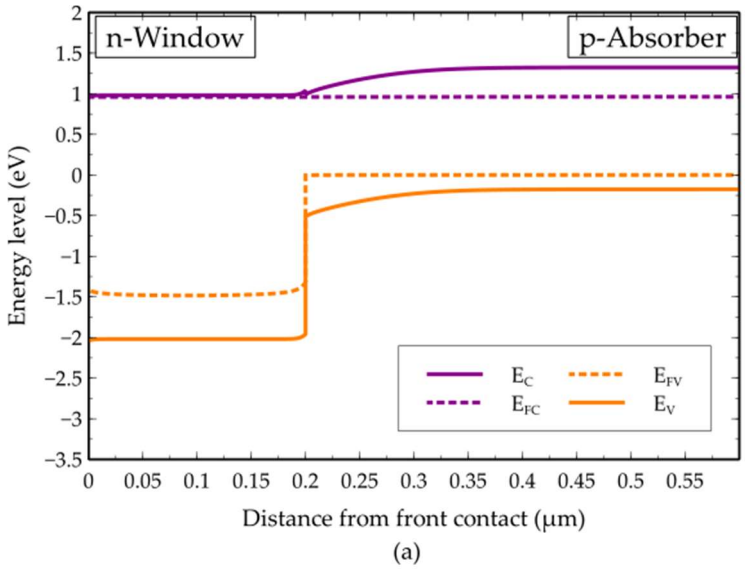

Figure 3-5 The band diagram of a heterojunction solar cell with (a) $X^{window} = 4.45\ eV$ and (b) $X^{window} = 4.95\ eV$ under illumination at $V_{bias} = 0.95\ V$.

The increase in V_{bias} also affect the band discontinuity at the hetero interface. In the case of the photovoltaics device with $X^{Window} = 4.45\ eV$, a small spike was forming at the ΔE_C as illustrated in Figure 3-5 (a). In contrast, it can be observed that notches have started to form on both the ΔE_C

and ΔE_V at the heterojunction interface of the solar cell device with $X^{Window} = 4.95\ eV$. These notches represent the accumulation of the carriers at the heterojunction interface, which are electrons for E_C and holes for E_V.

In order to understand the significance of the energy band notches in this context, it is important to consider the relationship between capacitance C and voltage V, where $V = \frac{Q}{C}$. In the case of a pn-junction device, the depletion region at the pn-interface acts as a capacitor, maintaining a constant potential through the exchange of charges across the junction. Similarly, in homojunction and heterojunction solar cells, on the state where V_d is less than V_{OC}, the depletion region also serves as the source of capacitance, reflected by the potential barrier V_d.

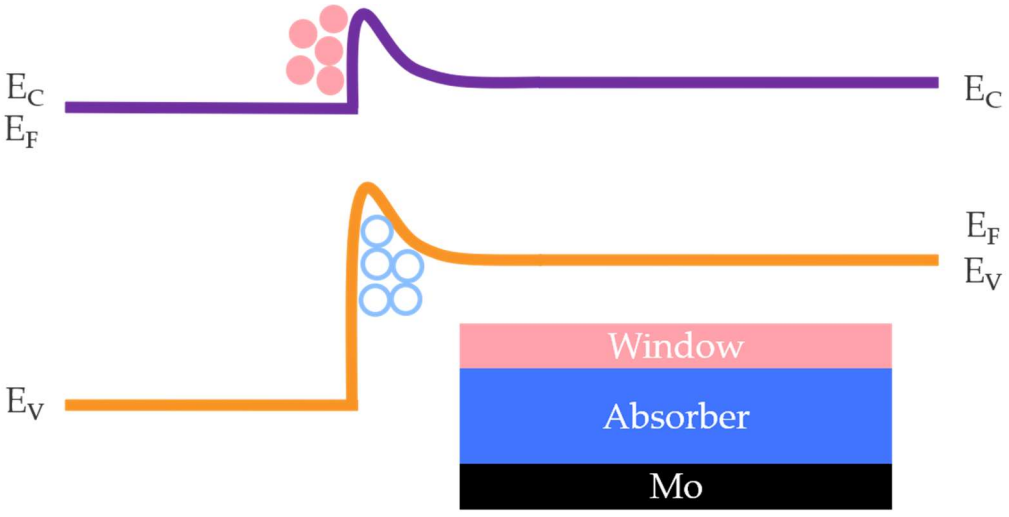

Figure 3-6 Illustration of carriers accumulation at the heterojunction pn-interface of window/absorber solar cell when $V_{bias} > V_d$.

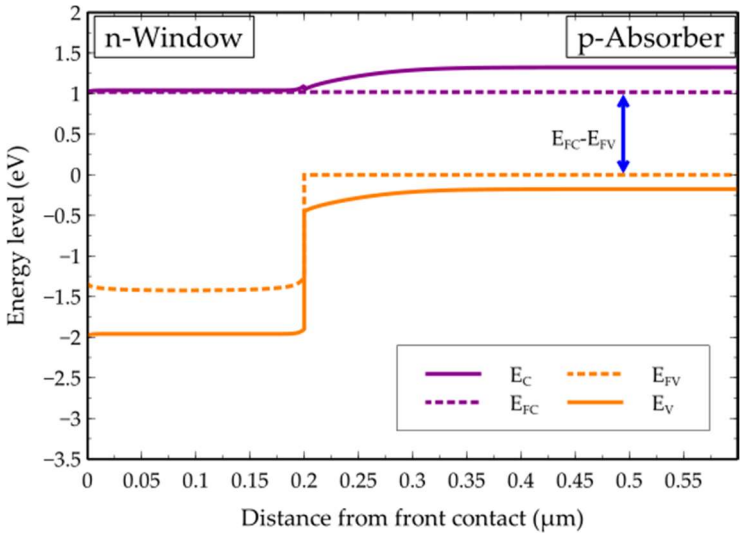

(a)

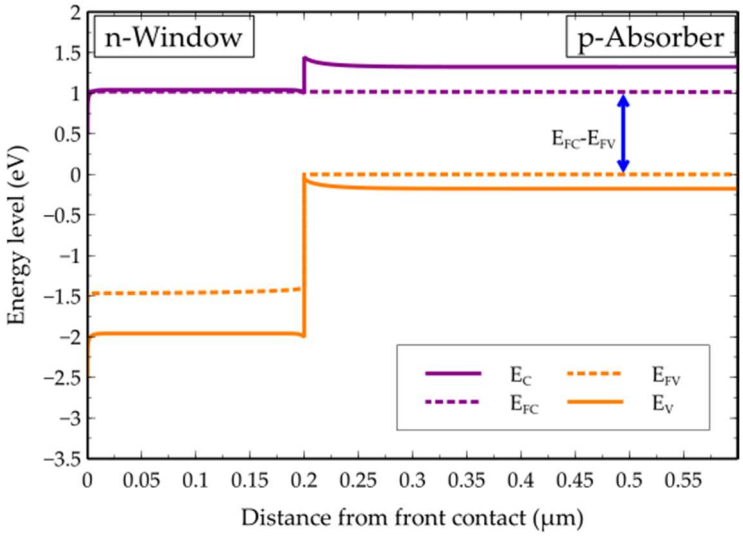

(b)

Figure 3-7 The band diagram of a heterojunction solar cell with (a) $X^{window} = 4.45\ eV$ and (b) $X^{window} = 4.95\ eV$ under illumination at $V_{bias} = 1.02\ V$.

However, in the case of a heterojunction solar cell with X^{window} equal to 4.95 eV, when V_{bias} exceeds V_d another mechanism comes into play to maintain the capacitance at the junction. This mechanism involves the accumulation of carriers at the interface, as illustrated in Figure 3-6. This

new capacitance mechanism enables higher biasing to reach the maximum V_{OC}, regardless of the properties of the window layer. The notches become even more pronounced in Figure 4.8 (b) when the bias voltage is increased to $V_{bias} = 1.02\ V$, which corresponds to the V_{OC} calculated in the simulation considering all variations of X^{window}, as shown in Figure 4.3 (a). It is important to note that the simulation assumes negligible interface defect concentration for this analysis.

The relationship between V_{OC} and the quasi-Fermi distribution is clearly demonstrated in Figure 3-7 (a) and Figure 3-7 (b). In these figures, the $E_{FC} - E_{FV}$ is shown to further increase beyond the minimum $E_{FC} - E_{FV}$ points as V_{bias} increases, until it reaches a value equal to V_{OC}. It is essential to keep in mind that Equation 3.42 is a valid definition of V_{OC} under very specific circumstances, where E_{FC} is equal to E_{FC_n} and E_{FV} is equal to E_{FV_p} in the open circuit condition.

3.4 Window/Absorber Structure with Interface Defect

3.4.1 Simulation Modelling and Parameters

One of the advantages of SCAPS over other solar cell simulation programs, particularly in heterojunction solar cell applications, is its interface layer function (Section 3.2). This function addresses the band gap discontinuity that occurs at the interface, where the conduction band of one material meets the valence band of another material, resulting in a new

Table 3-2 SCAPS material parameters for non-ideal window/absorber heterojunction solar cells structure.

	Window Layer	**Absorber**
d (μm)	0.20	3.00
X (eV)	*variable*	4.50
$\boldsymbol{E_g}$ **(eV)**	3.00	1.50
$\boldsymbol{N_C}$ **(cm^{-3})**	2.20×10^{18}	2.20×10^{18}
$\boldsymbol{N_V}$ **(cm^{-3})**	1.80×10^{19}	1.80×10^{19}
$\boldsymbol{N_A}$ **(cm^{-3})**	$-$	1.00×10^{16}
$\boldsymbol{N_D}$ **(cm^{-3})**	1.00×10^{18}	$-$
$\boldsymbol{qV_D}$ **(eV)**	*variable*	
$\boldsymbol{N_t}$ **(cm^{-2})**	$1.00 \times 10^{11} - 1.00 \times 10^{17}$	
$\boldsymbol{\sigma_e}$ **(cm^2)**	1.00×10^{-15}	
$\boldsymbol{\sigma_h}$ **(cm^2)**	1.00×10^{-15}	

forbidden energy gap. SCAPS allows modification of certain properties of this interface quasi-layer, such as energy level and interface defect concentration, similar to the bulk materials.

In the second simulation model, Model B, we introduced a new material parameter called interface defect concentration N_t at the window/absorber hetero-interface which ranges from $1 \times 10^{11}\ cm^{-2}$ to $1 \times 10^{17}\ cm^{-2}$. The energy trap is located in the middle of the quasi-band gap of the interface, as depicted in Figure 3-8. Additionally, the same variation of X^{window} used in the calculations of Section 3.3 is also applied in this simulation. By conducting this second calculation, the design rule for the window layer under more realistic conditions, considering the presence of an

interface defect, was established. The remaining material parameters remain unchanged as specified in Table 3-2 besides the interface defect contretation N_t, the electron capture cross section σ_e, and the hole capture cross section σ_h.

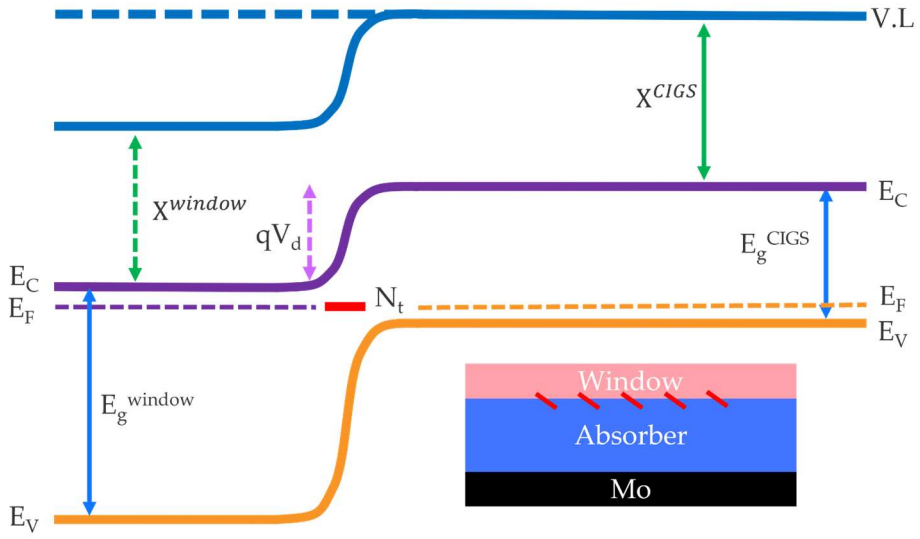

Figure 3-8 Illustration of the simulation model of a heterojunction solar cell with non-ideal window/absorber heterojunction solar cells structure (Model B).

3.4.2 Analysis of Solar Cell Characteristics

The calculation results from Model B demonstrated the crucial role of the interface condition in determining the suitable n-type materials for the window layer in a wide band gap thin-film heterojunction solar cell device. Figure 3-9 provides insights into the general design principle for the window layer, indicating that the defect concentration at the interface establishes the boundaries for acceptable n-type material combinations. The simulation results indicated that achieving high V_{OC} values would allow for

a wider range of alternative n-type materials in devices with lower interface defect concentrations. Conversely, devices with higher Nt values would require more precise design considerations to approach the estimated V_{OC}, as the available options for n-type materials become limited.

3.5 The Roles of N-Type Layer in Realistic Design Condition

3.5.1 N-Type Layer as Interface Passivation

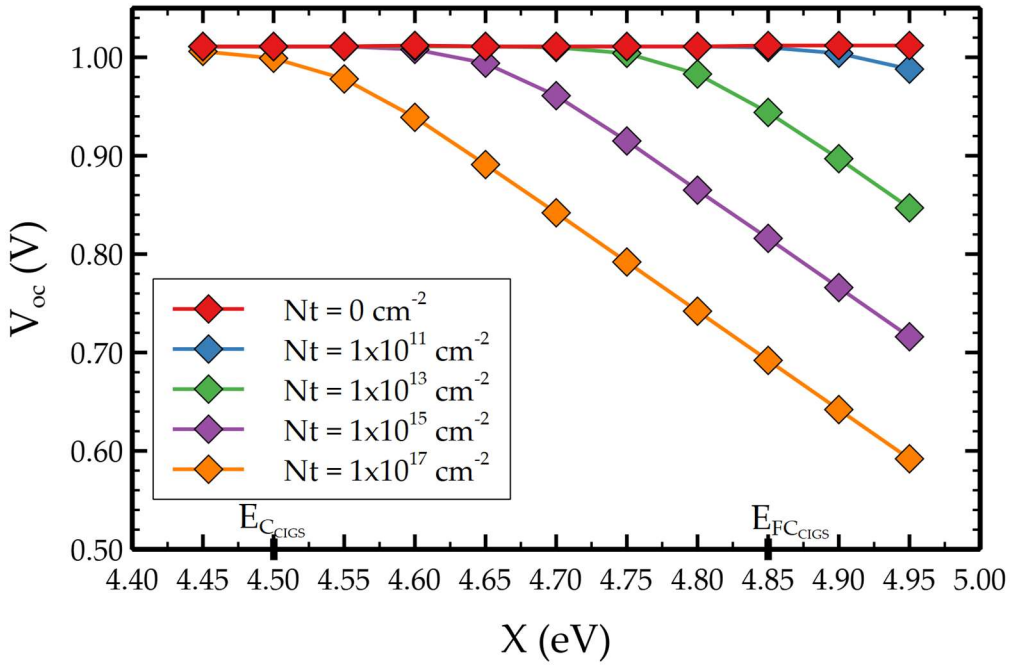

Figure 3-9 The effect of X^{Window} variation on the open-circuit voltage of a heterojunction solar cell with window/absorber structure and a non-ideal interface condition for various N_t values.

The relationship between the n-type layer and interface defects can be understood by considering Figure 3-5, which are simplified in Figure

3-10 (a) and (b). The figure demonstrates the effect of the accumulation of the majority carrier at the pn-junction interface when a bias voltage (V_{bias}) is applied, which is approximately equal to the built-in voltage (V_d). In the first model (Section 3.3.1), where no interface defects were present, recombination did not occur even in extreme cases of window layer high χ^{Window} of 4.95 eV (cliff structure) as illustrated in Figure 3-10 (b). However, in the second model (Section 3.4.1), where non-ideal interface conditions were considered, the increased recombination probability Figure 3-10 (d) due to the majority carrier accumulation at the interface significantly affected the open-circuit voltage (V_{OC}) of the solar cell.

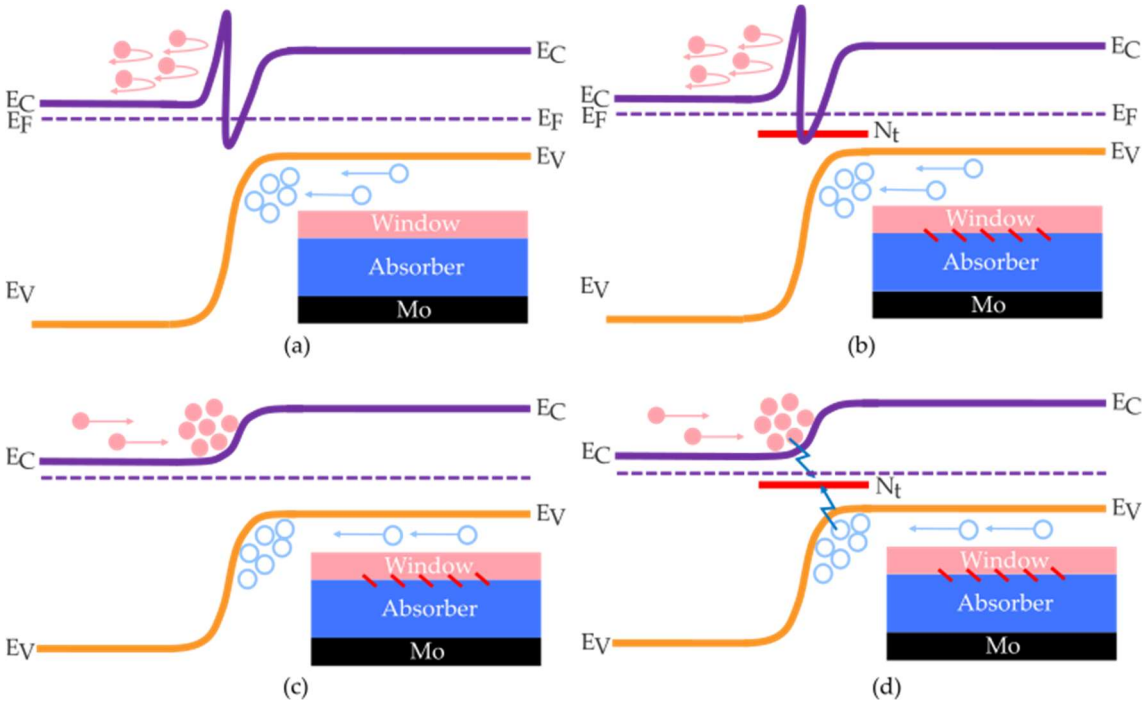

Figure 3-10 Illustration of the interface passivation mechanism for various heterojunction interface conditons. (a) $X^{Window} = 4.45\ eV$; $N_t = 0$, (b) $X^{Window} = 4.45\ eV$; $N_t \neq 0$, (c) $X^{Window} = 4.95 eV$; $N_t = 0$, (d) $X^{Window} = 4.95\ eV$; $N_t \neq 0$.

In Model B, the interface defect acted as an energy trap, leading to trap-assisted recombination, especially when electrons and holes accumulated at the interface. The probability of recombination was also influenced by the interface defect concentration N_t. Higher level of carrier accumulation and higher Nt resulted in a greater recombination probability. Consequently, designs utilizing materials with $\chi^{Window} \geq \chi^{Absorber}$ were disadvantaged compared to designs using low electron affinity materials for the window layer. The use of low electron affinity materials reduced electron accumulation in the conduction band, as shown in Figure 3-10 (c). In this context, the n-type layer functioned as a passivation layer, enabling solar cells with the latter design to maintain a high V_{OC} even at high interface defect concentrations. On the other hand, devices employing high electron affinity n-type materials were significantly affected by the high N_t.

3.5.2 N-Type Layer as Selective Electron Contact

Considering carrier collection, we also examined another aspect of the n-type layer material design. Würfel et al. [23] introduced the concept of carrier conductivity at each contact as the driving force for charge separation in pn-junction solar cells, rather than relying solely on the built-in potential or diffusion potential (V_d). The front contact, which is the n-type layer in this case, is considered selective for electrons when it has high electron conductivity and low hole conductivity. Similarly, the back contact is selective for holes when it exhibits high hole conductivity and low electron

conductivity. A selective contact attracts the desired carrier while repelling the opposite carrier, thereby preventing recombination before the carrier collection. Since conductivity depends on the elemental charge, the carrier concentration, and the mobility, the only controllable variable through material design is the carrier concentration. Hence, achieving a high concentration ratio of the desired carriers, which are electrons in the n-type layer, is crucial for designing a contact with high selectivity. To date, two selectivity models have been proposed by Brendel et al. [24] and Roe et al. [25]. Rau et al. [26] demonstrated the relationship between contact selectivity and the built-in potential or diffusion potential (V_d).

In this work, the contact selectivity of the n-type layer was controlled through the adjustment of the minority carrier concentration (p) at the interface through the selection of an appropriate electron affinity for the heterojunction n-type material. As depicted in Figure 3-11, compared to the low electron affinity material with $\mathrm{X}^{Window} = 4.45\,eV$, the device with $\mathrm{X}^{Window} = 4.95\,eV$ had a smaller V_d, resulting in $p^{\mathrm{X}=4.95} > p^{\mathrm{X}=4.45}$. Assuming the same majority carrier concentration in the n-type layer, we can define selectivity S as the ratio of the majority to the minority carriers in the layer. In this comparison, the electron contacts selectivity S_n for these designs was $S_n^{\mathrm{X}=4.95} < S_n^{\mathrm{X}=4.45}$. In other words, the n-type layer with a lower electron affinity material relative to the absorber, acted as a more effective electron contact in terms of carrier selectivity. Despite a high interface defect

concentration, the high V_{OC} could be achieved and maintained because the contact efficiently collected electrons while repelling holes.

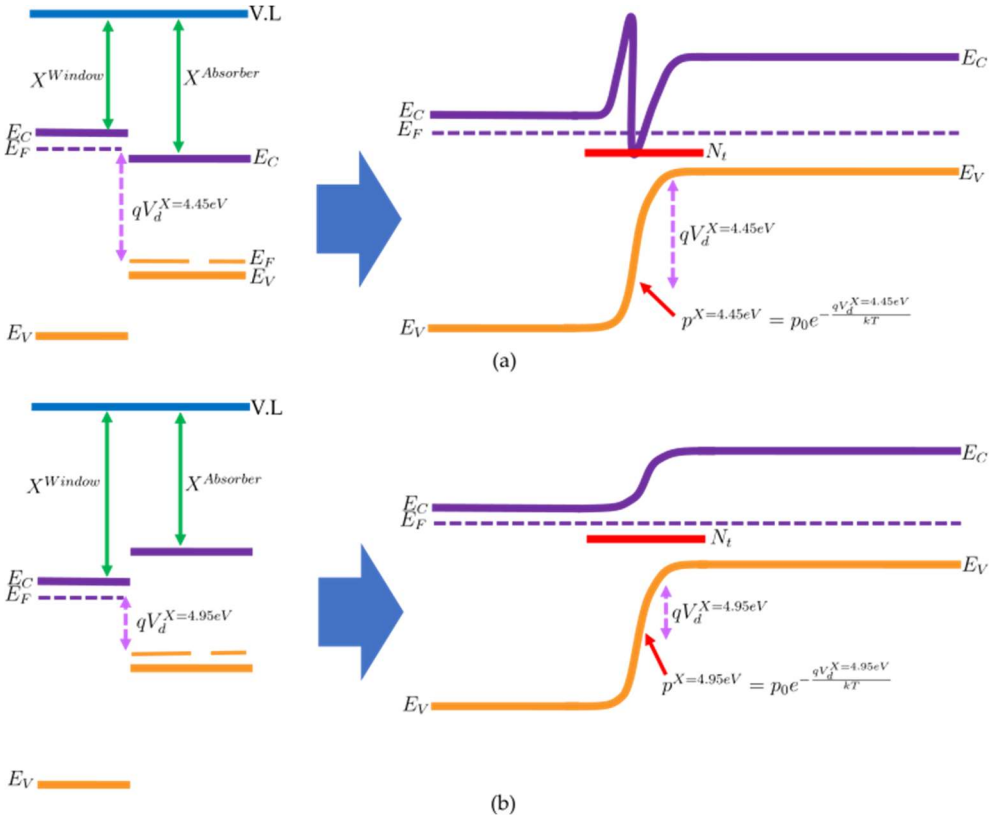

Figure 3-11 Illustration of the diffusion potential V_d effect on the hole concentration at the interface in devices with (a) low electron affinity and (b) high electron affinity.

References

[1] M. Gloeckler, A. Fahrenbruch, and J. Sites, "Numerical modeling of CIGS and CdTe solar cells: setting the baseline," in *3rd World Conference onPhotovoltaic Energy Conversion, 2003. Proceedings of*, 2003, vol. 1, pp. 491-494: IEEE.

[2] Y. Liu *et al.*, "Boosting electron transport and reducing open-circuit voltage deficit of CIGS solar cells with Zn1− x Mg x O buffer layer," *Journal of Materials Science: Materials in Electronics,* pp. 1-13, 2022.

[3] S. Ishizuka *et al.*, "Physical and chemical aspects at the interface and in the bulk of CuInSe 2-based thin-film photovoltaics," *Physical Chemistry Chemical Physics,* vol. 24, no. 3, pp. 1262-1285, 2022.

[4] T. Nishimura, S. Kim, J. Chantana, Y. Kawano, S. Ishizuka, and T. Minemoto, "Application of Al-Doped (Zn, Mg) O on pure-sulfide Cu (In, Ga) S2 solar cells for enhancement of open-circuit voltage," *Solar Energy Materials and Solar Cells,* vol. 202, p. 110157, 2019.

[5] H. Hiroi, Y. Iwata, H. Sugimoto, and A. Yamada, "Progress toward 1000-mV open-circuit voltage on chalcopyrite solar cells," *IEEE Journal of Photovoltaics,* vol. 6, no. 6, pp. 1630-1634, 2016.

[6] M. Burgelman, P. Nollet, and S. Degrave, "Modelling polycrystalline semiconductor solar cells," *Thin solid films,* vol. 361, pp. 527-532, 2000.

[7] M. Burgelman, K. Decock, S. Khelifi, and A. Abass, "Advanced electrical simulation of thin film solar cells," *Thin Solid Films*, vol. 535, pp. 296-301, 2013.

[8] K. Decock, P. Zabierowski, and M. Burgelman, "Modeling metastabilities in chalcopyrite-based thin film solar cells," *Journal of Applied Physics*, vol. 111, no. 4, p. 043703, 2012.

[9] A. Niemegeers and M. Burgelman, "Numerical modelling of ac-characteristics of CdTe and CIS solar cells," in *Conference Record of the Twenty Fifth IEEE Photovoltaic Specialists Conference-1996*, 1996, pp. 901-904: IEEE.

[10] S. Degrave, M. Burgelman, and P. Nollet, "Modelling of polycrystalline thin film solar cells: new features in scaps version 2.3," in *3rd World Conference onPhotovoltaic Energy Conversion, 2003. Proceedings of*, 2003, vol. 1, pp. 487-490: IEEE.

[11] B. Mohamed, S. Zambou, and S. S. Zekeng, "Influence of moisture on the operation of a mono-crystalline based silicon photovoltaic cell: A numerical study using SCAPS 1 D," *arXiv preprint arXiv:1712.08117*, 2017.

[12] S. Khelifi, J. Verschraegen, M. Burgelman, and A. Belghachi, "Numerical simulation of the impurity photovoltaic effect in silicon solar cells," *Renewable Energy*, vol. 33, no. 2, pp. 293-298, 2008.

[13] L. Ayat, S. Nour, and A. Meftah, "Computer simulation of hydrogenated amorphous silicon solar cell," 2013.

[14] T. Azizi, A. Torchani, M. B. Karoui, R. Gharbi, M. Fathallah, and E. Tresso, "Effect of defects on the efficiency of a-SiC: H pin based solar cells," in *2013 International Conference on Electrical Engineering and Software Applications*, 2013, pp. 1-5: IEEE.

[15] P. Chelvanathan, M. I. Hossain, and N. Amin, "Performance analysis of copper–indium–gallium–diselenide (CIGS) solar cells with various buffer layers by SCAPS," *Current Applied Physics,* vol. 10, no. 3, pp. S387-S391, 2010.

[16] M. Burgelman and J. Marlein, "Analysis of graded band gap solar cells with SCAPS," in *Proceedings of the 23rd European Photovoltaic Solar Energy Conference, Valencia*, 2008, pp. 2151-2155.

[17] M. Houshmand, M. H. Zandi, and N. E. Gorji, "SCAPS modeling for degradation of ultrathin CdTe Films: Materials interdiffusion," *JOM,* vol. 67, pp. 2062-2070, 2015.

[18] C.-H. Huang and W.-J. Chuang, "Dependence of performance parameters of CdTe solar cells on semiconductor properties studied by using SCAPS-1D," *Vacuum,* vol. 118, pp. 32-37, 2015.

[19] O. Simya, A. Mahaboobbatcha, and K. Balachander, "A comparative study on the performance of Kesterite based thin film solar cells

using SCAPS simulation program," *Superlattices and Microstructures,* vol. 82, pp. 248-261, 2015.

[20] T. Minemoto *et al.*, "Theoretical analysis of the effect of conduction band offset of window/CIS layers on performance of CIS solar cells using device simulation," *Solar Energy Materials and Solar Cells,* vol. 67, no. 1-4, pp. 83-88, 2001.

[21] T. Minemoto, Y. Hashimoto, T. Satoh, T. Negami, H. Takakura, and Y. Hamakawa, "Cu (In, Ga) Se 2 solar cells with controlled conduction band offset of window/Cu (In, Ga) Se 2 layers," *Journal of applied physics,* vol. 89, no. 12, pp. 8327-8330, 2001.

[22] T. Minemoto *et al.*, "Control of conduction band offset in wide-gap Cu (In, Ga) Se2 solar cells," *Solar energy materials and solar cells,* vol. 75, no. 1-2, pp. 121-126, 2003.

[23] U. Würfel, A. Cuevas, and P. Würfel, "Charge carrier separation in solar cells," *IEEE Journal of Photovoltaics,* vol. 5, no. 1, pp. 461-469, 2014.

[24] R. Brendel and R. Peibst, "Contact selectivity and efficiency in crystalline silicon photovoltaics," *IEEE Journal of photovoltaics,* vol. 6, no. 6, pp. 1413-1420, 2016.

[25] E. T. Roe, K. E. Egelhofer, and M. C. Lonergan, "Limits of contact selectivity/recombination on the open-circuit voltage of a

photovoltaic," *ACS Applied Energy Materials*, vol. 1, no. 3, pp. 1037-1046, 2018.

[26] U. Rau and T. Kirchartz, "Charge carrier collection and contact selectivity in solar cells," *Advanced materials interfaces*, vol. 6, no. 20, p. 1900252, 2019.

Chapter 4 Study of Zn-Ge-O Thin Film as Low Electron Affinity Material

4.1 Introduction

As mentioned briefly in Section 2.2.3 and Section 2.3, the band gap of CIGSSe solar cells can be adjusted within the range of $1.0 - 2.4\ eV$ by varying the composition ratios of the In-Ga alloy and the S-Se alloy [1, 2]. For the purpose of using CIGSSe as the top cell in tandem solar cells, a band gap of $1.5 - 1.7\ eV$ is typically desired [3]. In single junction CIGSe solar cells consisting of pure selenide, a composition ratio of $[Ga]/([In] + [Ga]) \approx 0.3$ corresponds to a band gap of approximately $1.1\ eV$, and such cells have shown higher efficiencies of over 18% [4-6]. However, single junction CGSe cells with wider band gaps have exhibited lower performance, achieving only around 10% efficiency [7-9]. The lower open circuit voltage (V_{OC}) in CGSe cells is attributed to a deep trap located approximately $0.3\ eV$ above the valence band in the CIGS bulk [10, 11]. The concentration of this deep trap is lowest at a $Ga/(In + Ga) \approx 0.3$ ratio. However, as the $[Ga]/([In] + [Ga])$ ratio exceeds 0.3, the interface defect concentration exponentially increases, leading to a significant reduction in V_{OC}, deviating from the theoretical open circuit voltage.

In Chapter 3, the physical mechanism and related roles of the n-type layer on thin-film heterojunction photovoltaics were exhaustively discussed. The calculation results indicated that in order to effectively played the roles of interface passivation and electron selective contact, a positive conduction band offset (CBO) at the heterointerface is pertinent. In regards to wide band gap CIGSSe-based thin-film heterojunction photovoltaics, a low electron affinity n-type material is theoretically advantageous for the n-type layer application.

In this Chapter, a novel low electron affinity material will be presented.

4.2 Transparent Conductive Oxide

Transparent conductive oxides (TCOs) are the most studied materials among transparent conducting materials (TCMs). These materials display both high electrical conductivities up to about $10^4 S/m$ either intrinsically or through external doping, and high optical transparency with optical band gap around $> 3\ eV$. The initial discovery of the first TCO, cadmium oxide (CdO), dates back over a hundred years by Badeker [12]. However, significant progress in the field of TCOs and their related applications occurred in the 1960s when two compounds emerged as key players: indium oxide (In_2O_3), commonly doped with tin to form Indium Tin Oxide (ITO), and tin dioxide (SnO_2), typically doped with fluorine to create

Fluorine-Doped Tin Oxide (FTO) [13]. More recently, zinc oxide (ZnO) has gained considerable attention as a TCO material, driven in part by concerns regarding the cost and availability of indium [14-16]. Some emerging TCOs include Ga_2O_3, which possesses a significantly wide band gap and is being explored for applications in power electronics [17, 18]. Another promising TCO is $BaSnO_3$, which exhibits one of the highest measured mobilities among TCOs, surpassing 120 $cm^2V^{-1}\ s^{-1}$ at room temperature [19, 20].

TCO thin films find wide-ranging applications in various industries such as solar cells, flat panel displays, touchscreens, light emitting diodes, smart-windows, transparent heaters, heat mirrors, etc. One of the main markets for TCO is architectural applications, where energy-efficient windows are used to prevent radiative heat loss. Currently, fluorine-doped tin oxide (FTO) deposited via a pyrolytic process is commonly employed in such applications due to its low emissivity properties. These coated windows are ideal for low-temperature environments, including glass freezer doors and aircraft cockpit windows.

The second major market for TCO thin films is in optoelectronic applications, including PV modules, touch screens, sensors, and flat panel displays. In these applications, ITO and ZnO are the primary materials used as transparent electrodes. ITO is widely utilized on the external surfaces of these devices. With the increasing demand for renewable energy and the consequent surge in PV panel production, there has been a need for

technological advancements, particularly in the development of thin-film PV panels. These panels require the replacement of traditional metal ribbons with transparent electrodes based on TCO layers.

4.3 N-Type Layer Dependence on The Ga- and S- Content in the $CIG(SSe)_2$ Absorber Layer

In [21], Maeda *et al.* presented the relationship between the Ga and S ratio with the position of conduction and valence bands with respect to the vacuum level. The authors proposed that Ga incorporation significantly influenced the electron affinity of the chalcopyrite material to a higher level. $[S]/([S]+[Se])$ ratio also have a similar effect although at more muted degree. This electron affinity shifts are mapped out on Figure 4-1. The valence band positions on the other hand are relatively constant for any $[Ga]/([In]+[Ga])$ ratio, and moderately decreased for higher S-content in the material.

Hence, based on the analysis and calculations conducted, it becomes evident that the manipulation of the band gap in CIGSSe by utilizing Ga and S elements not only influences the width of the band gap, resulting in a material with a broader band gap, but also affects the reference point for electron affinity. This reference point is crucial for the optimal design of the pn-junction coupling to maintain a high V_{OC}. Specifically, it requires an n-type material with a wide optical band gap and electron affinity lower

than the reference point of the absorber, which enables it to function as passivation and electron contact layers. Concerning CIGSSe solar cells, for applications as single-junction solar cells, it is apparent that the ideal X^{Window} lies within the range of $3.75 - 3.96\ eV$, whereas for tandem solar cell applications, the ideal X^{Wind} falls within the range of $3.53 - 3.74\ eV$.

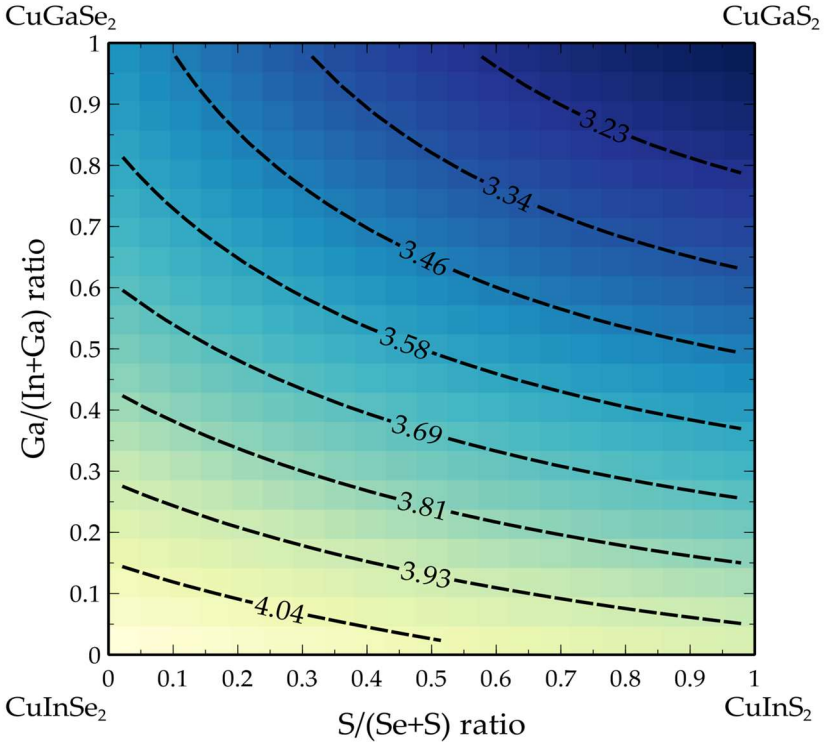

Figure 4-1 Mapping of the CIG(SSe)$_2$ absorber's electron affinity, relative to the vacuum level for various [Ga]/([Ga] +[In]) and [S]/([S] + [Se]) ratios. Adapted from [21].

4.4 ZnO Band Gap Engineering and Alloy Coupling

Customizing the band gap of ZnO allows for the adjustment of the device design to cover a wide range of wavelengths. This flexibility is especially important considering the current commercial and security objectives of developing optoelectronic devices in the UV range. One potential approach to achieve this is by alloying ZnO with materials that have larger band gaps while still maintaining compatibility with the crystal structure of ZnO. This could potentially enable the extension of ZnO's functionality to even shorter wavelengths. MgO and CdO had been shown to have a tuning effect on ZnO band gap and are expected to exhibit a type-I band alignment with ZnO, along with relatively smaller band offsets in the valence bands compared to the conduction band [22].

Cadmium oxide (CdO) possesses a narrower band gap (~2.3 eV) compared to ZnO and exists in a rock-salt phase, which is thermodynamically stable [23, 24]. The alloying of CdO with ZnO to form $Cd_xZn_{1-x}O$ (CdZnO) ternary alloys offers the possibility of narrowing the band gap, making CdZnO alloys particularly intriguing despite the toxicity associated with Cd [25]. While most cation-substituted ZnO alloys exhibit broadened band gaps in the UV and DUV regions, CdZnO ternary alloys can be finely tuned to lower energies within the visible region by adjusting the Cd composition. This expands the potential application range of ZnO-based materials. ZnO-based separate-confinement structures can be created through

alloying with $Cd_yZn_{1-y}O$, with the condition that y remains sufficiently small [22].

The similarity in ion radii between the divalent cations Mg^{2+} (0.57 Å) and Zn^{2+} (0.60 Å) suggests a high solubility of Mg in ZnO, allowing for the continuous tuning of the band gap from $3.37\ eV$ (ZnO) to $7.8\ eV$ (MgO) [26, 27]. However, due to the distinct crystal structures of ZnO (wurtzite hexagonal) and MgO (rock-salt cubic), there are significant lattice mismatches between them. This poses challenges in achieving high-Mg-content $Mg_xZn1\text{-}xO$ with a single wurtzite structure, resulting in limited band gap tunability. Experimental evidence suggests that the band gap of ZnO can be increased by forming wurtzite alloys of $Mg_xZn_{1-x}O$, as long as the value of x is not too large [28]. The development of non-thermal equilibrium growth techniques has enabled the realization of high levels of Mg incorporation in ZnO without phase separation [29].

The phase segregation in MgZnO can be attributed to the significant lattice mismatch along the a-axis and the crystallographic structural difference between ZnO (hexagonal with $a = 3.25$ Å) and MgO (cubic with $a = 4.22$ Å). However, BeO, which shares the same hexagonal structure as ZnO but possesses a much smaller a-axis length of 2.70 Å, may offer a potential solution. The large lattice mismatches between BeZnO and MgZnO could potentially counteract each other. Theoretical calculations by Su *et al.* [30] revealed that the a-axis length of MgZnO increases with an

increase in Mg content, while BeZnO exhibits the opposite trend, indicating that the compressive strain induced by Be along the a-axis could partially compensate for the tensile strain caused by Mg. Notably, it has been reported [31, 32] that the appropriate incorporation of Be can stabilize high-Mg-content wurtzite MgZnO.

GeO_2 is a promising alloying material for ZnO as it provides a favourable compromise between the electron affinity (X) and the energy band gap (E_g) [33]. In this research, we have successfully developed a novel Zn-Ge-O thin film using metal organic chemical vapor deposition (MOCVD). These thin films exhibit properties that make them suitable for application as TCOs. Our study focused on the control of Ge concentration in the film, and we have conducted optical and electrical characterizations on multiple Zn-Ge-O samples. To the best of our knowledge, limited research has been conducted on the ternary Zn-Ge-O compound in the field of TCOs, with the exception of its application in Cu_2O solar cells [34].

4.5 Experimental Set-Up

4.5.1 Epitaxial Film Growth

The films were deposited on soda lime glass substrates using the metal organic chemical vapour deposition (MOCVD). The soda lime glass substrates were prepared through wet cleaning in a diluted nonphosphorus cleaning solution to remove surface impurities and air-drying using

nitrogen air gun. The substrates were then placed in the reaction chamber as shown in Figure 4-2 on a heated stage. During the film growth, the atmosphere in the reaction chamber was maintained at 400 Pa and the stable temperature of 160°C. Diethylzinc (DEZn), tetramethoxygermanium (TMGe), and purified water (H2O) were employed as the precursors for Zn, Ge, and O, respectively. The precursors were vapourised at 20°C for DEZn, 27°C for TMGe, and 40°C for H2O. The materials were transported into the reaction chamber using an Argon carrier gas and each material flow rates were controlled by a material flow controllers appended to the individual lines. The material flow rates of DEZn and H2O were 60.3 and 140 $\mu mol \cdot min^{-1}$, respectively. An *i*-ZnO thin film was grown under similar condition as a reference.

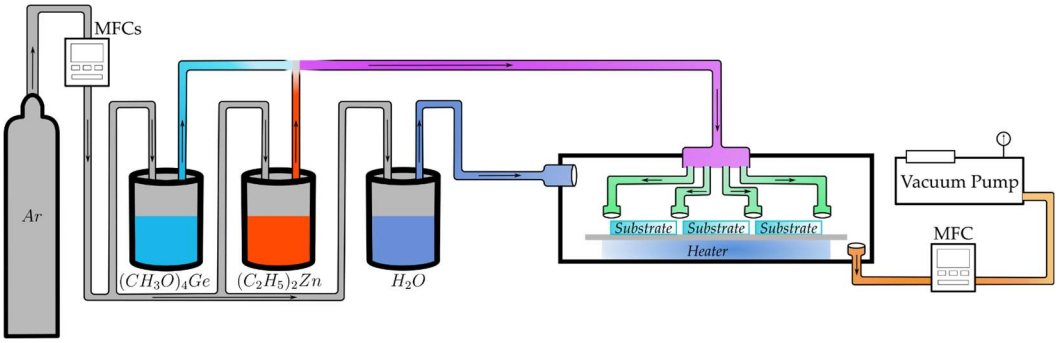

Figure 4-2 Schematic of metal-organic chemical vapour deposition (MOCVD) for Zn-Ge-O thin film deposition on glass.

To observe the impact of different concentrations of concentrations of Ge on the thin film properties, the Ge content in the Zn-Ge-O alloy was regulated by adjusting the flow rate of TMGe, ranging from

1.51 to 12.1 $\mu mol \cdot min^{-1}$. All the deposited Zn-Ge-O thin films were not doped. All samples were naturally cooled down in the chamber until the temperature drops below 110°C before being removed for characterisation.

4.5.2 Film Characterisation

The ratio on Zn and Ge in the film was investigated through inductively coupled plasma mass spectrometry (ICP-MS). ICP-MS is a highly sensitive and precise analytical technique used to determine the elemental composition and isotopic ratios in diverse samples. As illustrated in Figure 4-3, it combines inductively coupled plasma, which atomizes and ionizes the sample, with mass spectrometry, which separates and detects the ions based on their mass-to-charge ratio. ICP-MS provides the ability to detect trace elements at incredibly low concentrations and simultaneously analyse multiple elements. In this study, 10 ml nitric acid (HNO_3) was used for the digestion of the Zn-Ge-O film samples to prepare for the measurement [35].

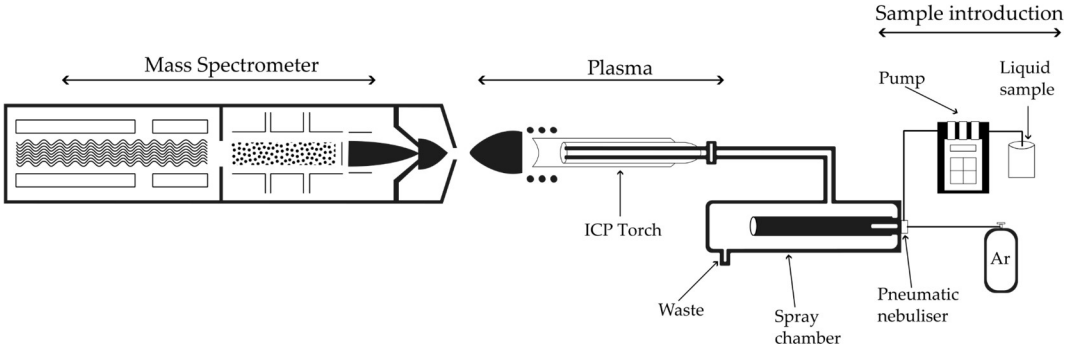

Figure 4-3 Schematic diagram of ICP-MS equipments and process.

To evaluate the optical band gaps of the Zn-Ge-O films, the approximation was derived from the transmittance and reflectance of the film measured by Ultaviolet-Visible (UV-Vis) spectroscopy in the wavelength range of $300 - 1000\,nm$. Electromagnetic wave on specific wavelengths was passed through the sample onto a sensor that measured the intensity of the transmitted or the reflected wave as described in Figure 4-4. The obtained values were calculated to obtain the absorption coefficient α and $(\alpha h\nu)^2$, assuming a direct band gap material similar to ZnO, to draw the Tauc Plot from which the optical band gap can be closely estimated.

Photoemission yield spectroscopy (PYS) was used in this work to examine the work function Φ of the films and to determine the electron affinity X position with respect to the vacuum level. PYS is a technique used to investigate the electron emission properties of a material when illuminated with light as shown in Figure 4-5. By varying the incident photon energy and analysing the emitted electrons, valuable information about the electronic structure, band gap, work function, and surface properties of the material can be obtained.

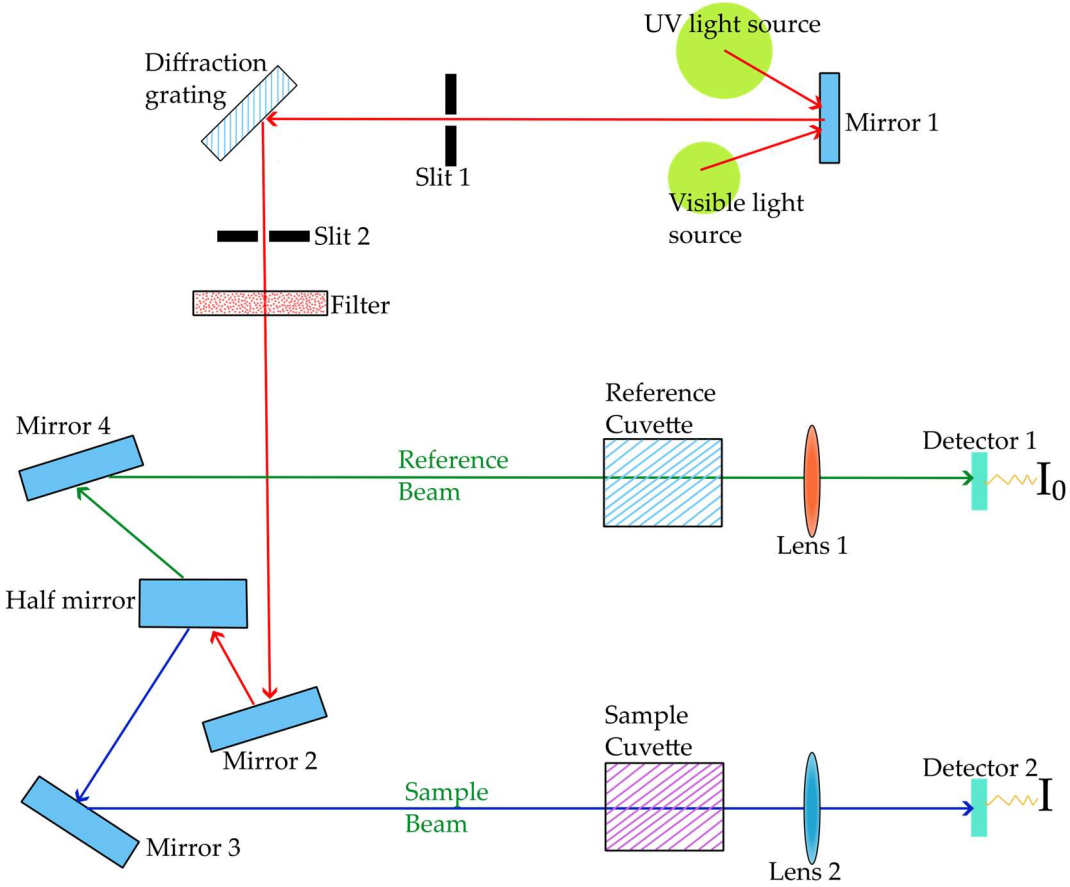

Figure 4-4 Schematic diagram of UV-Vis equipments and process.

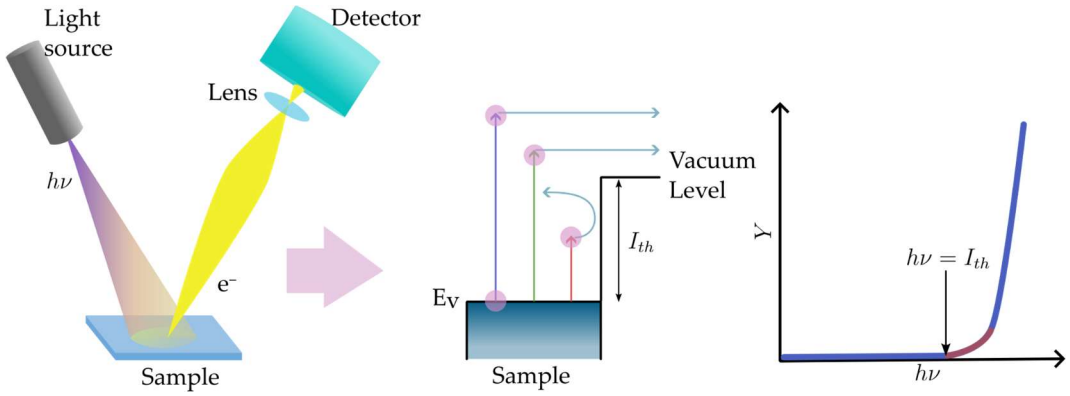

Figure 4-5 Schematic diagram of PYS measurement.

X-ray diffraction (XRD) is a widely used analytical technique for characterizing the atomic and molecular structure of materials. It is based on the principle of Bragg's law $2d\ sin\theta = \lambda$, which states that when X-rays with λ wavelengths interact with a crystal lattice with specific spacing d, they undergo constructive interference, resulting in a characteristic diffraction pattern at θ diffraction angle. In XRD, a sample is irradiated with X-rays of a specific wavelength, and the resulting diffraction pattern is recorded. By analysing the positions and intensities of the diffraction peaks, valuable insights can be gained into the arrangement of atoms, phase composition, crystal defects, and texture of the material. In this study, $CuK\alpha$ X-ray and $\theta - 2\theta$ method was used.

Van der Pauw method and four-probes method were used to evaluate the electrical properties of the thin film such as sheet resistance ρ, conductivity σ, carrier mobility ν, and carrier concentration n. The AC Hall measurement was conducted based on the Hall effect, which describes the deflection of charge carriers in a magnetic field when an electric current flows through a conductor. In AC Hall measurement, an alternating current is passed through the sample, while a magnetic field is applied perpendicular to the current. The resulting Hall voltage, which is proportional to the product of the magnetic field, current, and charge carrier properties, is measured. By varying the magnetic field strength and analysing the Hall

voltage, valuable information about the type of charge carriers (electrons or holes), their density, and mobility can be obtained.

Atomic Force Microscopy (AFM) is a high-resolution imaging technique that allows for the visualization and characterization of surfaces at the nanoscale. It operates by scanning a sharp tip mounted on a cantilever over the surface of a sample. As the tip interacts with the surface at several Å distance, it experiences interatomic forces that cause the cantilever to deflect. This deflection is detected by a piezoelectric element and used to generate a topographic image of the sample surface with remarkable resolution. In addition to imaging, AFM can also provide information about various surface properties, such as mechanical properties (e.g., elasticity and adhesion), electrical properties (e.g., conductivity and capacitance), and magnetic properties (e.g., magnetic force microscopy). One of the key advantages of AFM is its versatility, as it can be used to study a wide range of materials, from metals and semiconductors to polymers and biological samples due to its ability to interact with sample of any conductivity.

Transmission Electron Microscopy (TEM) instrument utilizes a high-energy electron beam that is transmitted through a thin film sample. As the electrons interact with the atoms in the film, they undergo various scattering processes. The scattered electrons include both elastic scattered electrons which did not lose energy, and inelastic scattered electrons which lost part of their energy. Similar to the XRD method, the diffracted elastic

scattered electrons can be used to investigate crystallinity. On the other hand, inelastic scattered electrons can be used to identify elements by measuring their energy losses. By analysing the scattering patterns, information about the crystal structure, lattice defects, grain boundaries, and thickness of the thin film can be obtained. The high-resolution capabilities of TEM allow for the visualization of individual atoms and the observation of nanostructures within the thin film. This enables detailed analysis of the film's crystallographic orientation, grain size, and interfaces.

Transmission Electron Diffraction (TED) measurement is a technique used in TEM to investigate the crystal structure, crystallographic orientation, and lattice parameters of materials at the atomic scale. It is based on the principle of electron diffraction, which occurs when a beam of electrons interacts with a crystal lattice and undergoes constructive interference. In TED measurement, a thin sample is illuminated with a high-energy electron beam in the TEM instrument. The electrons interact with the atoms in the crystal lattice, resulting in diffraction patterns that are recorded using a detector. These patterns consist of a series of bright spots called diffraction spots or reflections. The diffraction spots in the pattern correspond to specific crystallographic planes within the sample. By analysing the positions, intensities, and shapes of the diffraction spots, valuable information about the crystal structure and orientation can be obtained. This includes

determining the lattice spacing, crystal symmetry, crystallographic phase, and the presence of defects or imperfections in the crystal lattice.

4.6 Analysis of Single Layer Zn-Ge-O Thin Film

The results obtained from the ICP-MS measurement revealed a clear and consistent linear correlation between the variable n and the Ge concentration in the deposited samples, as illustrated in Figure 4-6. It was observed that as the Ge flow rate increased, indicating a higher supply of tetramethoxygermanium (TMGe), the Ge concentration in the samples also increased. Simultaneously, there was a corresponding decrease in the concentration of zinc (Zn), suggesting the replacement of Zn atoms by Ge in the film structure. This phenomenon was particularly evident when comparing the samples deposited with different Ge flow rates.

The experiments yielded four distinct compositional ratios of [Ge] / [Zn + Ge], namely 1.1%, 1.8%, 3.5%, and 8.1%. These ratios were achieved by adjusting the Ge flow rate while keeping the DEZn flow rate constant. Of particular interest was the sample with the highest compositional ratio of 8.1%, which exhibited a corresponding $n_{Ge}/(n_{Zn} + n_{Ge})$ flow rate ratio of 16.7%. This observation suggested that the TMGe gas was less reactive to water vapor compared to the DEZn gas during the film deposition process.

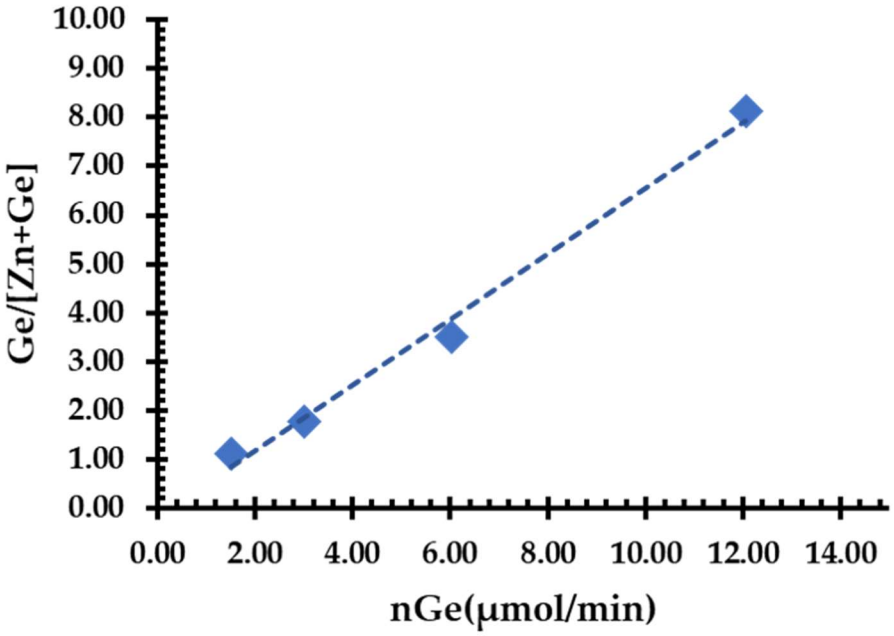

Figure 4-6 [Ge] / ([Ge] + [Zn]) compositional ratio as a function of flow rate of TMGe (n_{Ge}) for the the Zn-Ge-O films deposited by the different n from 1.51 to 12.1 $\mu mol\ min^{-1}$.

An interesting finding was that the film growth rate remained relatively constant across all the tested Ge flow rates. Regardless of the Ge concentration in the samples, the growth rate was consistently around 0.36 $nm \cdot s^{-1}$. This result indicates that the presence of different Ge concentrations did not significantly affect the overall deposition rate of the films.

4.6.1 Optical Properties

The results of the Tauc-plot analysis, presented in Figure 4-7, provide valuable insights into the optical properties of the samples. It is evident from the plot that there is a noticeable shift in the absorption edge

towards a wider energy gap (E_g) as the Ge content in the films increases. This shift implies a change in the band gap characteristics of the films.

By estimating the optical E_g for each film, it was determined that the film with a compositional ratio of 1.1% [Ge] / ([Zn] + [Ge]) had an E_g of 3.37 eV. As the Ge content increased, the optical E_g values also increased: 3.40 eV for the film with 1.8% [Ge] / ([Zn] + [Ge]), 3.53 eV for the film with 3.5% [Ge] / ([Zn]+[Ge]), and 3.60 eV for the film with 8.1% [Ge] / ([Zn]+[Ge]). These findings indicate that the introduction of Ge into the ZnO alloy composition leads to a wider band gap, affecting the optical properties of the films.

For comparison purposes, the Tauc-plot of the reference non-doped ZnO film is also included in Figure 4-7. From this plot, it was determined that the E_g of the reference ZnO film was measured to be 3.25 eV. This value serves as a baseline for understanding the impact of the Ge content on the band gap characteristics of the Zn-Ge-O films.

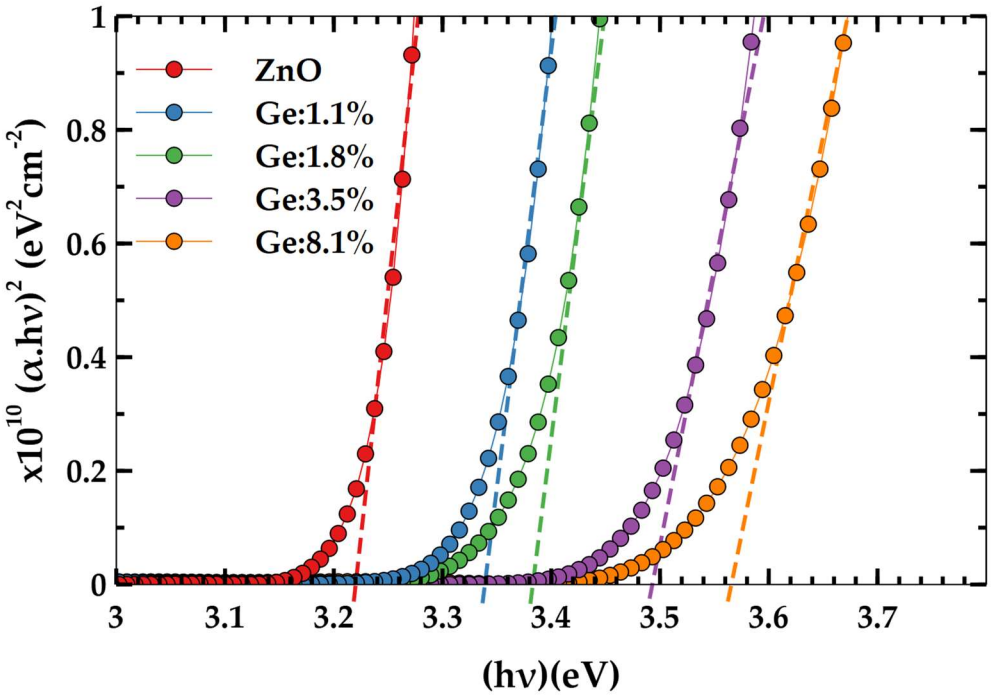

Figure 4-7 Tauc-plot to estimate the E_g of Zn-Ge-O films with various Ge content and reference ZnO film.

In order to estimate the electron affinity (X) of the Zn-Ge-O films, we employed the Photoemission Yield Spectroscopy (PYS) method to characterize their ionization energies. By subtracting the band gap energy (E_g) from the ionization energy, we were able to determine the X value of Zn-Ge-O. The results of this analysis are summarized in Figure 4-8, which presents the estimated positions of the conduction band minimum (CBM) and the valence band maximum (VBM) as a function of the compositional ratio [Ge] / ([Zn] + [Ge]).

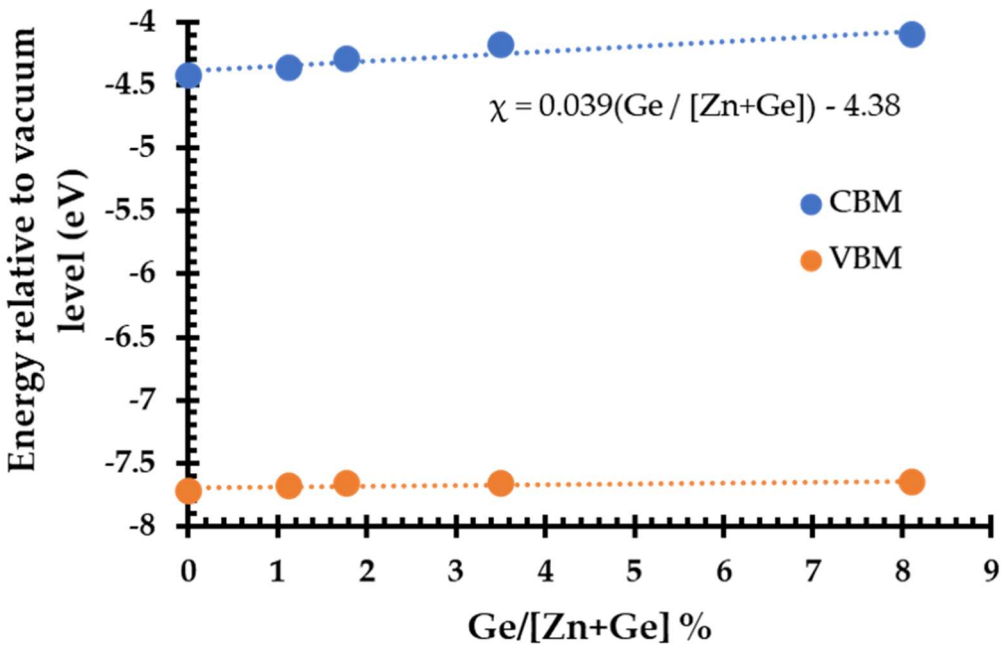

Figure 4-8 Conduction band minimum (CBM) and valence band maximum (VBM) as a function of the [Ge] / ([Zn] + [Ge]) compositional ratio. CBM and VBM values were estimated band gap and ionization energy obtained by UV–Vis and PYS measurements.

Through our analysis, we observed a linear decrease in the X value of Zn-Ge-O films with an increasing Ge concentration. This relationship between the compositional ratio [Ge] / ([Zn] + [Ge]) and the shift of X is described by Eq. 4.1. Notably, for the sample with an 8.1% [Ge] / ([Zn] + [Ge]) compositional ratio, the X value was found to be 4.06 eV, which is lower than the reference X value of ZnO, which measured at 4.42 eV. These findings highlight the influence of the Ge concentration on the electron affinity of the Zn-Ge-O films.

$$X = 0.039\left(\frac{[Ge]}{[Zn]+[Ge]}\right) - 4.38 \qquad \text{Eq. 4.1}$$

It is important to note that the VBM of each sample remained nearly constant across different Ge molar concentrations. This observation suggests that the valence band behaviour was not significantly affected by the Ge content in the Zn-Ge-O films. The consistency of the VBM values provides additional insights into the electronic structure of the films and helps to elucidate the relationship between composition and electronic properties.

In oxide semiconductors like ZnO and GeO_2, the valence band maximum (VBM) is primarily composed of oxygen p-orbitals, while the conduction band minimum (CBM) consists of cation s-orbitals. Given that oxygen is a common element in both the ZnO and GeO_2 systems, it is expected that the VBM will exhibit a relatively constant value regardless of the Ge content. Conversely, the CBM appears to be influenced by the distinct chemical properties of the Zn and Ge atoms.

These findings indicate that the Zn-Ge-O film possesses characteristics that make it a promising candidate as a low-electron affinity (X) n-type material. By incorporating both Zn and Ge atoms into the film, it becomes possible to modulate its electronic properties and potentially achieve enhanced performance in various applications.

4.6.2 Crystallographic Properties

The X-ray diffraction (XRD) spectra presented in Figure 4-9 depict the characteristics of Zn-Ge-O thin films with varying Ge compositions, namely [Ge] / ([Zn] + [Ge]) ratios of 1.1%, 1.8%, 3.5%, and 8.1%. The diffraction peaks corresponding to ZnO (100) and ZnO (110) were observed at 31.8° and 56.7°, respectively, confirming the presence of these lattices on the films (ICDD PDF no.: 01-075-0576). Notably, a notable shift toward higher diffraction angles is observed in the sample with a [Ge] / ([Zn] + [Ge]) ratio of 3.5%, indicating the substitution of Zn atoms by Ge atoms which has smaller atomic radii, resulting in a lattice compression.

The XRD results further demonstrate a gradual weakening of the ZnO (100) peak as the Ge composition ratio increases, eventually disappearing in the 8.1% sample. This suggests a transition from a polycrystalline film to a less crystalline film with a higher Ge composition. The change in crystallinity observed in the XRD analysis correlates with the trend observed in Figure 4-7, where the absorption edge becomes less distinct with increasing Ge content, indicating a broader band gap.

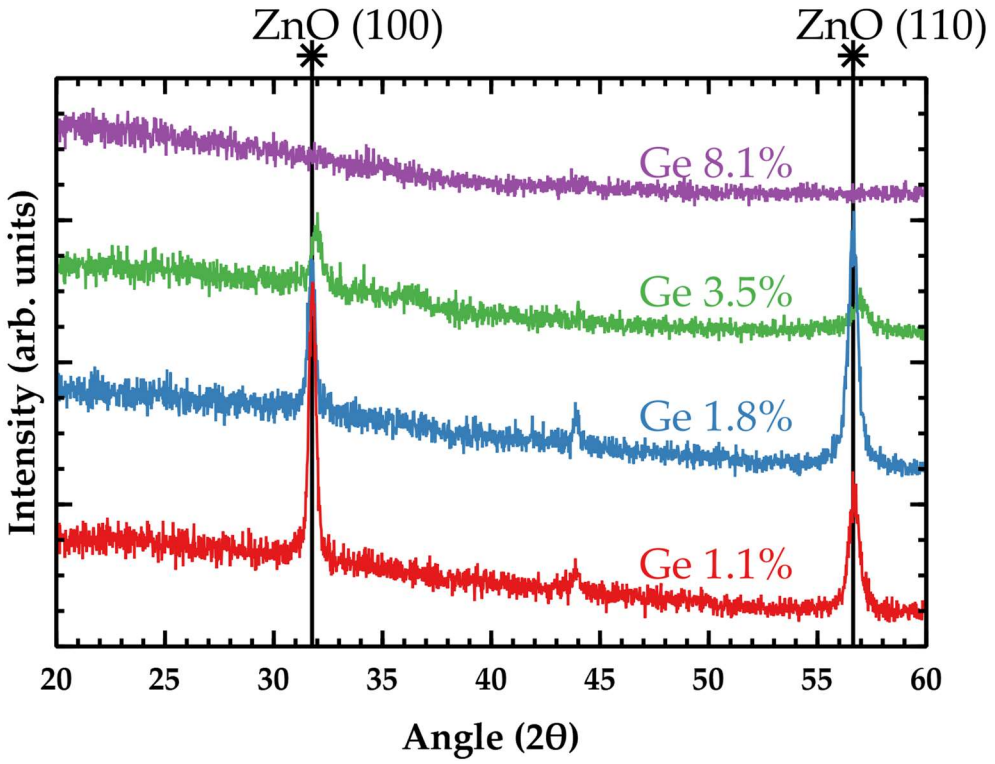

Figure 4-9 X-ray diffraction spectra of Zn-Ge-O thin-film samples with 1.1%, 1.8%, 3.5%, and 8.1% Ge content.

To gain further insight into the structural characteristics of the Zn-Ge-O films, cross-sectional transmission electron microscopy (TEM) images were captured and are presented in Figure 4-10. Specifically, the TEM images of samples with 1.8% and 8.1% [Ge] / ([Zn] + [Ge]) ratios were compared due to their substantial compositional differences. The samples exhibited relatively uniform thicknesses ranging from 600 to 700 nm. In Figure 5a, the TEM image of the 1.8% sample reveals a columnar structure resembling a typical polycrystalline ZnO structure. In contrast, the cross-sectional TEM image of the 8.1% sample (Figure 5b) does not display an

evident grain structure. Notably, both TEM images and quantitative energy-dispersive X-ray spectroscopy analysis indicated the absence of Ge segregation within the samples. This suggests that the Zn-Ge-O alloy was successfully formed through the MOCVD process.

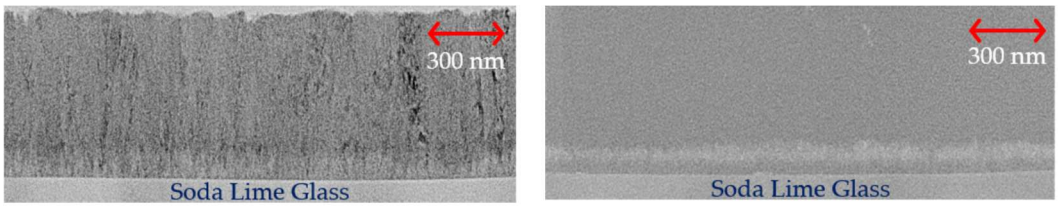

(a) (b)

Figure 4-10 Cross-sectional TEM images of Zn-Ge-O thin-film image with a) [Ge] / ([Zn] + [Ge]) = 1.8% and b) [Ge] / ([Zn] + [Ge]) = 8.1%.

Furthermore, to gain insights into the crystallinity of the Zn-Ge-O thin films, additional analysis using Transmission Electron Diffraction (TED) was conducted at a higher magnification. Figure 4-11 illustrates the diffraction patterns observed and their corresponding positions within the bulk of the films for two selected points in each sample, denoted as *1 and *2 in Figure 4-11(a) for the $[Ge]/([Zn] + [Ge]) = 1.8\%$ sample, and *3 and *4 in Figure 4-11(b) for the $[Ge]/([Zn] + [Ge]) = 8.1\%$ sample. In the case of the 1.8% sample, both *1 and *2 points exhibit a polycrystalline structure. However, a noticeable variation in the crystal ordering is observed between *1 and *2. Specifically, the region represented by *1, located at a higher position within the film, displays a higher degree of crystal order compared to *2, suggesting an improvement in crystallinity towards the upper layer of the film during the deposition process. Similarly, analysis of the

8.1% sample reveals a polycrystalline structure in the focus area, indicating the presence of nanocrystalline aggregations. These findings provide further confirmation and support the observations obtained from the XRD and TEM measurements, providing a comprehensive understanding of the crystalline characteristics of the Zn-Ge-O thin films.

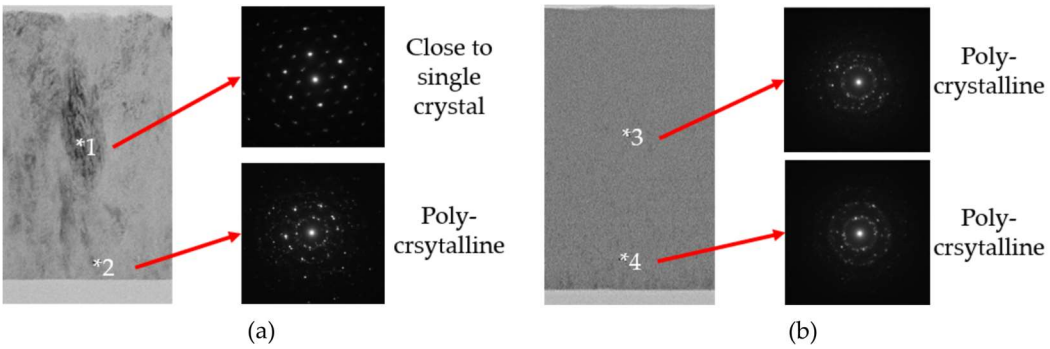

Figure 4-11 Transmission electron diffraction measurements of cross-sectional Zn-Ge-O thin-film image with a) [Ge] / ([Zn] + [Ge]) = 1.8% (i.e., points *1 and *2) and b) [Ge] / ([Zn] + [Ge]) = 8.1% (i.e., points *3 and *4).

From the TED measurement, it was found that the crystal structure of the Zn-Ge-O of the films are very close to ZnO film crystallography. Several lattice planes were identified by referencing the measured lattice spacing with ICDD PDF no.: 01-077-9355 Miller indices as illustrated in Figure 4-12. For the $[Ge]/([Zn] + [Ge]) = 1.8\%$ sample, clear diffraction signals were identified as {113}, {130}, and {220} lattices. The d-spacing of each lattice was measured to be around $0.146 - 0.147\,nm$, $0.132 - 0.136\,nm$, and $0.157 - 0.161\,nm$, respectively. These values are close to the reference d-spacing values for the reference lattices in the PDF card.

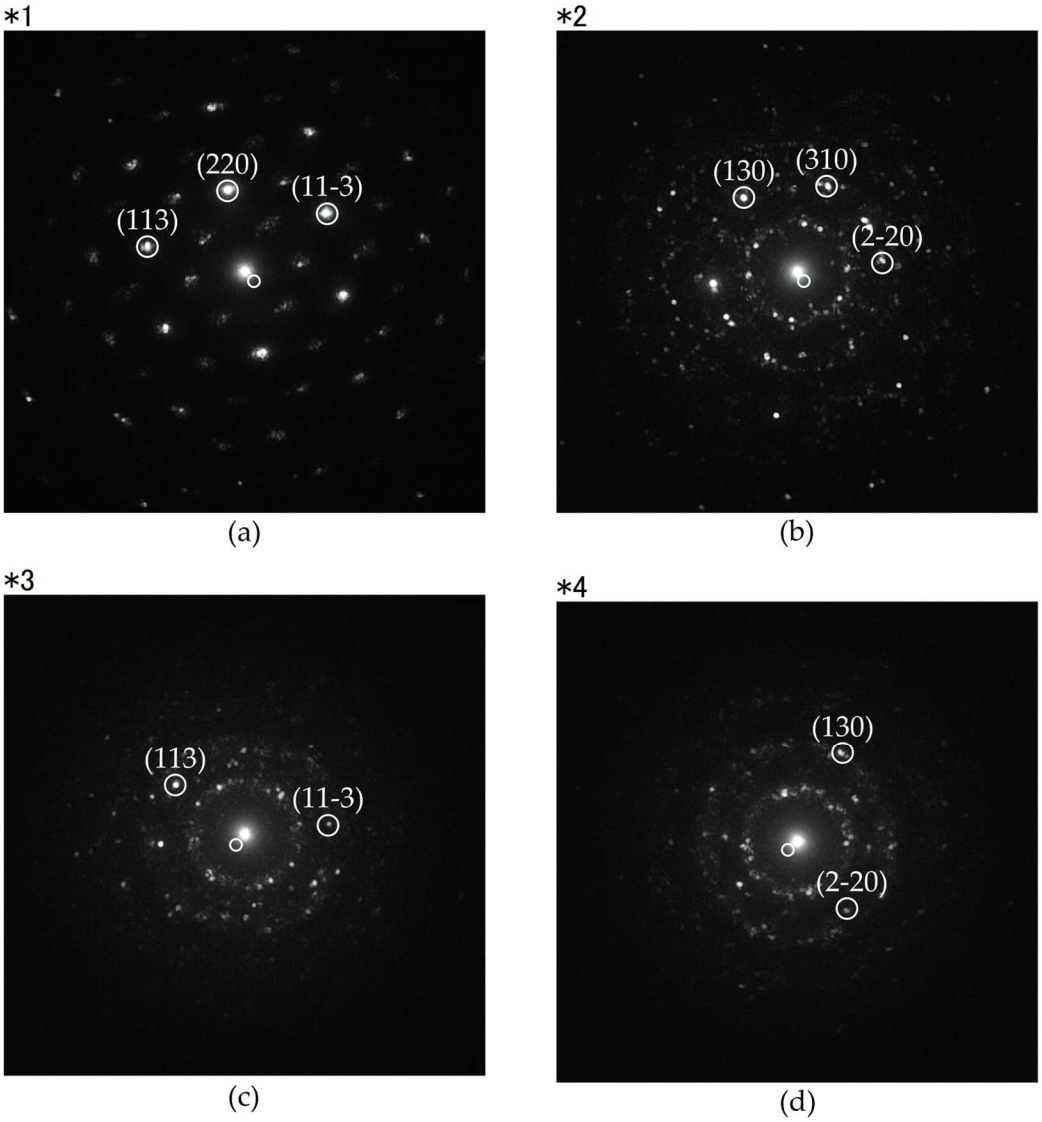

Figure 4-12 Identified lattices of ZnO crystal on the ZnGeO films with ([Zn] + [Ge]) = 1.8% (a and b) and ([Zn] + [Ge]) = 8.1% (c and d).

Unfortunately, the diffraction signals from the Zn-Ge-O single film with $[Ge]/([Zn] + [Ge]) = 8.1\%$ concentration was not definitive enough for Miller index comparison. However, by calculating the angle between the lattice planes from the $[Ge]/([Zn] + [Ge]) = 1.8\%$ sample, the

lattice planes and d-spacings could be estimated geometrically. From the calculation the presence of {113}, {130}, and {220} lattices could be approximated to exist on the $[Ge]/([Zn] + [Ge]) = 8.1\%$ Zn-Ge-O films as well. The d-spacing of each lattice were estimated to be around $0.131\ nm$, $0.153 - 0.154\ nm$, and $0.155\ nm$, respectively. Slight decrease on the {220} lattice was observed, however unusual large increases on the {113} and {130} were also noted.

4.6.3 Electrical Properties

The obtained data in Figure 4-13 provides insights into the electrical properties of the Zn-Ge-O film, specifically regarding carrier mobility and concentration. As the Ge concentration increased, a decrease in carrier mobility was observed. Additionally, the electron concentration ranged from 1×10^{18} to $1 \times 10^{19}\ cm^{-3}$ across the different samples. Interestingly, the film with an 8.1% Ge concentration exhibited no significant variations in these electrical properties. This finding is in line with the absence of peaks in the X-ray diffraction (XRD) pattern, indicating that the film is not amorphous but rather composed of aggregations of nanocrystals, as confirmed by transmission electron microscopy (TED) observations.

Considering the electrical characteristics, these results suggest that the Zn-Ge-O film holds potential for applications as a buffer layer for wide band gap chalcogenide solar cells, as well as a transparent conducting

oxide (TCO). The film's ability to modulate carrier mobility and concentration makes it a suitable candidate for improving the performance of solar cells and providing conductivity in optoelectronic devices. However, for successful TCO applications, further steps are necessary, such as the addition of dopants to enhance conductivity, and optimization of the growth conditions to achieve desired electrical properties.

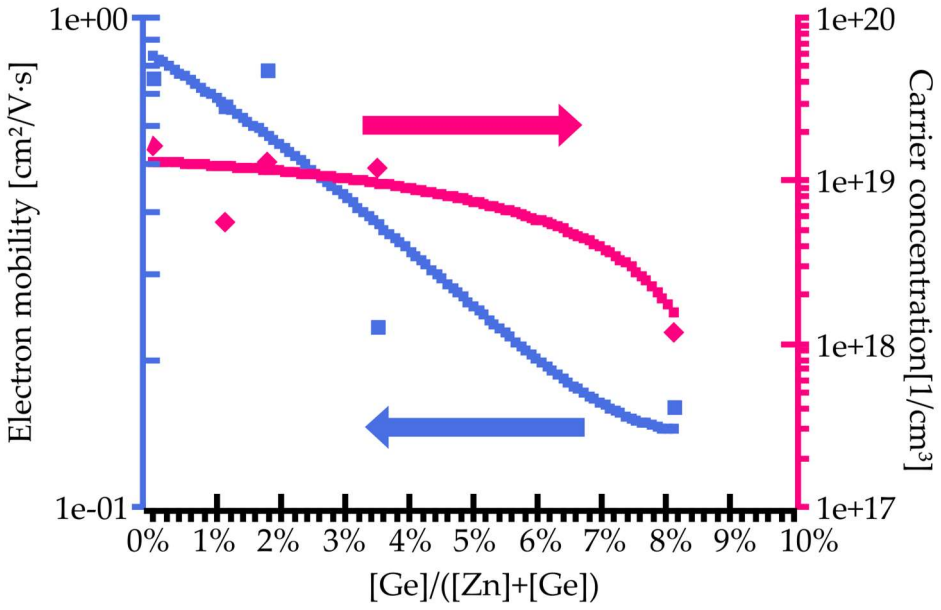

Figure 4-13 Carrier mobility and carrier concentration of Zn-Ge-O films as a function of [Ge]/([Zn]+[Ge]) compositional ratio.

4.7 Zn-Ge-O Film in Photovoltaic Device

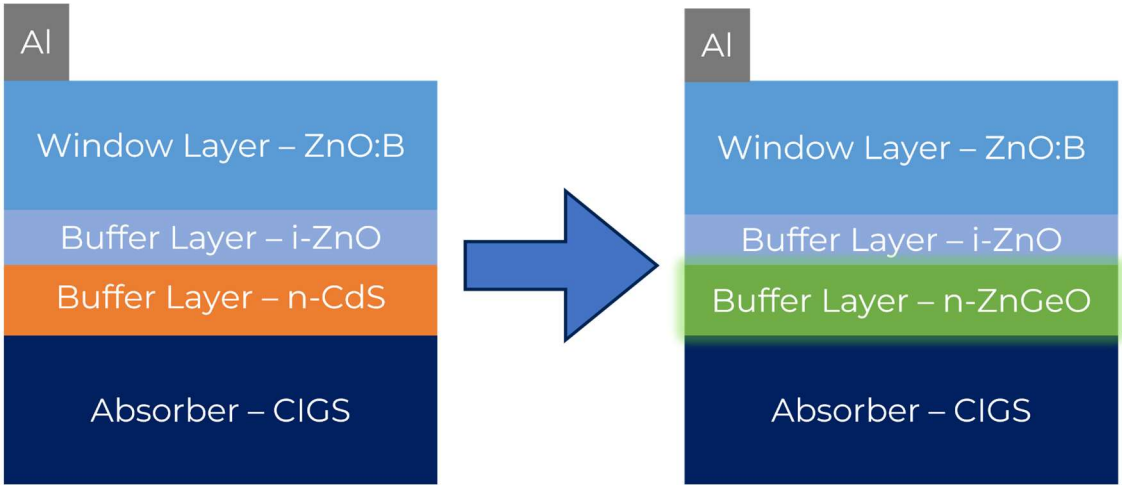

Figure 4-14 Device structure of thin-film heterojunction CIGSSe photovoltaic device with i-ZnGeO buffer layer.

Following the characterisation of the Zn-Ge-O single layer thin films the performance of the Zn-Ge-O film with various ratios of [Ge] / ([Zn] + [Ge]) as a buffer layer on a CIGSSe absorber was examined. A Mo-coated soda lime glass was used as a substrate. The narrow band gap CIGSSe absorber was deposited through the three-stage co-evaporation method, with thickness about 2 μm. As part of the initial device testing, the Zn-Ge-O film was applied as a thin buffer layer with a thickness of 50 nm replacing CdS. In addition, approximately 50 nm i-ZnO and 800 nm ZnO:B being used as the window layer (Figure 4-14). The Zn-Ge-O and ZnO films were consecutively grown through MOCVD without breaking vacuum. Finally, Al-Sn metals were used as the electrodes for the front and back contact, respectively.

Table 4-1 I–V characteristic of CIGSe solar cells with n-ZnGeO buffer layer of different Ge concentration.

[Ge]/([Zn]+[Ge])	V_{OC} [V]	$J_{SC}[mA \cdot cm^{-2}]$	FF	η [%]
1%	0.475	34.5	0.537	8.82
3%	0.470	36.7	0.511	8.81
6%	0.615	34.3	0.620	13.1

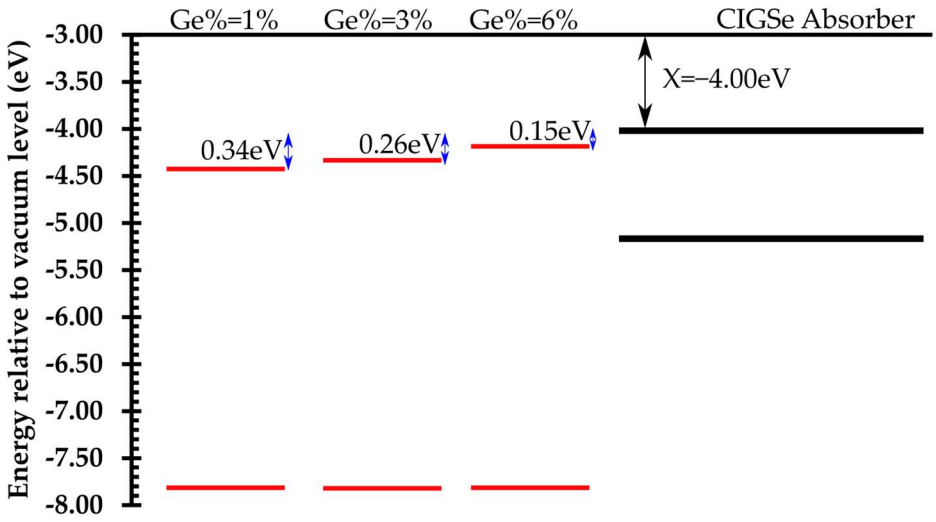

Figure 4-15 The conduction band offset shift at the ZnGeO/CIGSSe interface in correspond to the change in $[Ge]/([Zn] + [Ge])$

The results of the experiments, including the I-V characteristics, are listed in Table 4-1. A conversion efficiency η of 13.1% was achieved with V_{OC} of 0.615 V, J_{SC} of 34.3 $mA \cdot cm^{-2}$, and a fill factor of 0.620 for the device that employed a Zn-Ge-O film with a compositional ratio of 6%. The ideal-V_{OC} for $CIGSe_2$ absorber with $E_g \approx 1.1\ eV$ as used in this experiment is between $0.7 - 0.8\ V$.

The influence of the $[Ge]/([Zn] + [Ge])$ on the performance of the photovoltaics device, specifically V_{OC}, was also noted. The open circuit voltage was increased by about $0.14\ V$ when $[Ge]/([Zn] + [Ge]$ was raised from 1% to 6 %. $[Ge]/([Zn] + [Ge]$ is directly corelated to the electron affinity of the n-type layer at the heterointerface as indicated in Figure 4-8. In Section 3.5, the role of n-type layer as interface passivating material and electron selective contact were discussed. From both the perspective of interface passivation and contact selectivity, n-type material coupling with X^{n-type} lower than the X^{p-type} inhibits the recombination at the heterointerface. The conduction band offset at the heterointerface for each device can be understood from Figure 4-15 where simple band diagrams of each Zn-Ge-O buffer layer are contrasted with the $CIGSe_2$ absorber. The conduction band offset at the heterointerface was transformed from a cliff structure with $0.34\ eV$ difference for $[Ge]/([Zn] + [Ge]\ ) = 1\%$ toward close to a flat band at higher $[Ge]/([Zn] + [Ge])$.

In the subsection 3.4.2, the dependence of V_{OC} on X^{window} from the previous numerical study were shown in Figure 3-9. From that figure, it can be understood that the differences of V_{OC} between the device with $0.15\ eV$ cliff structure and the device with $0.35\ eV$, is similar to the V_{OC} difference found in the experimental result. This result shows the feasibility of Zn-Ge-O film as an alternative n-type material with low electron affinity.

References

[1] H. W. Spiess, U. Haeberlen, G. Brandt, A. Räuber, and J. Schneider, "Nuclear magnetic resonance in IB–III–VI2 semiconductors," *Physica Status Solidi B,* vol. 62, no. 1, pp. 183-192, 1974.

[2] S.-H. Wei and A. Zunger, "Calculated natural band offsets of all II–VI and III–V semiconductors: Chemical trends and the role of cation d orbitals," *Applied Physics Letters,* vol. 72, no. 16, pp. 2011-2013, 1998.

[3] T. Feurer *et al.*, "Progress in thin film CIGS photovoltaics–Research and development, manufacturing, and applications," *Progress in Photovoltaics: Research and Applications,* vol. 25, no. 7, pp. 645-667, 2017.

[4] I. Repins *et al.*, "19· 9% ‐ efficient ZnO/CdS/CuInGaSe2 solar cell with 81· 2% fill factor," *Progress in Photovoltaics: Research and applications,* vol. 16, no. 3, pp. 235-239, 2008.

[5] R. Kamada *et al.*, "New world record Cu (In, Ga)(Se, S) 2 thin film solar cell efficiency beyond 22%," in *2016 IEEE 43rd Photovoltaic Specialists Conference (PVSC)*, 2016, pp. 1287-1291: IEEE.

[6] M. Nakamura, K. Yamaguchi, Y. Kimoto, Y. Yasaki, T. Kato, and H. Sugimoto, "Cd-Free Cu(In,Ga)(Se,S)2 thin-film solar cell with record efficiency of 23.35%," *IEEE Journal of Photovoltaics,* vol. 9, no. 6, pp. 1863-1867, 11 2019.

[7] S. Ishizuka *et al.*, "Buried pn junction formation in CuGaSe2 thin-film solar cells," *Applied Physics Letters,* vol. 104, no. 3, p. 031606, 2014.

[8] D. L. Young *et al.*, "Improved performance in ZnO/CdS/CuGaSe2 thin ‐ film solar cells," *Progress in Photovoltaics: Research and Applications,* vol. 11, no. 8, pp. 535-541, 2003.

[9] S. Ishizuka, A. Yamada, P. J. Fons, H. Shibata, and S. Niki, "Impact of a binary Ga2Se3 precursor on ternary CuGaSe2 thin-film and solar cell device properties," *Applied Physics Letters,* vol. 103, no. 14, p. 143903, 2013.

[10] J. V. Li, S. Grover, M. A. Contreras, K. Ramanathan, D. Kuciauskas, and R. Noufi, "A recombination analysis of Cu (In, Ga) Se2 solar cells with low and high Ga compositions," *Solar Energy Materials and Solar Cells,* vol. 124, pp. 143-149, 2014.

[11] G. Hanna, A. Jasenek, U. Rau, and H. Schock, "Influence of the Ga-content on the bulk defect densities of Cu (In, Ga) Se2," *Thin Solid Films,* vol. 387, no. 1-2, pp. 71-73, 2001.

[12] K. Badeker, "Concerning the electricity conductibility and the thermoelectric energy of several heavy metal bonds," *Annalen der Physik,* vol. 22, p. 749, 1907.

[13] T. Minami, "Transparent conductive oxides for transparent electrode applications," in *Semiconductors and Semimetals*, vol. 88: Elsevier, 2013, pp. 159-200.

[14] M.-L. Lin, J.-M. Huang, C.-S. Ku, C.-M. Lin, H.-Y. Lee, and J.-Y. Juang, "High mobility transparent conductive Al-doped ZnO thin films by atomic layer deposition," *Journal of Alloys and Compounds,* vol. 727, pp. 565-571, 2017.

[15] S. Shinde, P. Shinde, Y. Oh, D. Haranath, C. Bhosale, and K. Rajpure, "Structural, optoelectronic, luminescence and thermal properties of Ga-doped zinc oxide thin films," *Applied Surface Science,* vol. 258, no. 24, pp. 9969-9976, 2012.

[16] P. Uprety, B. Macco, M. M. Junda, C. R. Grice, W. M. Kessels, and N. J. Podraza, "Optical and electrical properties of H2 plasma-treated ZnO films prepared by atomic layer deposition using supercycles," *Materials Science in Semiconductor Processing*, vol. 84, pp. 91-100, 2018.

[17] N. Suzuki, S. Ohira, M. Tanaka, T. Sugawara, K. Nakajima, and T. Shishido, "Fabrication and characterization of transparent conductive Sn‐doped β‐Ga2O3 single crystal," *physica status solidi c,* vol. 4, no. 7, pp. 2310-2313, 2007.

[18] S. Ohira *et al.*, "Characterization of transparent and conducting Sn-doped β-Ga2O3 single crystal after annealing," *Thin solid films,* vol. 516, no. 17, pp. 5763-5767, 2008.

[19] A. Prakash *et al.*, "Wide band gap BaSnO3 films with room temperature conductivity exceeding 104 S cm− 1," *Nature communications,* vol. 8, no. 1, p. 15167, 2017.

[20] H. Paik *et al.*, "Adsorption-controlled growth of La-doped BaSnO3 by molecular-beam epitaxy," *Apl Materials,* vol. 5, no. 11, 2017.

[21] T. Maeda, R. Nakanishi, M. Yanagita, and T. Wada, "Control of electronic structure in Cu (In, Ga)(S, Se) 2 for high-efficiency solar cells," *Japanese Journal of Applied Physics,* vol. 59, no. SG, p. SGGF12, 2020.

[22] A. Janotti and C. G. Van de Walle, "Absolute deformation potentials and band alignment of wurtzite ZnO, MgO, and CdO," *Physical Review B,* vol. 75, no. 12, p. 121201, 2007.

[23] O. Lupan, T. Pauporté, T. Le Bahers, I. Ciofini, and B. Viana, "High Aspect Ratio Ternary Zn1–x Cd x O Nanowires by Electrodeposition for Light-Emitting Diode Applications," *The Journal of Physical Chemistry C,* vol. 115, no. 30, pp. 14548-14558, 2011.

[24] D. M. Detert *et al.*, "Fermi level stabilization and band edge energies in CdxZn1− xO alloys," *Journal of Applied Physics,* vol. 115, no. 23, p. 233708, 2014.

[25] X. Wang, Y. Jin, H. He, F. Yang, Y. Yang, and Z. Ye, "Band gap engineering and shape control of colloidal Cd x Zn 1− x O nanocrystals," *Nanoscale,* vol. 5, no. 14, pp. 6464-6468, 2013.

[26] J. Zhang *et al.*, "Optical properties of the nonpolar a-plane MgZnO films grown on a-GaN/r-sapphire templates by pulsed laser deposition," *Optical Materials Express,* vol. 4, no. 11, pp. 2346-2354, 2014.

[27] X. Zhang *et al.*, "Effects of oxygen partial pressure and substrate temperature on the structure and optical properties of MgxZn1− xO thin films prepared by magnetron sputtering," *Applied surface science,* vol. 257, no. 15, pp. 6554-6559, 2011.

[28] X. Chen and J. Kang, "The structural properties of wurtzite and rocksalt MgxZn1− xO," *Semiconductor science and technology,* vol. 23, no. 2, p. 025008, 2008.

[29] W. Park, G.-C. Yi, and H. Jang, "Metalorganic vapor-phase epitaxial growth and photoluminescent properties of Zn 1− x Mg x O (0⩽ x⩽ 0.49) thin films," *Applied Physics Letters,* vol. 79, no. 13, pp. 2022-2024, 2001.

[30] L. Su, Y. Zhu, D. Yong, M. Chen, and X. Ji, "Yuquan Su, Xuchun Gui, Bicai Pan, Rong Xiang, and Zikang Tang, ACS Appl. Mater," *Interfaces,* vol. 6, pp. 14152-14158, 2014.

[31] M. Toporkov *et al.*, "Lattice parameters and electronic structure of BeMgZnO quaternary solid solutions: Experiment and theory," *Journal of Applied Physics,* vol. 119, no. 9, p. 095311, 2016.

[32] L. Su *et al.*, "Solar-blind wurtzite MgZnO alloy films stabilized by Be doping," *Journal of Physics D: Applied Physics,* vol. 46, no. 24, p. 245103, 2013.

[33] V. Afanas' ev and A. Stesmans, "Energy band alignment at the (100) Ge/HfO 2 interface," *Applied physics letters,* vol. 84, no. 13, pp. 2319-2321, 2004.

[34] T. Minami, Y. Nishi, and T. Miyata, "Efficiency enhancement using a Zn1− xGex-O thin film as an n-type window layer in Cu2O-based heterojunction solar cells," *Applied Physics Express,* vol. 9, no. 5, p. 052301, 2016.

[35] T. D. Lyon, G. S. Fell, R. C. Hutton, and A. N. Eaton, "Evaluation of inductively coupled argon plasma mass spectrometry (ICP-MS) for simultaneous multi-element trace analysis in clinical chemistry," *Journal of Analytical Atomic Spectrometry,* vol. 3, no. 1, pp. 265-271, 1988.

Chapter 5 General Conclusion and Future Prospect

5.1 General Conclusion

As the threat of climate change has turned from a probable disastrous future for a day-to-day reality to many people, the adoption of sustainable technology in our way of living has become a race against time. With the increasing threats posed by greenhouse gas emissions and global warming, transitioning to renewable sources is crucial to mitigate environmental damage. PV energy stands out due to its numerous advantages: it harnesses the sun's abundant and inexhaustible energy, generates electricity without emitting harmful pollutants or greenhouse gases, and reduces dependence on fossil fuels. By embracing photovoltaic technology on a large scale, we can significantly reduce carbon emissions, combat air pollution, and foster a more sustainable future.

CIGSSe-based thin film heterojunction solar cells are one of the prominent candidates for high-efficiency photovoltaic technology. Among the CIGSSe materials, wide band gap pure-sulfide CIGS absorbers have both the potential of being the ideal band gap single junction solar cell and the top cell for a multijunction solar cell. Previous research on wide band gap CIGSSe solar cells has primarily concentrated on pure-selenide CIGSe with high Ga content, but has failed to yield promising results because of

the drawbacks associated with high recombination in Ga-rich cells. A similar effect to band gap tuning through the conduction band minimum method by adjusting the S content. Existing literature on pure-sulfide CIGS solar cells has predominantly assumed the utilsation of techniques and materials commonly employed for narrow band gap pure selenide CIGSe solar cells. However, our study suggested that alternative n-type materials are necessary to achieve high efficiency in wide band gap CIGSSe cells. In addition, a novel n-type material with low electron affinity was introduced in this study.

Through the calculations, we clarified that, in an ideal scenario, the V_{OC} remains unaffected by the design of the n-type layer. This is because the ideal V_{OC} could be maintained by the capacitance of the depletion layer and the accumulation of carriers at the interface. However, since achieving an ideal condition in solar cell design is not realistic, this study took into account the presence of defects at the heterointerface. The calculations reveal that as the interface defect concentration increases, there would be less design flexibility for appropriate p-n material pairing, leading to V_{OC} losses in the device. This finding suggested a trade-off between employing more sophisticated fabrication methods to improve interface quality and achieving precise coupling of n-type materials in future wide band gap CIGSSe solar cell designs. In addition, through the analysis of carrier transport mechanism, the role of n-type layers as the interface passivator and carrier

selective contact was expounded in this study. Finally, it was suggested that the low electron affinity n-type material is a pivotal factor for the manufacturing of high-efficiency thin film heterojunction CIGSSe solar cells.

In this study, a single film alloy was successfully deposited using the MOCVD method to deposit using $Ge(OCH_3)_4$ as the Ge precursor. When the material flow rate in the system was controlled, the proportion of Ge material in the film was regulated. Furthermore, the alloying of Ge with ZnO was demonstrated to have the effect of widening of the E_g of the material, achieved by shifting the conduction band closer to the vacuum level. This outcome aligns with the follow-up of the result of the first part of the study: the development of an n-type material that can better align the conduction band minimum (CBM) with different CIGSSe absorbers. Furthermore, the study indicates that the increase in the Ge content leads to a transformation in the crystal structure of the film. More research and characterization will be necessary to fully understand the implications of these changes.

5.2 Future Prospect

The limitation of this study is that only the electrical, optical, and crystallographic properties of nondoped Zn-Ge-O single films were able to be thoroughly investigated. However, further studies on single-film Zn-Ge-O with a higher Ge content and dopant are needed to fully understand

properties and potential applications of this material. As a transparent conductive oxide material, Zn-Ge-O can be adapted not only as n-type material for thin-film heterojunction photovoltaics, but also for other optoelectronic applications like a touch screen, display, and sensors.

In terms of photovoltaic application, further trials on CIGSSe-based solar cells are needed to gain insight on the potential of Zn-Ge-O as an alternative buffer and window layer. In addition, a more detailed control of Ge-content throughout the epitaxial growth process will be beneficial for the future development of buffer-free CIGSSe photovoltaics. Outside of CIGSSe-based photovoltaic solar cell, other thin-film heterojunction solar cells such as CdTe, a-Si, and perovskite solar cells may also benefit from this development. In addition, the need for novel transparent conducting materials for bifacial or multijunction solar cells are also addressed through the development of Zn-Ge-O.

Acknowledgement

First and foremost, my utmost gratitude for the God Almighty, for His love and presence in my life that I experienced everyday through the people who are supporting me throughout this journey.

I dedicated this dissertation to my late grandfather, Pawin Tarigan, the Teacher of our family. Education had always been important for him. I wished I had the opportunity to present this achievement to him with the same excitement I had when I showed him my report cards back in school.

Words cannot express my appreciation to Prof. Akira Yamada, my supervisor. His guidance, never-ending support, and positive energy are my biggest motivation. My work under Prof. Yamada since 2015 shaped me into the researcher that I am today.

Assoc. Prof. Shinsuke Miyajima and Assist. Prof. Takahito Nishimura, thank you for all the advice and thought-provoking inputs throughout my research. I am also grateful for all the current and past members of Yamada-Miyajima Lab, especially the CIGS-sulfur team and the ZnGeO-team. Our collaboration is what made this dissertation possible.

I must also thank the New Energy and Industrial Technology Development Organization (NEDO) and the Japan Science and Technology Agency for their financial support in this research work.

I am also deeply grateful for my family for their prayers and emotionally support, especially for my sister, Feraena Bibyna. This journey would not even have started without her, let alone reached this finished line.

Finally, I thank my closest friends Jonathan Peang, Angel Chu, Annika Verlinde, and Alexandria Eagle. Thank you for becoming my sounding board and source of encouragement, even with all the time differences.